CHAPTER 5

THERMO-HYDRAULIC EXPERIMENTAL RESULTS

5.1 Retention Curves obtained from Vapour Equilibrium, Psychrometer Results and Air Overpressure Techniques

5.1.1 Aspects of clay-water system

Depending on the size of the pore spaces and the interactions with the solid matrix of the clay, interstitial water can be classified in three different forms (Stepkowska, 1990; Hueckel, 1992a). (1) Bulk, free macropore or capillary water contained in inter-aggregate pores (w_{mac}), which is able to flow due to hydraulic gradients. (2) Weakly bonded diffuse-layer or intercluster water (w_d) between particles and other structural elements in pores within aggregations. This intercluster adsorbed water is restricted from flow in normal conditions (Hueckel, 1992a). (3) Strongly bonded crystal phase water or hygroscopic water (w_h), which is sorbed on the external surfaces and in the interlayer spaces. This intracluster water behaves as a two-dimensional liquid, moving on the particle surface, but restricted in movement perpendicular to this surface (Stepkowska, 1990).

The typical residual hygroscopic water content w_h for Boom clay powder, corresponding to $n \delta_w \approx 5.5$ Å Stern layer (about two water molecules thick: $n = 2$) of strongly attracted adsorbed water to the mineral surface, can be estimated by the following generalised expression, which is related to the specific surface of the powder (estimated in $S_s = 40$ m^2/g according to section 2.2.1.2):

$$w_h = \frac{S_s}{2} L(2n + (L-1)m) \delta_w \rho_w R_{K+I/S} \approx 3.1\% \tag{5.1}$$

where the density of adsorbed water ρ_w may vary from 0.9 Mg/m^3 to 1.4 Mg/m^3 for the first layers of water molecules (Yong and Warkentin, 1975; Mitchell, 1993; Iwata et al., 1995; Pusch and Karnland, 1996). L represents the number of stacked layers, and n and m are the number of molecular layers of adsorbed water on the external surface and interlayer clay minerals, respectively. Typically for kaolinite-illite dominant mineralogy ($R_{K+I} \approx 65\%$ by weight of total solids), no clay platelet association is expected (L = 1). If certain quantity of smectite content is considered ($S_s \approx 600$ m^2/g; $R_S \approx 5\%$), a value of L = 1 should also be used for a dominant Na$^+$ system (Mitchell, 1993). The water content value is consistent with the residual water content of 1.5% at $\psi \approx 200$ MPa ($h_r \approx 23\%$) reported by Volckaert et al.(1996a). However, this bonded water is difficult to measure because it does not leave the clay during heating to 105°C in the standard oven drying. Total dehydration of the intracluster water occurs usually at temperatures higher than 150°C (Wang et al., 1990; Hueckel, 1992a).

Quasi-immobile water fraction (both diffuse-layer and strongly bonded water) contained at intra-aggregate level can be approximately and indirectly estimated from MIP (pore size delimiting inter and intra-aggregate zones) and main retention curves (inter and intra-aggregate zones as observed in Fig. 5.7), as well as from relative permeability results (threshold value delimiting mobile and quasi-immobile water). In practice, there are no means of directly determining this fraction from macroscopic experiments. The term quasi-immobile water refers to the non-Newtonian and Bingham water flow that may be dominant at low water contents, where the applicability of Darcy's law may be questionable: water flow in film water and water flow through filled pores under adsorptive-hydration force fields (Iwata et al., 1995).

According to MIP results presented in section 2.5.3 it appears that a pore size of around 150 nm can be accepted for the delimiting value separating inter-aggregate (related to entrapped or constricted porosity) and intra-aggregate (related to free or non-constricted porosity) zones. Interparticle distances separating intra and inter-aggregate zones between 200 Å and 1500 Å in high-porosity clays have been proposed by Touret *et al*. (1990) (referred in Robinet *et al*., 1996b). The pore size defined by MIP results is associated with an equivalent matric suction or air overpressure of 1.9 MPa at 22°C according to Laplace equation, which corresponds to a gravimetric water content of around 15% as stated by main wetting paths results presented in Fig. 5.7. This water content also appears as a delimiting point in the retention curve, separating regions of 'intra-aggregate governing suction' (gravimetric water content is not affected by mechanical effects) and 'inter-aggregate governing suction' (water content is sensitive to mechanical actions) as discussed in section 5.1.4. In addition, a water content of around 13% is associated with a region that separates zones of greater water relative permeability values in a generalised Darcian sense from others that present a restricted flow, as indicated in Fig. 5.39 and Fig. 5.40. In general, below a water content threshold value of 13% the relative water permeability is maintained below 1% as observed from inflow/outflow data interpreted using Darcy's law and a diffusion equation. All these results are consistent with the existence of two main pore size regions: an intra-aggregate porosity with quasi-immobile water that is little affected by loading processes and an inter-aggregate porosity for which the loading mechanism results in a reduction of interconnected macropores affecting free water. For these reasons, it seems adequate to admit that:

$$\left(w_{sat} - w_{mac}\right) = w_h + w_d \approx d\, S_s\, \rho_w \; ; \quad \left(w_{sat} - w_{mac}\right) \approx 13\% \quad \text{for} \quad d \approx 23\, \overset{o}{\text{A}} \qquad (5.2)$$

where d is the half-spacing in a parallel configuration of diffuse-layer water (idealised intra-aggregate void), $\rho_w \approx 1$ Mg/m^3 is the average water density and $S_s = S_{s\,K+I}\, R_{K+I} + S_{s\,S}\, R_S \approx 56$ m^2/g, the average specific surface for 65% in weight of kaolinite – illite content and 5% in weight of smectite content. It is important to emphasise that the term diffuse layer is used to describe the less bonded adsorbed water (intercluster water), although the spacing could not correspond to fully developed diffuse double layers (DDL). DDL theory describes accurately the behaviour of adsorbed water at interparticle distances greater than 30 - 50 Å and at low salt concentrations (Sposito, 1984), which is the case of the previous result.

Macropore free water content at saturation is estimated around $w_{mac} \approx 9\%$ for the low-porosity fabric and around $w_{mac} \approx 21\%$ for the high-porosity packing. For saturated Boom clay at a dry unit weight of 16.7 kN/m^3, the adsorbed quasi-immobile water represents 59% of the total volume of water in soil, whereas it corresponds to around 38% in the case of the high-porosity packing (Romero *et al*., 1998b). These results, which are represented in Fig. 5.1, compare well with intra-aggregate porosity determined with mercury extrusion, representing 28% of total porosity in the low-density packing and accounting for 54% of the total porosity in the high-density fabric. Thus, from approximately one to nearly two thirds of water behaves more like solid than fluid in these packings. For Na-montmorillonite, Pusch and Hökmark (1990) estimate that at saturation and a bulk density of 1.80 Mg/m^3, more than 60% of the water is immobile. For comparison, intra-aggregate water fractions vs. dry unit weight for different smectite clays are also represented in Fig. 5.1 (Pusch and Karnland, 1986 in Pusch and Karnland, 1996). Similar conclusions have been reported by Al-Mukhtar (1995) for saturated kaolinite under an axial loading of 1 MPa, where water contained in intra-aggregate pores represents more than ¾ of the total volume of water in the soil. Baldi *et al*. (1991) suggest that adsorbed water represents between 24% and 49% of the total water volume for natural Boom clay. Robinet *et al*. (1992) indicate a volumetric ratio of adsorbed water to total water content between 0.4 and 0.6 for low-porosity clays. Further aspects about the morphology of the porous medium interpreted with mercury intrusion and factors influencing Boom clay unsaturated hydraulic states with reference to water retention curves and relative water permeability values are discussed in Romero *et al*. (1999a).

When heated, the adsorbed quasi-immobile water may degenerate into free water. Derjaguin *et al.* (1986) suggest a breakdown of the special structure of adsorbed water contained in interstices smaller than 40 Å, which becomes more like bulk water at about 70°C. A mass-transfer model which simulates this possible degeneration is proposed in Ma and Hueckel (1992) and Ma and Hueckel (1993).

5.1.2   Main wetting and drying curves for different packings at T = 22°C (vapour equilibrium technique)

Total suction – gravimetric water content relationships at 22°C under free swelling and shrinking conditions with no change in boundary stresses ((σ_m-u_a) = 0) have been measured as a function of the initial dry density (reflecting the different packings), following the multi-stage procedure (main wetting paths followed by main drying paths) detailed in section 4.1.3. Main wetting paths refer to the slow water absorption of an initially dry sample at hygroscopic humidity, while first monotonic gradual desorption departing from a minimum suction ever experienced is referred to as main drying. Fig. 5.2 and Fig. 5.3 (a zoom of the previous figure) show the variation of water content with applied total suction (varying between 31.6 MPa and 3.2 MPa) in a main wetting path followed by a main drying path. Water contents obtained under laboratory relative humidity conditions (suction about 102 MPa) are also included. Suction - moisture content relationships were complemented in the lower suction range (between 15 MPa and 0.3 MPa) using psychrometer data (both transistor and thermocouple in main drying paths), according to the procedure outlined in section 4.1.4. Suction – water content relationships are strongly influenced by the paths followed by the specimens during testing; however, at high suction the equilibrium water content in the drying paths tend to the initial hygroscopic water content. Data from SCK.CEN (Volckaert *et al.*, 1996a; Bernier *et al.*, 1997) obtained from vapour equilibrium tests in the range of 240 MPa to 30 MPa (wetting paths) are also represented in the previous figures, as well as the logarithmic relationships between water content at equilibrium and total suction proposed by CIEMAT (Volckaert *et al.*, 1996a) and Wan (1996). As further indicated, these relationships as a function of the gravimetric water content, where the initial dry density and the overall porosity have little influence on the final water content and where water uptake/intake occurs at intra-aggregate scale, are adequate in the range between 200 MPa and around 2 MPa (for main wetting paths) and around 5 MPa (for main drying paths) for suction values greater than the air-entry value of the low and high-density soil packings. Extrapolations to lower suctions may result in different values than measured in suction controlled tests, where different porosity distributions at inter-aggregate scale are expected for the different packings with double-porosity network. It is important to indicate that the values reported by SCK.CEN (Volckaert *et al.*, 1996a; Bernier *et al.*, 1997) at low suctions (around 30 MPa) present high water content levels, which do not correspond to the values obtained by other authors and in the present investigation.

Fig. 5.4 and Fig. 5.5 show the values of dry unit weight and degree of saturation or water content measured in each sample after total suction equalisation and under free swelling and shrinking conditions (σ_m-u_a) = 0. Suction at high values is mainly controlled by the intra-aggregate pores, which will be water-saturated in a wetting path before the macropores. Under these conditions, a change in density of the soil basically reflects a change of the larger macroscopic voids, which have little influence on the suction of the soil as a whole. This situation is observed in Fig. 5.4, where in the applied range of suction, changes of degree of saturation as high as 30% due to inter-aggregate compression do not induce an appreciable soil suction change. Fig. 5.6 shows suction – degree of saturation relationships in a main wetting-drying cycle at constant dry unit weights, obtained from different interpolations using the results contained in Fig. 5.5 and assuming a non-constrained intra-aggregate swelling (refer to section 5.1.3). This data clearly shows that total suction cannot be related to a singular value of the degree of saturation. This insensitivity is related to the complex and wide nature of clayey soil structure if compared to sands, which present more fix packings. The retention curves are complemented with main drying psychrometer results previously grouped at constant packings (void ratio varying from 0.517 to 1.459), where the same trend is observed.

5.1.3   Main wetting and drying curves for different packings at T = 22°C (air overpressure technique)

In Fig. 5.7, the relationship between total suction and water content at fixed dry density has been plotted, according to the procedure outlined before (interpolations at constant dry unit weights using Fig. 5.4). Main wetting and drying data at low suction values (under 0.50 MPa) are obtained from constant volume swelling pressure tests (test series C14-SPx and C17-SPx detailed in Table 4.1 and Table 4.2) using the air overpressure methodology described in section 3.1.2. Starting from a matric suction of around 2 MPa the soil is monotonically hydrated up to 0.01 MPa and then is monotonically dried to 0.45 MPa without exceeding the air-entry value of the packing, in order to avoid inducing shrinkage that could alter null volume condition. Upon wetting, the swelling pressure tests imply certain inter-aggregate porosity decrease at expense of some non-constrained intra-aggregate swelling in order to maintain the overall constant volume condition. This is more evident in high-porosity packings, where a remarkable change in the loading trend is detected, as a consequence of inter-aggregate porosity collapse (refer to Fig. 6.73 and Fig. 6.75). The term non-constrained intra-aggregate swelling refers to a double-porosity network (aggregated fabric or dry-side compacted at medium-low dry density) where enough space is left at inter-aggregate scale to allow this swelling (usually for dry densities lower than 1.7 Mg/m^3, where more than 23% of the pore volume corresponds to entrance pore sizes higher than 1 μm). This way, interpolations of vapour equilibrium results obtained under free swelling conditions are representative values for a non-constrained intra-aggregate swelling.

A quite good correlation has been found between the different values obtained using axis translation and vapour equilibrium procedures. Both techniques can be overlapped in main wetting and drying paths showing the overall retention curve. Suction – degree of saturation retention curves (represented in Fig. 5.8 and Fig. 5.9) at fixed packings can be estimated by means of volumetric phase relations, where the remarkable influence of clayey soil structure is observed. At high suction values ('intra-aggregate governing suction') the wetting paths diverge as a result of the variation of porosity at constant water content, reaching a maximum separation around the zone corresponding to the transition between 'intra' and 'inter-aggregate governing suctions', whereas at lower suctions they converge towards 100%. The end of the main adsorption paths may differ for the different packings because of air entrapment in the soil. The air-entry values of the different drying paths appear as a particular transition zone separating quasi-saturated and unsaturated conditions and influencing hysteresis behaviour, which is shown in the closed loops represented in Fig. 5.9. Main drying path of the powdered structure is also indicated in the same figure, where a remarkable difference in the air-entry values of the different packings are observed. Under constant suction, this hydraulic hysteresis has notable influences on mechanical behaviour, because of the different arrangements of water within the voids that affect soil skeleton in different ways (Wheeler and Karube, 1996). This way, there is some need of incorporating this water content (via a function of Sr or w), either as a third independent variable as suggested by Toll (1990) or by including it within one or both of the remaining stress variables.

5.1.4   Aspects of soil – water characteristic curves (main wetting and drying paths). Soil – water characteristic curve equations

At low water content levels corresponding to the intra and intercluster water (less than 15% as estimated from MIP data or around 0.50 of plastic limit) the influence of the initial and equilibrated dry densities was found to be negligible, signifying that the suction water content relationship is mainly dependent on the specific surface of the clay (mineralogical composition) and controlled by soil intra-aggregate microstructure (refer to Fig. 5.10), which will be water-saturated in a main wetting path before the macropores. Under these conditions, a change in density of the soil basically reflects a change of the larger macroscopic voids, which have little influence on water content change and consequently on soil suction. This region, where total suction is insensitive to degree of saturation changes due to macroporosity reduction upon mechanical loading, is identified in the previous figure

as 'intra-aggregate governing suction'. It appears that gravimetric water content is more adequate as state variable than degree of saturation at high suction levels involving intra and intercluster water. Similar observations have been made on compacted sand-bentonite mixtures by Wan *et al.* (1995), where experimental data clearly show that total suction can be related to the gravimetric water content even though the data come from specimens showing a wide range of initial densities. Delage *et al.* (1998a) testing compacted bentonite observed little differences with respect to water content at high suctions between the retention curve at constant volume and the curve under free swelling conditions.

On the other hand, the 'inter-aggregate governing suction' zone indicated in Fig. 5.10 (water content is high enough to partly fill the inter-aggregation voids) is sensitive to mechanical actions, where the loading mechanism is towards the reduction of the macroporosity, affecting bulk water contained in the inter-aggregate pores, while maintaining intra-aggregate porosity not greatly affected by this effect.

The separation between inter and intra-aggregate zones indicated previously is expected not to be clearly identified in very high-density packings (around 2.0 Mg/m^3 for this type of clay and somewhat lower in more active clays) with a dominant matrix structure, even if dry-side compacted, where the delimiting line is expected to be shifted to lower suction values (the 'inter-aggregate governing suction' zone is assumed to be reduced). When performing a constant volume hydration path on such a heavily dry-side compacted packing, the intra-aggregation swelling is constrained due to the limited inter-aggregate porosity, and the intercluster wetting path will tend to the storage capacity of the matrix structure under low suction values. This condition has been experimentally detected on high-density FEBEX bentonite (dry-side compacted at a dry density of 1.75 Mg/m^3) by Villar *et al.* (1997), where a clear decrease in water content corresponding to a given suction under controlled volume is detected with respect to that obtained with unconfined specimens. Under these circumstances, no important hysteretic behaviour upon suction reversal is expected, because of the absence of a well-defined air-entry value in the inter-aggregate zone and only induced by the adsorption hysteretic mechanism at intra-aggregate scale. Delage *et al.* (1998b) and Cui *et al.* (1998b) observed no significant hysteresis in retention curves of heavily compacted clays, which can be explained in terms of the very dense state of the samples in which quasi-reversible intra-aggregate effects are predominant compared to inter-aggregate capillary phenomena.

The residual intercluster water content (w_r associated with a total suction s_r and represented in Fig. 5.10) is the water content where a large suction change is required to remove the remaining intercluster water and some intracluster water. If the curve in the high-suction range can be approximated by another line, the residual value can be considered as the ordinate of the point at which the two lines intersect. Total suction corresponding to zero water content as measured in a standard oven drying technique appears to be essentially the same for all types of soils as suggested by Fredlund and Xing (1994), where a value slightly below 1000 MPa has been experimentally supported (Koorevaar *et al.*, 1983). In addition, the psychrometric law relates a total suction of 1000 MPa with a relative humidity of around 0.01%. This way, relative humidity of water vapour versus total suction relationship can be seen as an upper limit of the soil water retention curve showing quite similar shapes as indicated in Fig. 5.10.

A recent review of soil-water characteristic curve equations is presented in Fredlund and Xing (1994) and Leong and Rahardjo (1997a), where the different expressions are derived from a single generic form. Main-wetting and drying retention curves data have been fitted to a modified form of van Genuchten (1978, 1980) expression to take into account a maximum total suction value of a = 274 MPa under null intercluster and free water content. This value corresponds to the intersection of the linear relationship between the logarithm of the suction and the intercluster water content with the suction-axis at null water content (refer to Fig. 5.10). It appears that this intersection depends on the specific surface of the clay, resulting in higher values for high-activity clays. A value of a ≈ 800 MPa has been extrapolated for FoCa clay (S_s ≈ 430 m^2/g) from main wetting path data reported by Cui *et al.* (1998b) and by Volckaert *et al.* (1996a), while a value of around a ≈ 1000 MPa has been

considered for FEBEX bentonite presenting a specific surface of $S_s \approx 600$ m^2/g according to retention curve data presented by CIEMAT (1998).

Van Genuchten (1978, 1980) original relationship (represented in Fig. 5.10) with three different soil parameters α (related to the air-entry of the soil), n (related to the slope of the inflection point) and m (related to the residual water content), is affected by a correction function C(s), similar to that proposed by Fredlund and Xing (1994). The objective of this correction function is to smooth the steep behaviour of the residual intercluster water content zone, tending to a linear relationship between the logarithm of the suction and the normalised water content, as observed in clayey soils (parameter s_r controls the shape and slope of the log s – w/w$_{sat}$ curve at low water contents). It is also a way of forcing the intercluster water content to be zero at suctions lower than 1000 MPa (refer to Fig. 5.10). The original curve is not greatly affected under suction values lower than 10 MPa, since the correction function is around 0.95 for a = s$_r$ = 274 MPa. Other correction factors that serve for the same purpose are given in Leong and Rahardjo (1997a). The expression for the degree of saturation Sr or normalised water content w/w$_{sat}$ (only valid for free and intercluster water) in terms of suction s is assumed as:

$$Sr = \frac{w}{w_{sat}} = C(s)\left(\frac{1}{1+(\alpha s)^n}\right)^m \quad ; \quad C(s) = 1 - \frac{\ln\left(1+\dfrac{s}{s_r}\right)}{\ln\left(1+\dfrac{a}{s_r}\right)} \quad \text{with} \quad 0.1\,a < s_r \le a \tag{5.3}$$

As observed, it is preferable not to include in the retention curve expression a parameter that separates the two suction zones because in matrix dominant fabrics (dry-side compacted at high dry density values), this separation zone is expected to disappear as previously suggested.

A non-linear curve-fitting algorithm using least-squares method have been implemented to determine the parameters α, n and m (for simplicity a = s$_r$ = 274 MPa). The idea is to choose the three parameters so that the sum of the squared deviations of the measured data from the calculated data is minimised. The minimisation problem of the objective function is carried out using the Solver utility from Microsoft®Excel. Best-fit curves for the different packings in main wetting and drying paths are presented in Fig. 5.7, Fig. 5.8 and Fig. 5.9. In general, Eq. (5.3) can be used to fit experimental data reasonably well over the suction range involving free and intercluster water. Fitting parameters for the different packings resulting from the regression analysis are indicated in Table 5.1.

Table 5.1 Retention curve fitted parameters from regression analysis for different packings.

Parameters	Dry unit weight (kN/m^3)				
Main-wetting	10.8 powder	13.7	14.7	15.7	16.7
	(w$_{sat}$→liq. limit)	(w$_{sat}$=33.67%)	(w$_{sat}$→29.7%)	(w$_{sat}$→25.5%)	(w$_{sat}$=24.40%)
α (MPa^{-1})		20.50 to 22.07	9.07 to 11.48	3.54 to 4.57	1.128 to 1.979
n		1.022 to 1.257	0.752 to 0.882	0.736 to 0.784	0.734 to 0.762
m		0.175 to 0.217	0.244 to 0.309	0.284 to 0.339	0.331 to 0.377
Main-drying					
α (MPa^{-1})	4.610	2.165 to 2.306			0.305 to 0.441
n	1.723	1.156 to 1.188			0.815 to 0.846
m	0.138	0.217 to 0.274			0.440 to 0.458

Usually, parameter α is the one that displays more variation between the different packings, as well as in the main wetting and drying cycles (for simplicity, parameters n and m can be considered constant for both wetting and drying curves). In general, suction values of $1/\alpha$ in main drying paths correspond to degrees of saturation of around $0.73 < (1/2)^{m} < 0.86$, which are slightly higher than the air-entry values corresponding to the maximum curvature zone of the retention curve (refer to the air-entry zone represented in Fig. 5.26).

5.1.5 Temperature effects on main wetting paths (vapour equilibrium technique)

Fig. 5.11 summarises the data corresponding to isothermal main wetting paths (variation of water content with applied total suction) performed at different temperatures (22°C, 40°C, 60°C and 80°C) under free swelling conditions $(\sigma_m-u_a) = 0$ as a function of initial dry density. Single-stage vapour equilibrium procedures (refer to section 4.1.3), permitting accurate gravimetric measurements and requiring replicate samples at different temperatures, have been used to obtain the temperature dependence of total suction at equilibrium. As observed, moisture retention capacity of the clay is influenced by temperature, where for a given water content the total suction tends to decrease with increasing temperatures. In the same way, at a given total suction, water content tends to decrease with temperature. This effect of the lower water retention at higher temperatures and at a specified suction occurs in an opposed way if compared to the effect of increasing air relative humidity with temperature at the same total suction, standing out the effect of soil matrix and interfaces in water retention. Some variability of the wetting path data at the same temperature is as large than any temperature effect (mainly at higher temperatures), hindering thermal effects on water retention. In addition, the influence of temperature is not clear detected at high suction values (higher than 70 MPa), as observed from SCK.CEN results. Lower values of moisture retention results under constant suction and higher temperatures are in agreement with those reported in the low suction range by Wilkinson and Klute (1962) testing silt with a cell pressure apparatus (air overpressure technique up to 100 kPa and 44°C); by Haridasan and Jensen (1972) testing silt loam with a pressure plate and tensiometers up to a matric suction of 70 kPa and 35°C; by Nimmo and Miller (1983) testing sand and silty loam using tensiometers (matric suction up to 50 kPa and 50°C); by Hopmans and Dane (1986) on sandy loam using tensiometers up to a matric suction of 20 kPa and 45°C; by Constantz (1991) testing sand and tuff with a pressure plate up to a matric suction of 100 kPa and 80°C; by Wan (1996) on sand-bentonite material using thermocouple psychrometers (up to a total suction of 4.5 MPa and 50°C); and by She and Sleep (1998) on silica sand using a pressure plate up to an air overpressure of 10 kPa and 80°C. Lower water contents for the same total suction and higher temperatures are also consistent with data in the high suction range (between 9 MPa and 500 MPa) obtained by Wan (1996) testing sand-bentonite, sand-illite and Boom clay up to 50°C using vapour equilibrium technique.

Data at different temperatures have been grouped at constant total suction values in dry unit weight – equilibrium water content plots (refer to Fig. 5.12) and dry unit weight – equilibrium degree of saturation relationships (refer to Fig. 5.13). Equilibrium conditions refer to total suction equalisation under free swelling conditions, which are representative for interpolations at constant packings under non-constrained intra-aggregate swelling. Dry unit weights could not be determined on low-porosity specimens because of packing destructuration upon heating induced by swelling. Total suction – degree of saturation relationships (main wetting paths) at different temperatures and fixed packings, obtained from interpolations using the data contained in the previous figure, are represented in Fig. 5.14. The systematic shifts of the points at higher temperatures are explained because of the lower water retention and higher values of free swelling detected at higher temperatures and under constant suction.

Water content – temperature plots at constant total suction varying between 6 MPa and 32 MPa are represented in Fig. 5.15, where the temperature derivative $(\partial w/\partial T)_{\psi}$ is consistently negative. Total suction – temperature plots at constant water content varying between 6% and 11%, obtained from

interpolations using Fig. 5.11, are indicated in Fig. 5.16. Consistent deviations at 80°C may be associated with some free water evaporation affecting water content determinations.

5.1.6   Aspects of temperature effects on soil water retention

Following the suggestion of Philip and DeVries (1957), which derived an expression for the temperature dependence in terms of the total potential, numerous experimental results have been interpreted based on the influence on water retention of the interfacial tension between the liquid and the gas phases (Wilkinson and Klute, 1962; Hopmans and Dane, 1986; Nimmo and Miller, 1986; Mohamed *et al.*, 1992; Wan, 1996; She and Sleep, 1998). Explanations to changes in moisture content or energy status of water in an inert soil and electrolyte free water with changes in temperature are also interpreted based on air-water interfacial tension change caused by volume change of water (Chahal, 1964; Wan, 1996); thermal expansion of entrapped air (Peck, 1960; Chahal, 1964); dissolved air release upon heating due to changes of solubility of air in water; and thermal influence on wetting coefficients or contact angles (Grant and Salehzadeh, 1996; She and Sleep, 1998). Different values of temperature coefficient of pressure potential than would be expected from considerations of surface tension – temperature relationships for free water have been reported in fine-grained active soils (electrolyte soil water), which can be explained in terms of the influence of temperature on the structural disturbances of the interlayer water lattice (Zhang *et al.*, 1993), of the effects of salts contained in soil water, the effects of solutes affecting surface tension, as well as temperature influence on chemical induced water adsorption potential, which has a prominent role in clayey soils. However, little theoretical development of such mechanisms have been published because of the difficulty for contrasting experimental data on active clays in a wide range of suctions and temperatures.

For a given water content w and a constant pore geometry, temperature effects on the capillary pressure defined by the mechanical equilibrium of a liquid – gas interface, are due to temperature induced changes in the interfacial tension between the liquid and the gas phases σ and in the wetting coefficient $\cos\theta_w$ (contact angle of the liquid – gas interface with the solid), stated by the following expression:

$$\left(\frac{\partial s(w)}{\partial T}\right)_w = \frac{s(w)}{\sigma}\frac{\partial\sigma}{\partial T} + \frac{s(w)}{\cos\theta_w}\frac{\partial(\cos\theta_w)}{\partial T} \tag{5.4}$$

The surface tension, in addition to the main dependence on temperature, is also influenced by the concentration of the liquid solution (Guggenheim, 1967). If it is admitted that the wetting coefficient is temperature independent, then Eq. (5.4) transforms to the Philip and DeVries (1957) expression. Though there has been no conclusive experimental evidence of temperature induced changes in wetting coefficients (She and Sleep, 1988), a theory to allow the formulation of the wetting coefficient - temperature derivative has been proposed in Grant and Salehzadeh (1996) based on thermodynamics of interfacial phenomena. Since surface tension of water decreases with increasing temperature and vanishes at the critical point ($T_c = 647.4$ K), the simplest possible form of empirical relation between σ and T is a linear fit, which describes the temperature effect acceptably over the temperature range -10°C to 70°C: $\sigma = a + bT$. The estimates for the two parameters are (Grant and Salehzadeh, 1996): a = 0.11766±0.00045 Nm^{-1} and b = -0.0001535±0.0000015 Nm^{-1}K^{-1}.

Temperature effects on energy status of soil water can be derived based on the following coefficients affecting a reference matric suction $s(w,T_r)$ at a reference temperature T_r:

$$\left(\frac{\partial s(w)}{\partial T}\right)_w = \frac{s(w)}{a_1 + b_1 T}; \quad \frac{s(w,T_f)}{s(w,T_r)} = \left(\frac{a_1(w) + b_1(w)T_f}{a_1(w) + b_1(w)T_r}\right)^{b_1(w)} \approx \left(\frac{a_1 + b_1 T_f}{a_1 + b_1 T_r}\right)^{b_1} \tag{5.5}$$

$$\text{or} \quad \frac{s(w,T_f)}{s(w,T_r)} = G(w)\frac{b(T_f - T_r)}{a + bT_r} + 1 \approx G\frac{b(T_f - T_r)}{a + bT_r} + 1$$

where, $a_1(w)$ and b_1 or alternatively $G(w)$ (gain factor introduced by Nimmo and Miller, 1986) are empirical functions (or coefficients) reflecting the actual behaviour compared to the surface – tension mechanism, and T_f the observational temperature ($T_f > T_r$). If values estimated from analysis of experimental data are equal to $b_1 = 1$ and $a_1 = a/b$ (a and b are the parameters of interfacial tension) or alternatively $G = 1$, then temperature induced changes may be described by temperature effects on surface tension (Philip and DeVries, 1957). If the estimated values of b_1 are near 1 and a_1 are consistent with the enthalpy of immersion prediction ($a_1 > a/b$), then the specific mechanism of the temperature dependence on the wetting coefficient can be accepted as suggested by Grant and Salehzadeh (1996). In general, it is expected that $a_1(w) \rightarrow a/b$, $b_1(w) \rightarrow 1$ or $G(w) \rightarrow 1$ for high water content levels near the soil air-entry value assuming non-electrolytic inter-aggregate water, as suggested from published results obtained for non-active soils in very low suction ranges (Nimmo and Miller, 1986; Constantz, 1991; She and Sleep, 1998).

Comparisons between total suction – temperature plots at constant water content (ranging from 6% to 11%) and predicted in terms of surface – tension mechanism of pure water ($b_1 = 1$ and $a_1 = -767$ K or $G = 1$) are shown in Fig. 5.16. At higher temperatures, the theory under-predicts the influence of temperature on total suction. Therefore, the capillary model cannot solely explain the effect of temperature on high suction values, as expected for relatively active clays and for electrolytic soil water. Similar results of greater temperature dependence have been reported by Hopmans and Dane (1986), Nimmo and Miller (1986) and Constantz (1991) in their upper suction range. No clear trend has been detected for gain factors when plotted against water content (refer to Fig. 5.17), being a representative value (3.16±1.14), which are similar to those measured by Nimmo and Miller (1986) and Constantz (1991) in the low suction range. Fig. 5.17 presents a_1 and b_1 values obtained from $\bar{s}(w)/(\delta s(w)/\delta T)$ versus T plots at different water contents ranging from 6% to 11% compared to surface-tension prediction.

In Fig. 5.18, the relationships between total suction and water content (main wetting paths) at fixed dry densities and two different temperatures (22°C and 80°C) have been plotted. Data at high suction values (between 8 MPa and 32 MPa) have been interpolated at constant dry unit weight using Fig. 5.12. Main wetting data at low suction values (under 0.50 MPa) and high temperature (80°C) are obtained from test series H14-SPx (constant volume swelling pressure test controlled with air overpressure technique) and test series H17-0.550, which develops very low swelling strains upon wetting and is representative of a quasi-constant volume test. Both techniques can be overlapped in main wetting paths showing the overall retention curve, where increasing temperatures caused drainage from the soil fixed matrix. The end of the main adsorption curves at 80°C is somewhat lower compared to the ending point of the main wetting curves at ambient temperature because of the lower gravimetric water storage capacity for the same soil packing at higher temperatures, mainly caused by water dilatation and possibly due to thermal expansion of entrapped air. Suction – degree of saturation retention curves at fixed packings and different temperatures (22°C and 80°C) are represented in Fig. 5.19 according to the procedure outlined before (interpolation at constant dry unit weight using Fig. 5.13 and air overpressure methodology in the low suction range).

Incorporating Eq. (5.5) into Eq. (5.3) results the empirical expression for water content or degree of saturation as a function of soil suction $s(w,T_f)$ at the observational temperature T_f:

$$\frac{w}{w_{sat}} = C(s)\left(\frac{1}{1+(\alpha_T s)^n}\right)^m \; ; \quad \alpha_T = \alpha\left(\frac{a_1 + b_1 T_r}{a_1 + b_1 T_f}\right)^{b_1} \quad \text{or} \quad \alpha_T = \alpha\left(G\frac{b(T_f - T_r)}{a + bT_r} + 1\right)^{-1} \tag{5.6}$$

where $C(s)$, n and m are considered temperature independent. However, She and Sleep (1998) estimated a small decrease in parameters n and m with increasing temperatures. As it is expected that $a_1 \rightarrow a/b$, $b_1 \rightarrow 1$ or $G(w) \rightarrow 1$ for high water content levels near the soil air-entry value, it is accurate enough to consider $b_1 = 1$ in the above expression. Retention curve data for both packings at high temperatures have been fitted to the proposed expression, maintaining parameters n and m according to Table 5.1. Fitted values of α_T for main wetting paths are between 24.27 MPa^{-1} and 25.81 MPa^{-1} for the low-density packing and between 1.232 MPa^{-1} and 2.732 MPa^{-1} for the high-density fabric. Values of a_1 (for $b_1 = 1$) are around $-(608\pm89)$ K, which are somewhat higher than the surface-tension prediction, in accordance with previous results reported by Grant and Salehzadeh (1996) and She and Sleep (1998) in the low suction range. G values are around (1.75 ± 0.49). As observed, Eq. (5.6) is adequate to fit retention curve data at different temperatures over a wide suction range. However, the temperature parameter α_T cannot be interpreted as representing only temperature dependence on contact angle or surface tension, but as an empirical fitting parameter.

5.1.7   Main wetting-drying cycles and first scanning wetting path obtained from suction controlled oedometer tests at different temperatures

5.1.7.1   Main wetting paths at different temperatures

Main wetting paths (matric suction versus water content) obtained from suction controlled oedometer tests at 22°C starting from an estimated suction of 1.9 MPa down to 0.01 MPa are represented in Fig. 5.20 (test series C17-xx on low-porosity packings) and in Fig. 5.21 (test series C14-xx on high-porosity fabrics). Gravimetric water content has been preferred as state variable instead of degree of saturation or volumetric water content due to the direct methodology that involves its determination, as well as because it is not sensitive to temperature changes (inflow / outflow mass of water is determined based on the direct measurement of the water volume change at a reference temperature). In addition, gravimetric water content changes in the form of the work conjugate strain variable $G_s/(1+e).\delta w$ appear as an appropriate extensive variable associated with matric suction stress variable, as discussed in section 6.1.2. Reference main wetting curves at 22°C and fixed packings with their respective equalised degrees of saturation are also plotted in the previous figures, where a tentative air-entry zone corresponding to a transition between a degree of saturation of 85% and 90% is identified. This transition, which accounts for the commencement of the occluded air saturation, appears as a singular zone in the wetting paths that has the maximum curvature. Although the term of air-entry is not strictly applicable in the wetting path, it will be used to indicate this transition in a similar way to the drying paths. Low-porosity packings initially try to follow the wetting paths corresponding to the denser fabric at constant porosity, but as the wetting process advances they diverge towards higher values of water storage as a result of soil swelling (refer to Fig. 5.20). This tendency is consistent with the greater swelling strains that are detected in the less loaded samples, which are the ones that retain a greater amount of water, showing a fully coupled poromechanical behaviour. The evolution of the degrees of saturation are also indicated in the figure, where a tendency to arrive to complete saturation is observed at low matric suctions (only test series C17-0.085 performed on 20-mm high sample in the lateral stress cell showed somewhat lower degree of saturation when arriving to the minimum matric suction).

Similar results are obtained in Fig. 5.21 when performing main wetting paths and following the same sequence on high-porosity packings. Major differences refer to the meta-stable-structured packing with collapsible tendency, displaying certain swelling in the first wetting first stages associated with a water retention higher than that corresponding to the fixed low-porosity structure, and following with collapse in later stages, which is associated with a smaller water storage. Final water retention remains

between both fixed packings, where the more loaded samples developing higher collapsing strains tend to lower storage capacities. Thus, changes in water content are strongly coupled to the swelling and collapse characteristics developed upon wetting due to the different applied stresses. Fig. 5.22 shows main wetting paths at 22°C obtained from isotropic tests (test series I17-xx and I14-xx) performed on the mini-isotropic and triaxial cells, following the same wetting sequence and displaying similar features of behaviour. However, lower values of the final degree of saturation are achieved when testing with the double drainage system used in the triaxial cell due to air entrapment. This condition becomes more evident when departing at low saturation levels, which is the case of the high-porosity packing.

Approximate water retention values for the different main wetting paths can be derived by linear scaling the main wetting curve for a fixed packing. Retention curves derived in this way may display the same air-entry value corresponding to the selected packing at a specified void ratio e_{ref}. Linear scaling of the actual water content $w(e,s)$ can be expressed as follows:

$$\frac{w(e,s) - w_{ref}}{w(e_{ref},s) - w_{ref}} = \frac{\dfrac{e}{Gs} - w_{ref}}{\dfrac{e_{ref}}{Gs} - w_{ref}} \;; \; w(e,s) = \frac{w_{sat}\left[1 + (\alpha s)^n\right]^{-m} - w_{ref}}{\dfrac{e_{ref}}{Gs} - w_{ref}}\left(\frac{e}{Gs} - w_{ref}\right) + w_{ref} \qquad (5.7)$$

where $w(e_{ref},s)$ is the water content of the reference wetting curve estimated by Eq. (5.3) assuming $C(s) = 1$ at the same soil suction s, e_{ref}/Gs is the water content at saturation of the reference packing, e/Gs is the saturated water content at the actual void ratio e, and w_{ref} is a reference water content towards which all the packings converge. Predicted retention curves for the high-density packings based on swelling strains developed during wetting are presented in Fig. 5.23 (reference curve: e = 0.591 packing). This figure also shows predicted curves for the high-porosity test series with collapsing trend based on a reference packing of e = 0.932. Greater deviations from measured values are detected at high net vertical stresses, where the high-porosity packing tends to the high-density fabric upon initial compression (the air-entry zone is shifted towards higher values after this initial macroporosity reduction). A similar procedure can be applied to Fig. 5.8, where suction – degree of saturation retention curves at different packings can approximately be obtained by linear scaling a reference curve with constant packing. Linear scaling of main drying volumetric water retention curve of a rigid soil in order to derive a hysteretic drying scanning curve has been used by van Dam *et al.* (1996).

Fig. 5.24 and Fig. 5.25 show main wetting paths obtained from suction and temperature controlled oedometer tests at 80°C (test series H17-xx and H14-xx), departing from an estimated matric suction of 1.6 MPa down to 0.01 MPa. Main wetting curves at 22°C and fixed packings with their respective equalised degrees of saturation and air-entry transition zones are also indicated for reference in the previous figures. Heavily overconsolidated packings at 80°C (refer to Fig. 5.24) display higher swelling strains and absorb larger amount of water when wetted, which are associated with somewhat higher degrees of saturation (calculated based on free water considerations and indicated in the figure) for the same suction if compared with results at 22°C. This way, the maximum curvature zone as previously defined is positioned at higher suction levels if compared to the air-entry zone at 22°C. Nevertheless, this tendency to absorb greater amount of water due to the higher swelling strains developed at 80°C is partially compensated with the thermal expansion that experiences the water at higher temperatures. At higher net vertical stresses and consequently lower volumetric changes, this trend is reversed in part due to the smaller storage capacity of water mass that offers the hotter soil.

Meta-stable structured packings at 80°C (refer to Fig. 5.25) present similar retention curves if compared to results at ambient temperature. Main differences refer to the lower storage capacity at high net vertical stresses as a result of higher compressive strains developed upon initial loading (refer to Fig. 6.39) and also linked to the thermal expansion that experiences water at higher temperatures.

As observed, the amount of water stored in the packing is coupled to the mechanical behaviour followed by the sample upon initial compression and wetting.

5.1.7.2   *General aspects of main drying and first scanning wetting paths at different temperatures*

Main drying and first scanning wetting paths (matric suction versus water content) obtained from suction controlled oedometer tests at 22°C starting from a suction of 0.01 MPa up to 0.45 MPa and then reverted to 0.01 MPa are represented in Fig. 5.26 (test series C17-xx on low-porosity packings) and in Fig. 5.27 (test series C14-xx on high-porosity fabrics). Scanning wetting refers to the first wetting path after performing the main wetting – drying cycle, even if the scanning curve does not lie between the main drying and main wetting curves. Reference main drying paths at fixed packings, as well as degree of saturation evolution in drying paths, are also shown in the figures, where a tentative air-entry or maximum curvature zone corresponding to the beginning of desaturation (between an estimated degree of saturation of 95% and 90%) is indicated. Equivalent main drying and scanning wetting paths performed on different packings under isotropic conditions are plotted in Fig. 5.28. Drying and wetting paths performed at 80°C on low-porosity overconsolidated packings are indicated in Fig. 5.29, while Fig. 5.30 shows equivalent drainage paths performed on high-porosity packings. In general, similar features of behaviour are observed for both packings subjected to different temperatures. Volume change behaviour associated with the different drying paths are presented in section 6.2.1 and section 6.3.1, highlighting the correspondence and coupling between shrinkage or suction consolidation and water content changes. In addition, hysteretic cycles (scanning wetting and drying paths) in terms of gravimetric water content changes and volumetric strains presenting similar features of behaviour are indicated in Fig. 6.7 and Fig. 6.34.

According to Fig. 5.31 the relationship between water content and the logarithm of matric suction is usually linear for initially saturated and normally consolidated soils with no external loads applied following a theoretical saturation line upon main drying (called VDL or virgin drying line by Toll, 1995), which is assumed to be related to the behaviour of saturated clays during consolidation (VCL: virgin compression line). Experimental results concerning volumetric and water content variations of clayey soils during drying – wetting cycles over a wide suction range are presented in Biarez *et al.* (1988) and Fleureau *et al.* (1993) starting from initially slurried soils. Shrinkage behaviour of compacted near-saturated soils is presented in Marinho and Chandler (1993) and Sitharam *et al.* (1995).

Provided that the soil remains saturated, the following relationship between water content changes δw and volumetric strain $\delta \varepsilon_v$ (or void ratio change δe) for an unloaded sample at an initial void ratio e_o holds: $\delta e = (1+e_o) \, \delta \varepsilon_v = Gs \, \delta w$. This way, the main drying path of a slurried soil will initially follow the normally consolidated isotropic compression curve or VDL (changes in water content result mainly from void ratio changes and an increase in suction is equivalent to an increase in effective stress), but tending to a constant void ratio as the water content decreases, where an increase in suction cannot result in a rearrangement of particles (shrinkage limit of the soil). This plastic process observed in slurried soils upon initial drying, where desaturation only occurs when a relatively rigid packing is achieved, is not detected when performing suction controlled tests on loaded overconsolidated packings and departing from near-saturated conditions, where an initially rigid response is detected (low water content changes and low volumetric strains with $Gs \, \delta w / \delta e \rightarrow 1$). However, between both extreme behaviours a singular point indicated in Fig. 5.31, which is usually not easy to detect experimentally, appears when matric suction is increased over the general air-entry value of the packing. At this point, the degree of saturation decreases very sharply due to the desaturation of the largest inter-aggregate pores, expelling water as air enters the soil and affecting the macroporosity of the packing (changes in water content result from both macro-void ratio changes and degree of saturation changes: $Gs \, \delta w / \delta e > 1$). Under these circumstances, an increase in the effective stress in a Bishop's sense of the quasi-saturated soil subjected to external loads is admitted, inducing high inter-aggregate forces with an obliquity exceeding the angle of friction between

aggregates, which can cause irreversible volume changes affecting in a poroplastic way soil behaviour (both simultaneous occurrence of plastic compressive strains and plastic water content changes associated with the main drying path). A conceptual picture of this behaviour is presented in Fig. 5.31. In addition, it appears also reasonable to admit that saturated aggregate shrinkage will try to follow the VDL for a slurry, as observed by Marinho and Chandler (1993), when testing clay/sand mixtures prepared on the wet side (near-saturated samples). This way, drying probably contributes to the enlargement of the macropores at expense of aggregate shrinkage (that remain saturated), which enables new macropore space for further rearrangement of soil structure. Based on this last concept a mathematical formulation using the inclined neutral line (associated with aggregate swelling/shrinkage behaviour) has been proposed by Alonso *et al.* (1994) to scale microstructural elastic deformations associated with changes in $(\sigma_m-u_a)+(u_a-u_w)$. However, lack of experimental results does not confirm the presence of an inclined suction increase SI yield surface with a negative slope. Recently, Sivakumar and Ng (1998) detected a somewhat inclined SI yield curve at a positive angle in the net mean stress : suction space for drying processes following an inundation path.

Whatever it is the mechanism that acts on soil macro-structure, it appears that the effect of matric suction is widely related to soil desaturation, occurring the maximum compressibility (both in water content and volumetric sense), when the quasi-saturated packing approaches and remains in this air-entry zone (Fig. 5.26 to Fig. 5.30).This situation is clearer detected in the high-porosity packings (refer to Fig. 5.27 and Fig. 5.30), where the drying paths cover a wider range of water content changes. This aspect is also more evident at 80°C, where higher degree of saturation changes in a free water sense are detected upon drying, which are associated with higher water content changes and higher shrinkage strains. It is also important to emphasise that H14-SP test does not display irreversibility in water content in consistency with the null global volumetric change condition of the swelling pressure test (further aspects are discussed in section 6.5.2).

Fig. 5.32 shows main drying and scanning wetting paths results for the different packings and temperatures in terms of Gs.w (Gs.w provides a representation of the water content with reference to the volume of the solid phase) and matric suction. The ends of the scanning wetting curves differ from the starting point of the main desorption curves because of irreversible shrinkage affecting storage capacity. According to this figure, water volume changes associated with macropore desaturation after passing the air-entry value are somewhat higher than those corresponding to the volume of water expelled by mechanically compressing a saturated soil (VDL dashed lines in Fig. 5.32). In general, water content changes in the air-entry zone are higher than those ones corresponding only to void ratio changes, where the progressive tendency of macropore desaturation is stated (refer to the conceptual frame of Fig. 5.31). Further aspects of the uniqueness (at least under nearly saturated states) of the virgin drying line in the e – intergranular stress plane are presented in Fig. 6.66. Reversible elastic water content changes associated with the scanning paths are discussed in section 6.2.1.2 and section 6.3.2 in a parallel framework to reversible microstructural strains.

It is supposed that whenever matric suction increases over the suction corresponding to the air-entry zone, which bounds the transition between the elastic state from the virgin state, both irreversible strains and water content will begin to develop from this suction loading. This way, as a preliminary choice for drying processes following a main inundation stage, it is adequate enough to admit a plane bounding surface that would be associated with the air-entry value of the original packing and not with the maximum suction ever experienced by the dry-side sample compaction. It is expected that this maximum suction is not a permanent feature of the soil and is substantially influenced by the main inundation stage. The air-entry value is also modified in a main wetting path by two different causes: the closing of the original fabric (macrostructural hardening) originated by the collapse of the meta-stable macrostructure due to aggregate distortion and sliding into a denser packing under confined stress (dragging of the loading-collapse LC yield curve defined in Alonso *et al.*, 1990) and that is associated with a higher desaturation value; or to the swelling of the macrostructure due to aggregate expansion (dragging of the suction decrease SD yield curve as defined in Gens, 1993) that originates an overall macrostructural softening associated with a lower air-entry value. This suction

increase or air-entry yield-locus is dragged along as the soil is dried, reaching a maximum suction ever experienced by the soil upon main drying. This way, the effect of drying or suction consolidation is similar to that of a mechanical overconsolidation, which depends of the drying level reached by the soil. Irreversible shrinkage at expense of inter-aggregate pores is limited to the shrinkage limit (refer to the suction increase hardening zone in Fig. 5.31). At higher suctions, the small pores at intra-aggregate scale are still quasi-saturated, while soil aggregates are confined by the application of high capillary forces that inhibit further inter-aggregate sliding or rearrangement of the macrostructure (air-filled inter-aggregate voids with meniscuses formed at inter-aggregate contacts), and shrinkage is admitted to be mainly associated with reversible intra-aggregate drying. It is also postulated that in this high-suction range there is hardly any hysteresis between the drying and wetting.

During scanning wetting the degree of saturation increases tending to Sr$\rightarrow$ 100%, while both void ratio and water content vary very little, since pores in overdried soils (a term originally proposed by Toll, 1995) are smaller and less water will enter upon re-saturation. The hysteresis arises therefore from plastic strains, which affect the topology of the macroporosity network. The simultaneous occurrence of volumetric plastic strains and plastic volumetric water content changes associated with drying paths has been mathematically formulated using a hardening poroplasticity unifying approach by Dangla *et al*. (1997). However, their theoretical formulation based on the physical interpretation of soil water retention curve hysteresis caused by pore structure effects was not contrasted with experimental data.

5.2   Water Permeability Determination under Controlled Suction

5.2.1   Introduction. Unsaturated flow equations. General aspects

Measurements of the hydraulic conductivity have been performed using the oedometer cells under controlled matric suction (both wetting and drying paths) and under constant net vertical stress states or constant volume conditions. The hydraulic conductivity values were obtained from both inflow and outflow data using the expressions that are further described and the correction proposed by Miller and Elrick (1958) and Kunze and Kirham (1962), which takes non-negligible ceramic disc impedance into account. The inflow/outflow approach is an unsteady-state method based on the use of the pressure plate apparatus and initially developed by Gardner (1956) (only for outflow). A step matric suction decrease/increase is applied to the soil and the transient inflow/outflow of water is carefully measured with time and interpreted with a simplified resolution of Richards's equation. Experimental problems refer to impedance effects from ceramic disc, diffusion of air into the measuring system (refer to section 3.2.5) and free water evaporation (refer to section 4.5.2).

Experimental methods for determining water coefficient of permeability are described in Vicol (1990), Fredlund and Rahardjo (1993) and Jucá and Frydman (1996). Three methods have been widely used: steady-state methods under constant hydraulic head gradient (Corey, 1957; Klute, 1965 and recently used by Fleureau and Taibi, 1995 and Huang *et al*., 1995); instantaneous profile methods in the high suction range (Daniel, 1982 with thermocouple psychrometers; Ed Diny *et al*., 1993 and Bentoumi and Alimi-Icholal, 1996 with filter papers); and pressure plate outflow/inflow tests. Jucá (1993) determined the permeability coefficient from outflow data obtained from tests on unsaturated clays performed in oedometer cells under vertical stress and suction control by axis translation. Ed Diny *et al*. (1993) determined hydraulic conductivity from outflow data caused by air overpressure acting on triaxial samples. Vicol (1990) and Delage *et al*. (1992) also used outflow data from a suction controlled oedometer cell (osmotic technique). Angulo-Jaramillo *et al*. (1993) used an Eulerian description of water flow and solid particles movement for estimating soil hydraulic conductivity in a deformable porous medium, coupled to the use of dual gamma attenuation technique and tensiometers.

The governing equation for one-dimensional transient water flow for unsaturated soil is given by Richards (1931) (refer to Vicol (1990) for further details) as:

$$\frac{\partial(\rho_w \theta)}{\partial t} = -\frac{\partial(\rho_w q_w)}{\partial z} + g; \quad q_w = -k_w(\psi_m)\left(\frac{\partial \psi_m}{\partial z} + 1\right)$$

$$\frac{\partial \theta}{\partial t} = C(\psi_m)\frac{\partial \psi_m}{\partial t} = \frac{\partial}{\partial z}\left[k_w(\psi_m)\left(\frac{\partial \psi_m}{\partial z} + 1\right)\right] + \frac{g}{\rho_w}; \quad \text{for constant } \rho_w$$

(5.8)

where θ is the volumetric water content ($\theta = n.Sr = Gs.w/(1+e)$), t the time, z refers to the vertical co-ordinate taken as positive upward, q_w the volumetric water flux $[LT^{-1}]$, g the water sources/sinks $[ML^{-3}T^{-1}]$ (g = 0 for the following analysis), ψ_m the soil water pressure head given as $\psi_m = u_w/\gamma_w$ [L], $k(\psi_m)$ the unsaturated permeability $[LT^{-1}]$, and $C(\psi_m) = d\theta/d\psi_m$ the soil water (capillary) capacity $[L^{-1}]$. The gravitational potential can be considered negligible for the present study (small thickness of the sample: $\partial \psi_m/\partial z \gg 1$), which is equivalent to admit $\partial k_w/\partial z \to 0$, simplifying the above expression to a diffusion equation. If the variable $D_w(\psi_m) = k_w(\psi_m)\partial \psi_m/\partial \theta$ (capillary diffusivity, $[L^2 T^{-1}]$) is introduced (Gardner, 1956), then the last expression of Eq. (5.8) transforms to:

$$\frac{\partial \theta}{\partial t} = C(\psi_m)\frac{\partial \psi_m}{\partial t} = \frac{\partial}{\partial z}\left[D_w(\psi_m)\left(\frac{\partial \theta}{\partial z}\right)\right]; \quad \frac{\partial \psi_m}{\partial t} = \frac{\partial}{\partial z}\left(D_w(\psi_m)\frac{\partial \psi_m}{\partial z}\right) = D_w\frac{\partial^2 \psi_m}{\partial z^2}$$

(5.9)

where the second expression is obtained assuming a linear relationship between volumetric water content and matric potential: $\theta(\psi_m) = a + b.\psi_m$ (or $\theta(u_w) = a + b_1.u_w$), which is valid for a small water pressure increment/decrement. The inflow/outflow method is also based on the assumption that the water permeability k_w (or diffusivity D_w) is constant over the small step change in water pressure (or small change in water content). This last assumption is generally not valid, but makes experimental data easier to analyse.

The initial and boundary conditions in the controlled inflow/outflow test are mathematically expressed as:

$\psi_m(z,t) = \psi_o \quad \text{for} \quad t = 0 \quad \text{and} \quad 0 \le z \le L$

$\psi_m(z,t) = \psi_o + \Delta\psi \quad \text{for} \quad t > 0 \quad \text{and} \quad z = 0$

$\left.\dfrac{\partial \psi_m}{\partial z}\right|_{z=L} = 0 \quad \text{for} \quad t > 0 \quad \text{and} \quad z = L$

where L is the height of the sample in which z = 0 is taken at the bottom. The initial condition corresponds to zero water velocity across the sample for which the water pressure head is constant. The last boundary condition expresses zero water velocity at the top of the sample. These boundary conditions reflect the physical characteristics in the test in which water at a pressure head of $\psi_o + \Delta\psi$ enters from the bottom and only air (no water) is allowed to enter at the top.

Gardner (1956) and Vicol (1990) integrated the Fourier's series solution of $\psi_m(z,t)$ on the volume of the sample in order to obtain the amount Q(t) of intruded/extracted water at time t:

$$\frac{Q(t)}{Q_o} = 1 - \frac{8}{\pi^2}\sum_{m=0}^{\infty}\frac{1}{(2m+1)^2}\exp\left(-(2m+1)^2 \pi^2 \frac{D_w t}{4L^2}\right)$$

(5.10)

where Q_o is the total amount of intruded/extracted water in a suction step $[L^3]$ and L the sample height.

Miller and Elrick (1958) and Kunze and Kirham (1962) introduced the ratio of soil to ceramic plate impedance by means of the following expression used to analyse measured inflow/outflow data:

$$\frac{Q(t)}{Q_o} = 1 - \sum_{n=1}^{\infty} \frac{2\exp\left(-\alpha_n^2 D_w t/L^2\right)}{\alpha_n^2 \left(a + \csc^2 \alpha_n\right)} \tag{5.11}$$

where Q_o is the total inflow/outflow for a water pressure increment/decrement $[L^3]$, Q the inflow/outflow at any time, L the soil height, a the ratio of impedance of the ceramic disc to the impedance of the soil $a = z_m/z_s = k_w e/(Lk_d)$ (e is the ceramic disc thickness and k_d its water permeability), and α_n the nth solution of the equation $a\alpha_n = \cot\alpha_n$ (for n = 1, 2,...). The solution involves a new boundary condition of equality of flow through the ceramic disc and the soil, through the following expression: $k_w\left(\partial\psi_m/\partial z\right)\big|_{z=0} = \left(\psi_o + \Delta\psi - \psi_m(0,t)\right)k_d/e$ for t > 0 and z = 0, which reduces to $\psi_m(0,t) = \psi_o + \Delta\psi$ for t > 0 when $e \to 0$ or the impedance $a \to 0$. For the case of a = 0 with low ceramic disc impedance, $\alpha_n = (2n-1)\pi/2$ (n = 1, 2,...), which results in an equivalent expression to Eq. (5.10). For $a \to 0$ and values of $t \geq \ln(100/9)L^2/\left(2\pi^2 D_w\right)$, the second term of the series is less than 1% of the first term. The above expressions are subjected to a number of simplifications and assumptions: the soil matrix is rigid, the water flow is isothermal and one-dimensional, the fluid is homogeneous and incompressible and the flow of air in the porous medium is neglected or considered to be instantaneous.

A non-linear, least-squares optimisation procedure is used to approximate test readings (time evolution of inflow/outflow data: $Q(t)/Q_o$) to model predictions according to Eq. (5.11) (the first two terms of the series have been considered). The idea is to choose D_w parameter with adequate restrictions on $0 < \alpha_1 \leq \pi/2$ and $\pi/2 < \alpha_2 \leq 3\pi/2$, such that the sum of the squared deviations of the measured data from the calculated data be minimised. The minimisation problem of the objective function is carried out using the Solver utility from Microsoft®Excel. The optimisation procedure of Eq. (5.11) has been contrasted with the equivalent expression for null impedance ratio (Eq. (5.10) with six terms of the Fourier's series). Water permeability k_w is calculated from the following expression:

$$k_w = \frac{D_w \delta\theta_w}{\delta\psi_m} = \frac{D_w \gamma_w Q_o}{V\delta u_w} \tag{5.12}$$

where δu_w is the water pressure increment/decrement and V the volume of the sample.

Impedance ratio effects on water permeability determined on the same $Q(t)/Q_o$ evolution are evaluated in Fig. 5.33 for different suction steps (main wetting path) performed on test series C17-0.085B (lateral stress cell). In general, values of a < 0.10 do not present an important effect on water permeability determinations and Eq. (5.10) for negligible membrane impeded flow can be used to evaluate the hydraulic conductivity. According to Fig. 3.17, the ceramic disc impedance of the lateral stress cell varied between $z_m = 99.2\times10^6$ s (measured in September 1995) and $z_m = 1.83\times10^9$ s (registered in February 1997) due to disc clogging, which is associated with impedance ratios of around $0.007 \leq a \leq 0.429$ and correction factors of $1.04 \leq k_w(a \geq 0)/k_{w\min}(a = 0) \leq 2.24$. The optimisation procedure of Eq. (5.11) has also been verified with the approximate expression proposed in Vicol (1990) for the correction factor based on an impedance ratio for a reference point time:

$$\frac{k_w(a \geq 0)}{k_{w\min}(a = 0)} = \frac{\pi^2}{4\alpha_1^2} \tag{5.13}$$

where α_1 is the solution of the equation $a\alpha_1 = \cot\alpha_1$. Special care has been taken for assessing adequate ceramic disc impedance when computing water permeability values at high temperatures where disc-clogging effects are of certain consideration.

Data is usually evaluated using inflow/outflow results that do not exceed 30% of the total change ($0.20 \leq Q(t)/Q_o \leq 0.30$) associated with the step change in water pressure. Under this short period the diffusivity and soil volume are not constant, but sufficiently to satisfy theory. Influence of the cut-off percentage on permeability determination has been evaluated and only permeability values maintained within a maximum deviation of $\left. \left| k_w \right|_{Q(t)/Q_o=0.20} - k_w \right|_{Q(t)/Q_o=0.30} \left| \middle/ k_w \right|_{Q(t)/Q_o=0.20} \leq 0.15$ are considered.

Steady-state corrections for air diffusion and soil water evaporation in main drying paths under nearly saturated conditions and for both soil packings at different temperatures are presented in Fig. 5.34. Volumetric evaporative fluxes, which decrease with increasing matric suction and lower water availability within the soil and increase at higher temperatures, have been fitted to the Dalton-type surface boundary condition expressed by Eq. (4.15) that assumes a common saturation vapour pressure for both air above the evaporating surface and air within the soil matrix. High values of relative humidity in the air chamber above the soil surface are observed (h_{ra} = 99.47% at 22°C and h_{ra} = 99.54% to 99.57% at 80°C), which ensure an adequate matric suction equalisation (refer to section 4.5.2). The value of the exchange function under nearly saturated conditions is around $f_v = 6.173 \times 10^{-3}$ mm/(s.MPa) at 80°C, which is somewhat higher than the value reported in section 4.5.2 for main wetting paths, indicating some possible dependence on degree of saturation. Evaporative fluxes for two different temperatures measured under low matric suction values $(u_a - u_w) \leq 0.06$ MPa have been represented as a function of soil porosity, where a clear trend of increasing evaporative fluxes with increasing porosity is detected at high temperatures. Considering the tested soil equivalent to a macro-element and the dominant Fickian molecular diffusion of vapour in air expressed as (Nassar and Horton, 1989; Wilson *et al.*, 1994): $E_v\rho_w = -\beta\tau D_m^w \nabla u_v$ (where $E_v\rho_w$ is the gravimetric water vapour flux measured at a reference temperature of 22°C; $\beta = n(1\text{-Sr})$ the cross sectional area available for vapour flow; τ the tortuosity factor; D_m^w the molecular diffusivity of vapour in air; and u_v the vapour pressure), it appears that the tortuosity factor which accounts for pore geometry complexities is proportional to $\tau \propto n^{0.34}$ (refer to high temperature data in the previous figure). This exponent is somewhat lower than that proposed by Lai *et al.*(1976) of $\tau \propto n^{2/3}$.

Air diffusion through ceramic disc is dominant at high-applied matric suction values and high temperatures. However, diffused-air flow rates across a unit area under nearly saturated conditions are lower than the corresponding ones of main wetting paths (refer to Fig. 3.19, which are normalised by a unit area of disc voids). This fact puts forward as evidence the retarding effect of the nearly saturated soil matrix that acts as a prolongation of the ceramic disc inducing lower pressure gradients as defined by Eq. (3.16). Reported data can be used to determine diffusion parameters of air through pore water at different temperatures according to the expressions detailed in section 3.2.5, assuming nearly saturated conditions with occluded air and that air movement is essentially by diffusion through water phase of both soil and ceramic disc. According to the data presented in Fig. 5.34 under $(u_a\text{-}u_w)$ = 0.45 MPa, the flow rate of diffused air across a unit area of voids (an average porosity of 0.35 is assumed for both ceramic disc and soil) is around $\delta V_d/\delta t \approx 3.7 \times 10^{-7}$ (mm³/s)/mm² at 22°C and $\delta V_d/\delta t \approx 1.0 \times 10^{-6}$ (mm³/s)/mm² at 80°C. These values correspond to an overall diffusion coefficient of around $D_o \approx 1.1 \times 10^{-10}$ m²/s at 22°C (h = 0.019, u_{db} = 0.15 MPa, δu_d = 0.45 MPa, and δz = 17.4 mm for both ceramic disc and soil), and somewhat higher $D_o \approx 3.9 \times 10^{-10}$ m²/s at 80°C (h = 0.015), which are smaller than the corresponding values for diffusion of air in free water (2.2×10^{-9} m²/s) in accordance with the expected reduction due to the tortuosity of the path. Corrected diffusion coefficients through the compacted soil D_s can be estimated from the following expression equivalent

to an effective permeability for stratified soils that assumes a common reference absolute pressure u_{db}: $L/D_s = (L + e)/D_o - e/D_c$; where $L \approx 10$ mm is the soil thickness, e = 7.4 mm the ceramic disc thickness and D_c the coefficient of diffusion through the ceramic disc ($D_c \approx 8.6 \times 10^{-11}$ m²/s at 22°C and $D_c \approx 2.0 \times 10^{-10}$ m²/s at 80°C, according to Fig.3.19). A value of $D_s \approx 1.4 \times 10^{-10}$ m²/s is obtained at 22°C, which is of the same order of magnitude to that reported by Barden and Sides (1967) on clayey soils, and somewhat higher $D_s \approx 1.3 \times 10^{-9}$ m²/s at 80°C. The increase of diffusivity with increasing temperature, which corresponds to certain expected reduction in the viscosity of soil water, could not be compared with other reported results due to the absence of tests (to the author's knowledge) performed at different temperatures.

5.2.2   General aspects and testing results of partial saturation and porosity effects on water permeability at two different temperatures

Classified water permeability values are represented in Fig. 5.35 (at 22°C) and in Fig. 5.36 (at 80°C) for different degrees of saturation and void ratios. An adequate value of e and Sr to be used for the identified k_w value is, in view of the small amount of moisture and volume change which is assumed when considering $0.20 \le Q(t)/Q_o \le 0.30$, that of a weighted value tending to the preceding equalisation value for suction steps in main wetting paths ($0.85Sr_o + 0.15Sr_f$) and a mean value between steps for the main drying and scanning paths. Contour levels representing constant void ratio values were obtained from scattered data using polynomial regression defined by a maximum Sr order of 2 and a maximum (log k_w) order of 1. Surface fitting results are:

$$e = -0.517 - 0.134 \log k_w + 6.65 Sr + 0.539 Sr \log k_w - 0.850 Sr^2 \text{ at } 22^o C$$
$$e = -0.674 - 0.151 \log k_w + 6.86 Sr + 0.572 Sr \log k_w - 0.676 Sr^2 \text{ at } 80^o C$$

(5.14)

where k_w is expressed in m/s.

Certain effect of the temperature is observed in Fig. 5.36, where solid contour lines obtained from water permeability results at 80°C are compared to dashed contour lines representing equivalent conditions in terms of void ratio at 22°C. In general, this temperature effect is more important at near-saturated conditions, whereas below a degree of saturation of 70% no clear trend appears. In addition to the important dependence of water permeability on degree of saturation and temperature, a high void ratio dependence is also observed (as expected for the wide range of clayey soil structure if compared to sands or silts, which present a more fixed packing), which appears to increase up to a certain limit with decreasing degree of saturation. In order to observe this trend, the water permeability values at 22°C have been conveniently grouped in approximately constant degree of saturation values and plotted versus void ratios, as shown in Fig. 5.37. At a degree of saturation of around (95 ± 5)% and 22°C, coefficient of permeability with respect to water presents a variation between $k_w = 7.9 \times 10^{-12}$ m/s at e = 0.90 and $k_w = 2.2 \times 10^{-12}$ m/s at e = 0.60, whereas at a smaller degree of saturation of (75 ± 5)% this same void ratio variation is associated with a change of water permeability between $k_w = 2.7 \times 10^{-12}$ m/s and $k_w = 3.0 \times 10^{-13}$ m/s. This last variation of over one order of magnitude is as important as a change in degree of saturation between 75% and 50% for a fixed packing of e = 0.90. Similar conclusions with respect to the important void ratio dependence can be deduced from water permeability results at 80°C presented in Fig. 5.38. This last consequence is very important, since the greater water permeability change is usually associated with the saturation degree, because most of experimental determinations found in the literature correspond to low activity soils that underestimate packing variations. Water permeability values at nearly saturated conditions (Sr ≈ (95±5)%) are compared with those obtained from consolidation data (refer to Fig. 2.36), where a good agreement is obtained when checking different indirect methods.

Temperature effects on water permeability associated with high degrees of saturation (at an average degree of saturation of 75% there are no appreciable effects) are also shown in the previous figure and

compared to equivalent results at 22°C (represented by dashed lines). The slight increase of permeability with temperature at $Sr \approx (95\pm5)\%$ of $k_w(80)/k_w(22)|_{Sr,e} \approx 1.25$ cannot be solely explained in terms of the reduction of free water viscosity in the same interval of temperature, which is also represented in the same figure.

As observed from the previous results water permeability is a function of void ratio, water content (degree of saturation), temperature and soil or water structure, where the last aspect incorporates thermo-chemical effects altering clay fabric (flocculation or dispersion), effects on pore sizes and shapes and changes that occur as a result of pore fluid chemistry alteration. Usually the general form of permeability with respect to a reference configuration (e_o, w_{sat}, T_o) is admitted to be decoupled: $k_w(e,w,T)/k_w(e_o,w_{sat},T_o) = k_T(T)k_e(e)k_r(w)$, where k_r accounts for water retention in the soil (the saturated state is the reference configuration), k_e quantifies the effects of void ratio changes (or porosity changes) and k_T for pore water property changes induced by temperature (the reference state is usually the ambient temperature). However, these functions are not totally independent and porosity (even if maintained constant) may have important consequences on k_r water relative permeability that is admitted only to be a function of the gravimetric water content (refer to Fig. 5.41). In addition, different degrees of saturation (even if maintained constant) may effect the temperature function k_T as previously shown in Fig. 5.38 (decreasing $k_w(80^\circ C)/k_w(22^\circ C)|_{Sr,e=0.80}$ values with decreasing degrees of saturation) or the porosity function k_e as indicated in Fig. 5.37 (increasing $k_w^{-1} \delta k_w/\delta e|_{Sr,T}$ values with decreasing degrees of saturation).

The relative water permeability k_r for constant porosity and temperature follows the general relation:

$$k_r(w) = \frac{k_w}{k_{ws}}\bigg|_{e,T} = S_e^{\lambda} \; ; \quad S_e = \frac{w - w_{res}}{\dfrac{e}{Gs} - w_{res}} = \frac{Sr - \dfrac{Gs.w_{res}}{e}}{1 - \dfrac{Gs.w_{res}}{e}} = \frac{\theta_w - \dfrac{Gs.w_{res}}{1+e}}{n - \dfrac{Gs.w_{res}}{1+e}} \quad (5.15)$$

where k_{ws} is the saturated water permeability for the reference configuration; S_e the effective saturation ratio that can be evaluated on gravimetric water content, degree of saturation or volumetric water content (θ_w) bases; and λ an empirical constant usually related to the pore size distribution index (Brooks and Corey, 1964 in Leong and Rahardjo, 1997b). Mualem (1976) found that λ ranges from 2.5 to 24.5 (an exponent of 3 is related to a soil with a uniform pore-size distribution; Fredlund and Rahardjo, 1993). Subscript *res* refers to the residual gravimetric water content, which is defined as the water content at which an increase in total suction does not produce a significant change in it and is usually related to the hygroscopic water content.

The relative water permeability is studied as a function of the degree of saturation and for different constant porosity values. Fig. 5.39 shows relative water permeability values as a function of degree of saturation at a constant void ratio of around 0.60 and for different temperatures, where no appreciable temperature effects are observed. Fig. 5.40 indicates the equivalent plot for a constant void ratio of around 0.93. Relative permeability values have been fitted to Eq. (5.15), admitting a residual water content of $w_{res} = 2.2\%$ ($Sr_{res} = 10.1\%$ for the low-porosity fabric and $Sr_{res} = 6.4\%$ for the high-porosity packing). Complete saturation is admitted for normalising purpose, even in the main wetting paths corresponding to the high-porosity packings. Complementary data of relative water permeability versus degree of saturation at different temperatures and classified void ratios are presented in Fig. 5.41 following the same fitting criterion with reference to the residual water content, where a high dependence of λ on soil porosity is detected. This aspect suggests a modification of the empirical relative water permeability function with another reference gravimetric water content for normalising purpose, as indicated in the previous figure. Different reference gravimetric water contents up to a maximum of 14% corresponding to the weakly bonded diffuse-layer or intercluster water within

aggregations of clay particles were analysed, where a minimum reference water content of 13% is consistent with an approximately constant value of around $\lambda \approx 3$ and a relative water permeability of around 1%. This intercluster adsorbed water is indicated in the previous figures, which is associated with a region that separates zones of greater water relative permeability values from others presenting a restricted flow in a generalised Darcian sense.

A mobile-immobile concept has also been used to explain accelerated breakthrough in the case of steady state solute transport by van Genuchten and Wagenet (1989). Pusch (1982) found that for a bentonite-water mixture at separations of 10 Å to 20 Å, the water permeability is affected by the ordered structure of water. In clays with high percentage of adsorbed water associated with a smaller mobility of water adjacent to mineral surfaces, the relative water permeability with reference to hygroscopic humidity is drastically reduced (high λ values) if compared with free water dominant fabrics (low λ values). A mass transfer model in a rigid porous media for low-porosity clays has been proposed in Robinet *et al*. (1992), which considers a convective flow in a Darcian sense for capillary water and a Fickean diffusive transport for adsorbed water.

Water permeability appears to be governed by the size and distribution or contribution of interconnected filled macropores within soil structure as indicated in section 2.5.5, and predictive equations based on PSDs joined to MIP – retention curve relationships permit to reflect this dependence in terms of degree of saturation. This way, PSD or alternatively soil-water characteristic curve data can be used to evaluate the relative water permeability, according to the following expressions based on the general Eq. (2.26):

$$k_r(x_m) \propto \frac{\int_{x_{min}}^{x_m} x^2 f(x) dx}{\int_{x_{min}}^{x_{max}} x^2 f(x) dx} \; ; \quad k_r(Sr_{nw}) \propto \frac{\int_{Sr_{nw}}^{1} \frac{dSr_{nw}}{(p(Sr_{nw}))^2}}{\int_{0}^{1} \frac{dSr_{nw}}{(p(Sr_{nw}))^2}} \; ;$$

$$k_r(Sr) = S_e^n \frac{\int_{Sr_{res}}^{Sr} \frac{dSr}{(u_a - u_w)^{2+m}}}{\int_{Sr_{res}}^{1} \frac{dSr}{(u_a - u_w)^{2+m}}} \tag{5.16}$$

which assume a porous medium characterised by a pore diameter x and its pore size density function given by f(x) (the pores are considered correlated), as well as the Hagen-Poiseuille equation for laminar flow through cylindrical capillaries (the permeability is determined by integration over the contribution from the filled pores ranging from x_{min} to x_{max}, being MIP typical values around 6 nm to 100μm). In the third expression, the soil-water characteristic curve is considered analogous to the PSD (second expression) following the relationships presented in section 2.5.4. The term S_e^n, which is supposed to account for tortuosity, and the parameter m are correction factors to improve the prediction of the relative permeability based on statistical models (Mualem (1976) suggested n = 0.50).

Relative water permeability values estimated based on the numerical integration of the first expression of Eq. (5.16) as a function of the degree of saturation (calculated from MIP - retention curve relationships) are represented in Fig. 5.42. A similar trend is observed for both packings compared to relative water permeability values obtained under controlled suction (the high-porosity curve is located over the low-density curve). Relative water permeability values based on the numerical integration of the third expression (for n = 0 and m = 0) using the main drying degree of saturation – matric suction retention curve for both packings (refer to Fig. 5.9) are also represented in

the previous figure, where a poor model prediction is observed compared to suction controlled results (further improvements can be obtained incorporating different correction factors).

A reference cut-off water content can be arbitrarily chosen as the value when $k_w/k_{ws} \leq 0.01$, which is associated with a water content of around 13% as previously stated and that is consistent with the quasi-immobile water fraction within aggregations of clay particles determined from retention curve and MIP data (refer to section 5.1.1). Fig. 5.43 shows the normalised effective degrees of saturation with respect to this reference cut-off water content, where a parameter of $\lambda \approx 2.6$ adequately fits inflow/outflow experimental data corresponding to the different packings (normalised MIP data is shifted towards a somewhat higher value of $\lambda \approx 4.0$). As observed, estimations from pore volume considerations alone cannot be simply related to the relative permeability of the soil, and correction functions to take into account tortuosity of the flow and a partially correlated connection between cross sections are required. Nevertheless, these estimations demonstrate the dependence of relative permeability on retention curve and MIP data, as well as the consequences of degree of saturation changes.

The effects of void ratio (e) or porosity (n) changes with reference to an initial configuration (e_o or n_o) can be quantified as follows:

$$k_e(e)\big|_{w,T} = \frac{e^3}{(1+e)}\frac{(1+e_o)}{e_o^3} = \frac{n^3}{(1-n)^2}\frac{(1-n_o)^2}{n_o^3} \quad \text{or} \quad k_e(e)\big|_{w,T} = 10^{a(e-e_o)} \tag{5.17}$$

The first expression is derived from Kozeny-Carman equation for porous media (Das, 1983b), which is admitted to hold for saturated clays in terms of the effective porosity where only the larger inter-aggregate pores are considered (the flow through intra-aggregate pores can be neglected according to Fig. 2.29). In low-porosity saturated clays, the free water porosity should be considered as the effective porosity, since the adsorbed water porosity is filled with quasi-immobile water (Ma and Hueckel, 1992). Nevertheless, it has been preferred to include the different water mobility aspects in the relative permeability factor, as previously explained, and to maintain the total porosity or the total void ratio in the previous expressions. The second expression is suggested based on linear log k_w – e plots described in Lambe and Whitman (1979). A model for intrinsic permeability as a function of macroporosity depending on degree of saturation is described in Olivella *et al.* (1998) to take into account clay structural changes upon wetting, where a maximum macroporosity is assumed under dry conditions and tending to a minimum under saturated states.

Temperature effects on water permeability in saturated soils are usually interpreted based on viscosity changes under free water considerations, according to the following expressions:

$$k_T(T)\big|_{e,w} = \frac{\rho_w(T)\mu_w(T_o)}{\rho_w(T_o)\mu_w(T)} \approx 1 + \alpha_T(T - T_o); \quad T_o = 22^{\circ}C \tag{5.18}$$

where μ_w is the absolute viscosity and $\alpha_T \approx 0.030$ K^{-1} is an empirical coefficient that fits relative viscosity data over the temperature range of $22^{\circ}C \leq T \leq 80^{\circ}C$. Experimental data presented in Fig. 5.38, which show a temperature dependence smaller than could be expected from the thermal change in water viscosity, are associated with $\alpha_T \approx 0.004$ K^{-1} at nearly saturated conditions (Sr $\approx (95\pm5)\%$) and tending to $\alpha_T \rightarrow 0$ at lower free water availability (Sr $\approx (75\pm5)\%$). Possibly, the liquid permeability is somewhat overestimated due to some contribution of vapour movement (mainly at lower water contents) in the same direction as the liquid water flow. Although no detailed study has been performed on unsaturated soils that corroborates the information presented in this research, it is possible that the nature of soil fabric, clay particles and pore fluid chemistry change when heated, even though the total porosity and degree of saturation appear to have changed only slightly. However, for all controllable factors remaining constant, it appears correct to state that temperature effect on the viscosity of the permeant represents the dominant influence. Towhata *et al.* (1993) studied the effects of temperature on saturated kaolinite-clay up to 90°C using indirect methods,

where an additional temperature effect over that predicted based on free water considerations was observed (an estimated of $\alpha_T \approx 0.042$ K^{-1} is obtained from experimental data at a reference $T_o = 20°C$). This observation is contrary to Houston and Lin (1987) who observed a saturated water permeability on illite at 200°C lower than that of viscosity prediction. An increase in water permeability as high as one order of magnitude per 50°C of temperature increase has been observed in saturated Na-montmorillonites by Pusch (1986) (referred in Ma and Hueckel, 1993). Permeability measurements up to 120°C have also been performed on saturated montmorillonite by CIEMAT (Volckaert *et al.*, 1996a), where a value of around $\alpha_T \approx 0.014$ K^{-1} can be deduced from experimental data up to 100°C (dry density of 1.6 Mg/m^3 and reference temperature of 22°C). Recently, Khemissa (1998) reported careful direct measurements of permeability for a saturated kaolinite-clay up to 130°C, where an estimated of $\alpha_T = 0.010$ K^{-1} is obtained from experimental data up to 80°C departing from a reference of 22°C.

Experimental data of temperature effects on water permeability of unsaturated soils have been limited to low suction values and low target temperatures. Experimental results have been reported by Haridasan and Jensen (1972) on a silty loam up to a matric suction of 70 kPa and 35°C using steady state and pressure plate outflow methods. In these results, a somewhat greater temperature dependence seems to be observed at higher volumetric water contents (although this fact has not been reported by the authors) in accordance with Fig. 5.46. Hopmans and Dane (1986) tested a sandy loam using tensiometers up to a matric suction of 20 kPa and 45°C. In general, an increase in water permeability is detected at higher temperatures, which is not accounted for entirely by the temperature dependence of water viscosity. Higher values of permeability than predicted from viscosity changes can be interpreted assuming that the amount and cross section of free water in macropores increases, which is sustained on the concept that quasi-immobile adsorbed water contained in interstices smaller than 40 Å changes at around 70°C its nature to that of free water (Derjaguin *et al.*, 1986; Ma and Hueckel, 1993). The structural disturbance of this interlayer water lattice can consequently induce aggregate contraction upon heating due to a denser grouping of stacks of flakes leaving larger inter-aggregate voids between them that favour free water flow. Flocculation also occurs when temperature is increased in clays that have in their structure illite-mica (Almanza *et al.* 1995) and bentonite (Brandl, 1992), altering the nature of pores and creating preferential pathways for water flow.

Combining the different expressions, the following relationship is suggested:

$$k_w(e, w, T) = k_{wo}(1 + \alpha_T(T - T_o))10^{ae}\left(\frac{w - w_{ref}}{\dfrac{e}{Gs} - w_{ref}}\right)^\lambda ; \quad T_o = 22^o C \tag{5.19}$$

Water permeability results for the high-porosity packing at different degrees of saturation, different temperatures and approximately constant porosity are represented in Fig. 5.44. A non-linear curve-fitting algorithm using least-squares method have been implemented to determine the material parameters $k_{wo} = 2.00\times10^{-13}$ m/s, $\alpha_T = 4.31\times10^{-3}$ K^{-1}, a = 1.87 and λ = 2.40 for w_{ref} = 13%. The same parameters have been used to predict water permeability values for the high-density fabrics that are indicated in Fig. 5.45, where a quite good agreement is observed. Best-fit curves in terms of volumetric water contents (refer to Eq. (5.15)) and void ratios for the different packings are presented in Fig. 5.46 for both temperatures, where typical parameters similar to the previous ones are also indicated. The following restrictions are imposed to parameters $a \geq 0.434k_w^{-1}\delta k_w/\delta e\big|_{Sr=(95\pm5)\%,T}$ and

$\alpha_T \leq \left[k_w(80^o C)/k_w(22^o C)\big|_{Sr=(95\pm5)\%,e=0.80} - 1\right]/\Delta T$, according to classified data reported in Fig. 5.37 and Fig. 5.38.
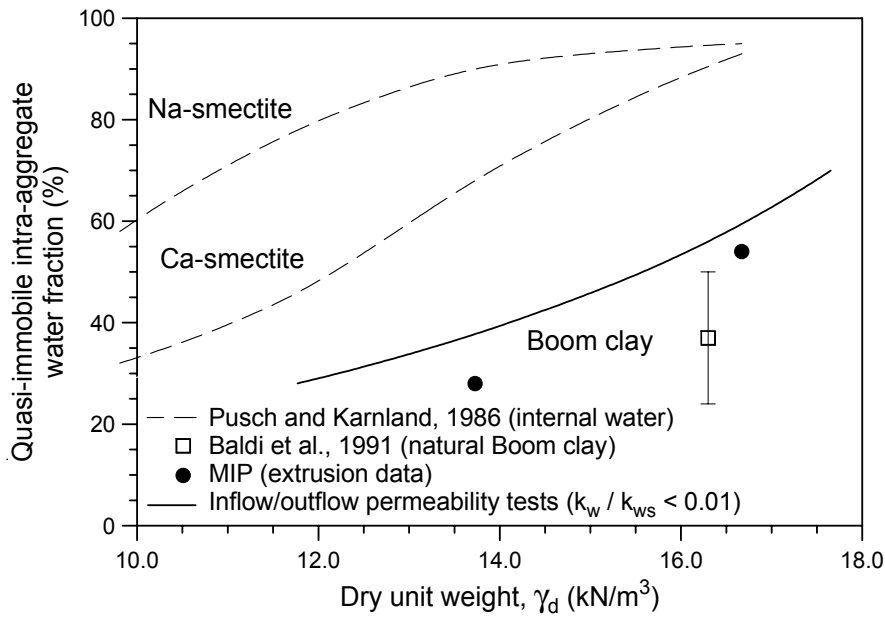
Figure 5.1   Quasi-immobile intra-aggregate water fraction (% of total pore volume).
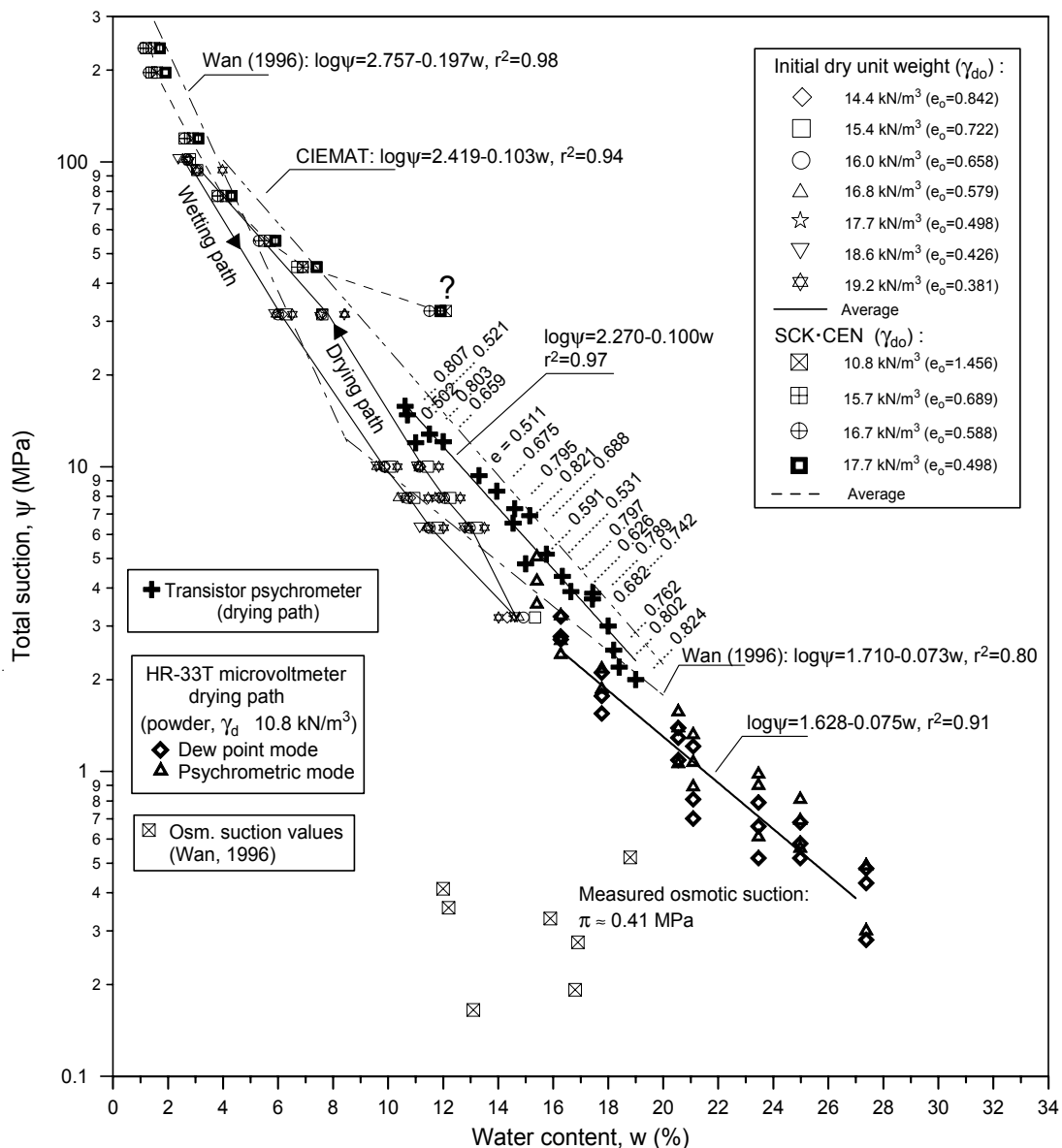
Figure 5.2   Soil water potential relationships for different initial dry unit weights at 22°C.
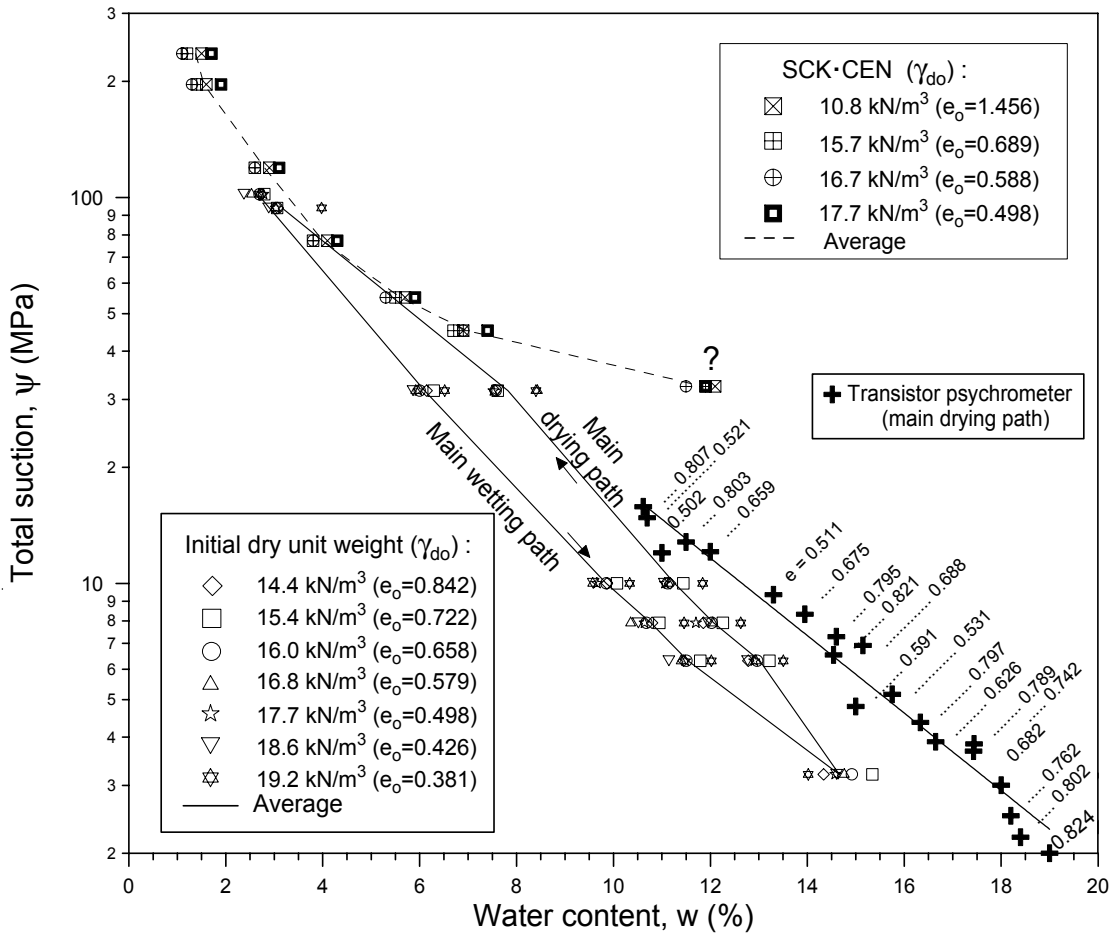
Figure 5.3   Zoom of the previous figure.
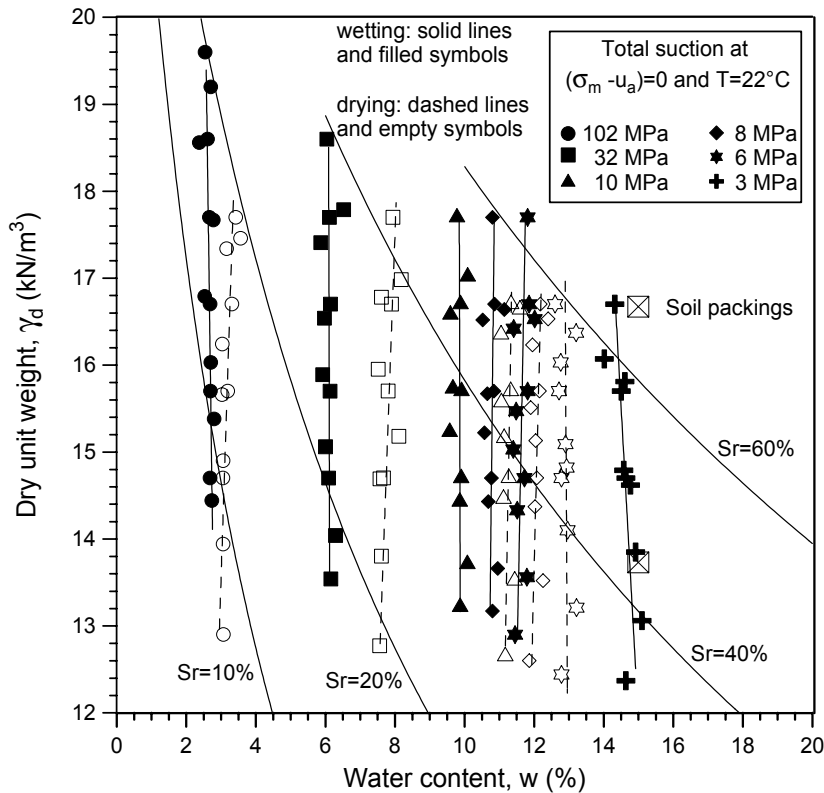
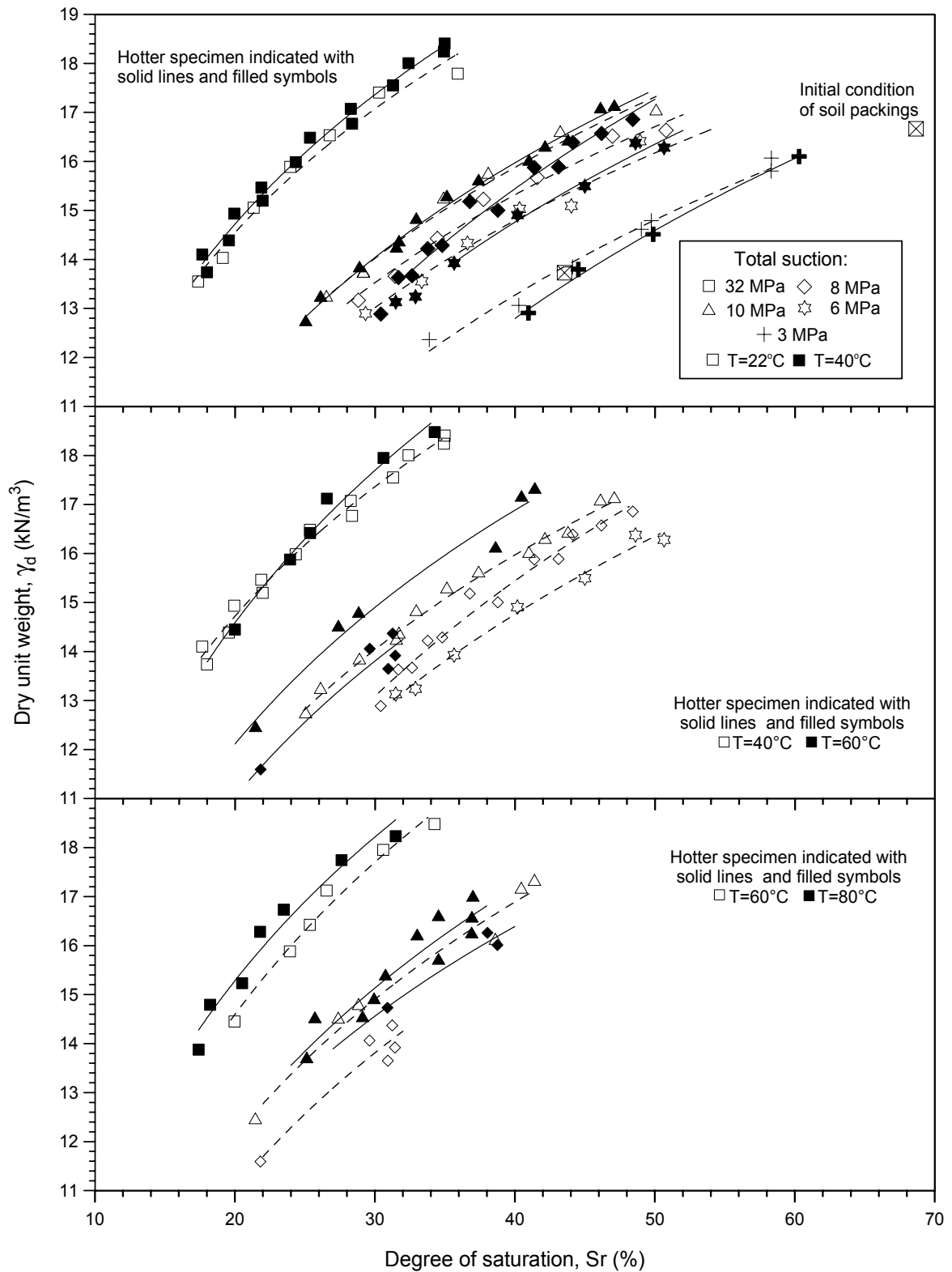Figure 5.4   Dry unit weight-degree of saturation values after total suction equalisation in main wetting and drying paths.
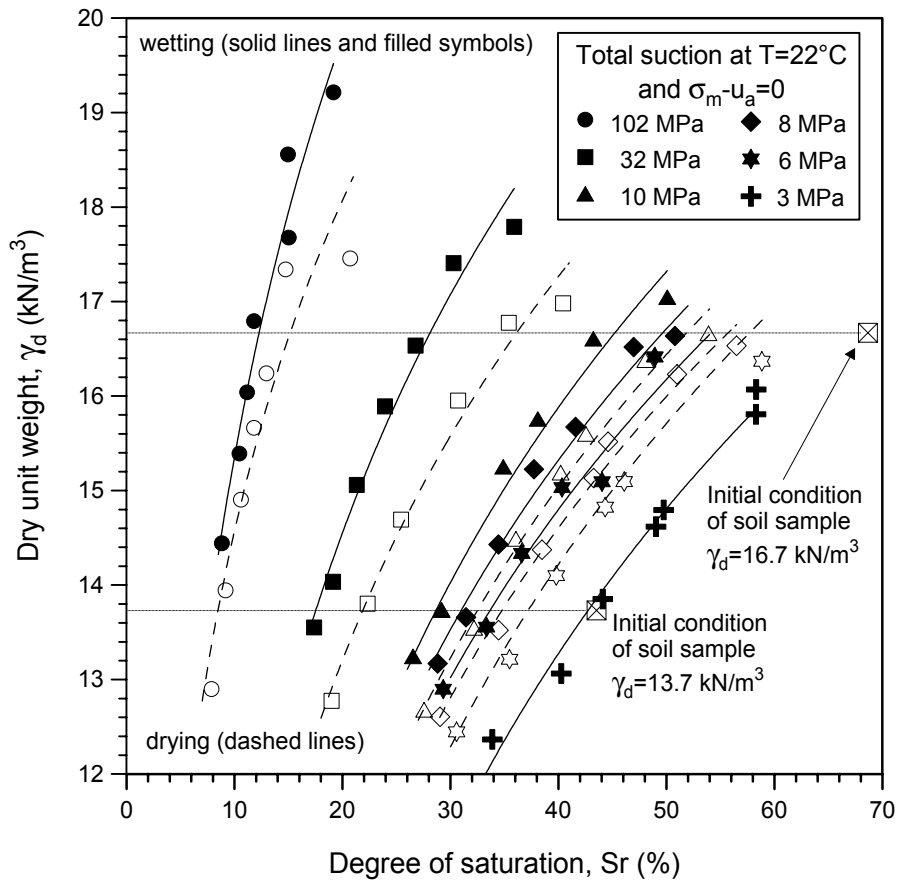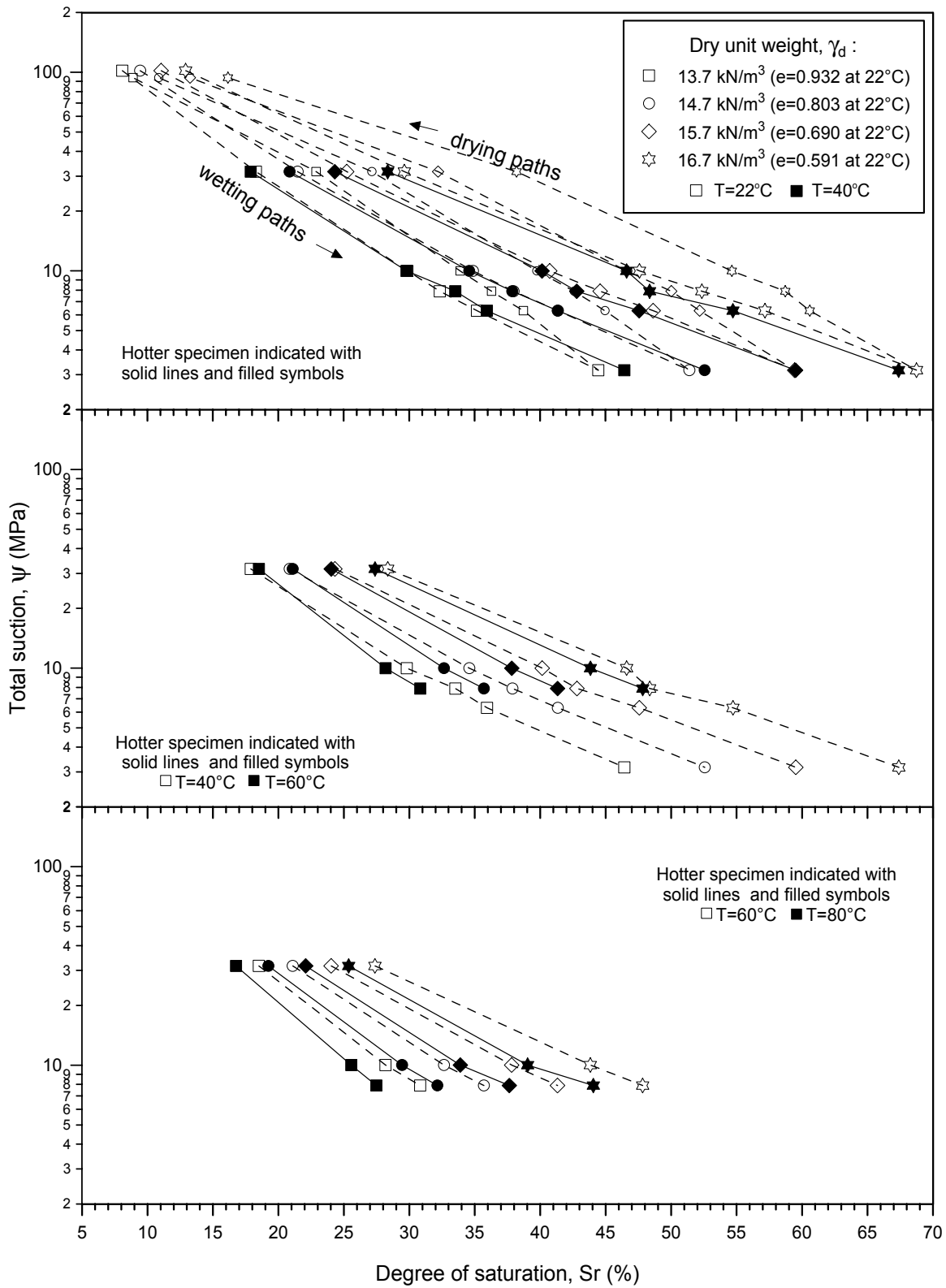
Figure 5.5   Dry unit weight-water content values after total suction equalisation.
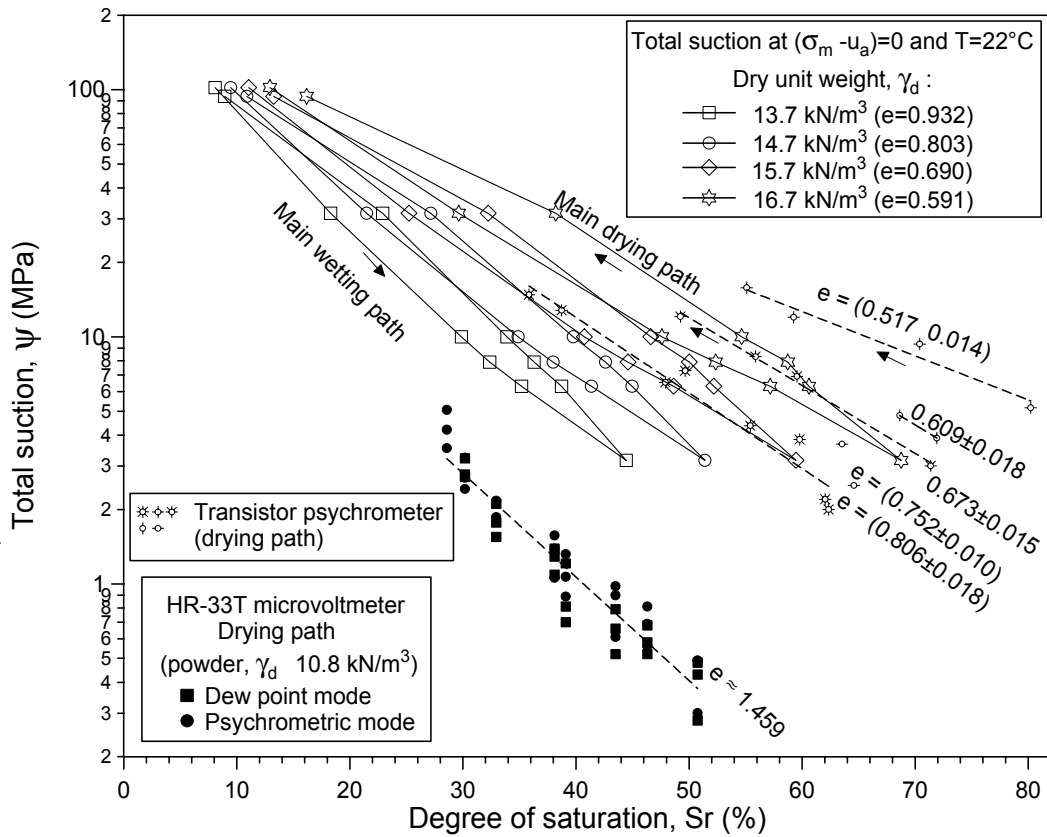
Figure 5.6   Total suction-degree of saturation relationships at constant porosity.
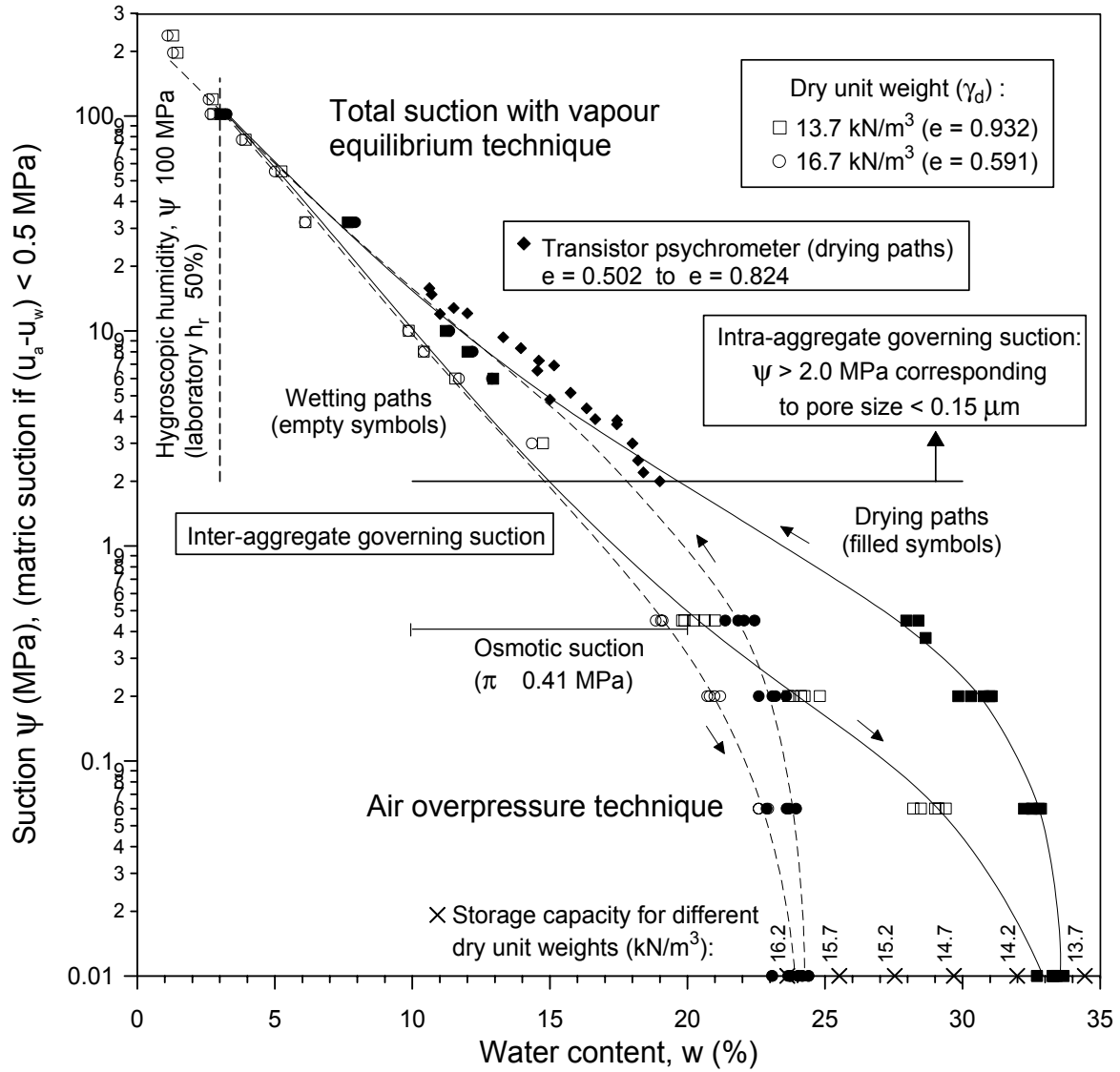
Figure 5.7   Relationships between suction and water content for different dry unit weights in main wetting and drying paths at 22°C (vapour equilibrium and air overpressure techniques).
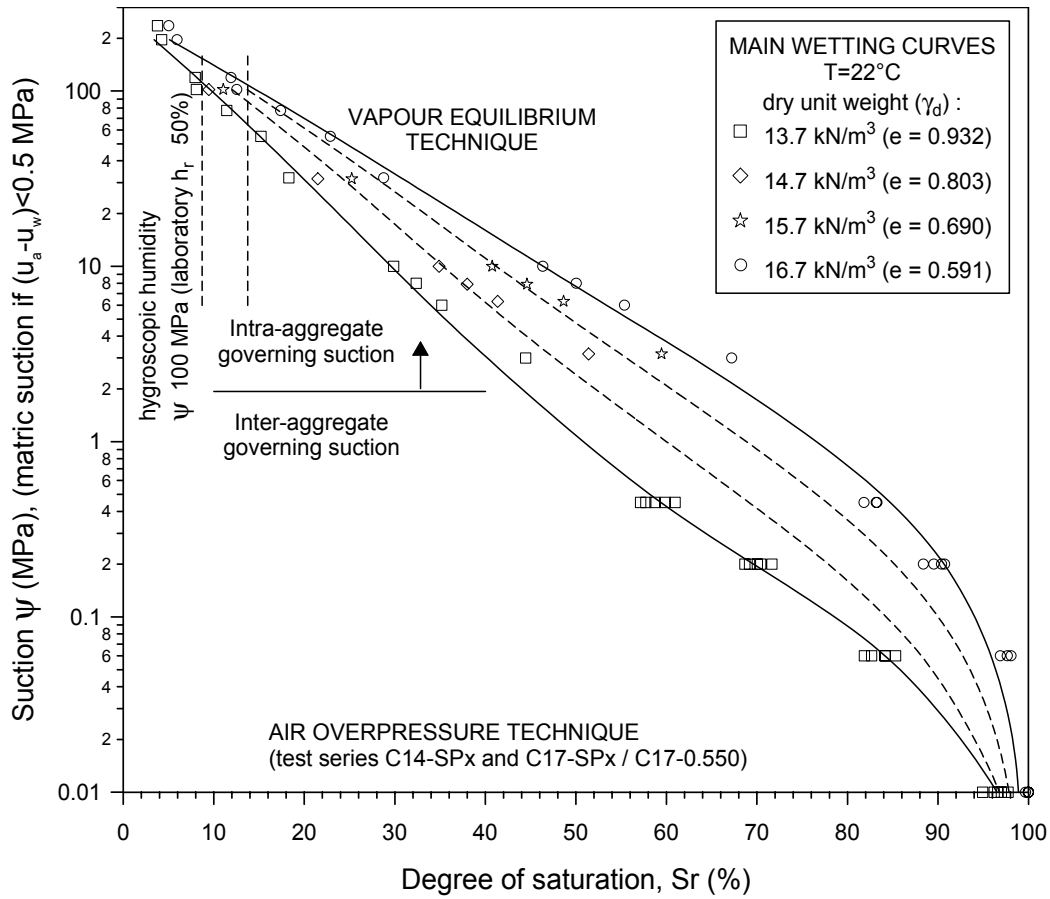
Figure 5.8 Relationships between suction and degree of saturation for different dry unit weights.
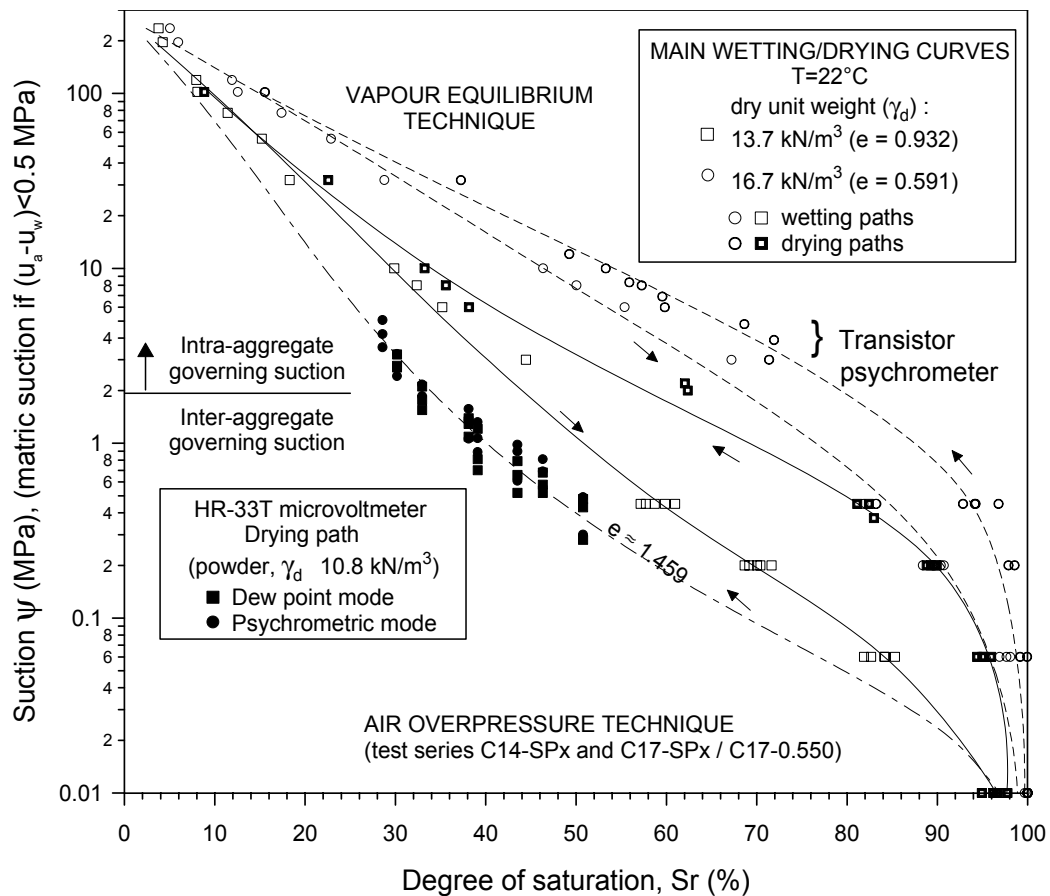
Figure 5.9 Main wetting and drying retention curves (suction vs. degree of saturation).
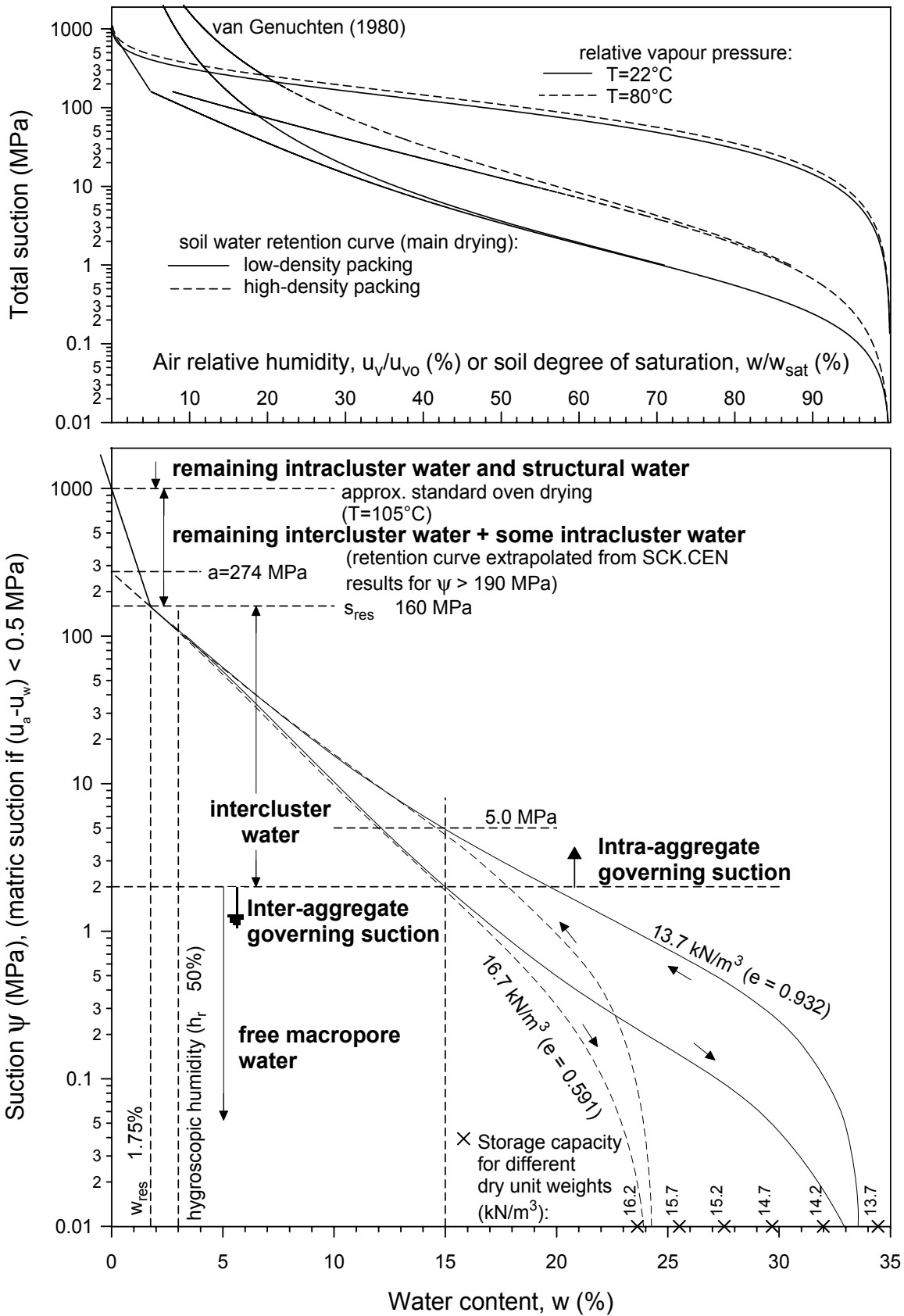
Figure 5.10 Conceptual framework of suction-water content retention curves at constant porosity.
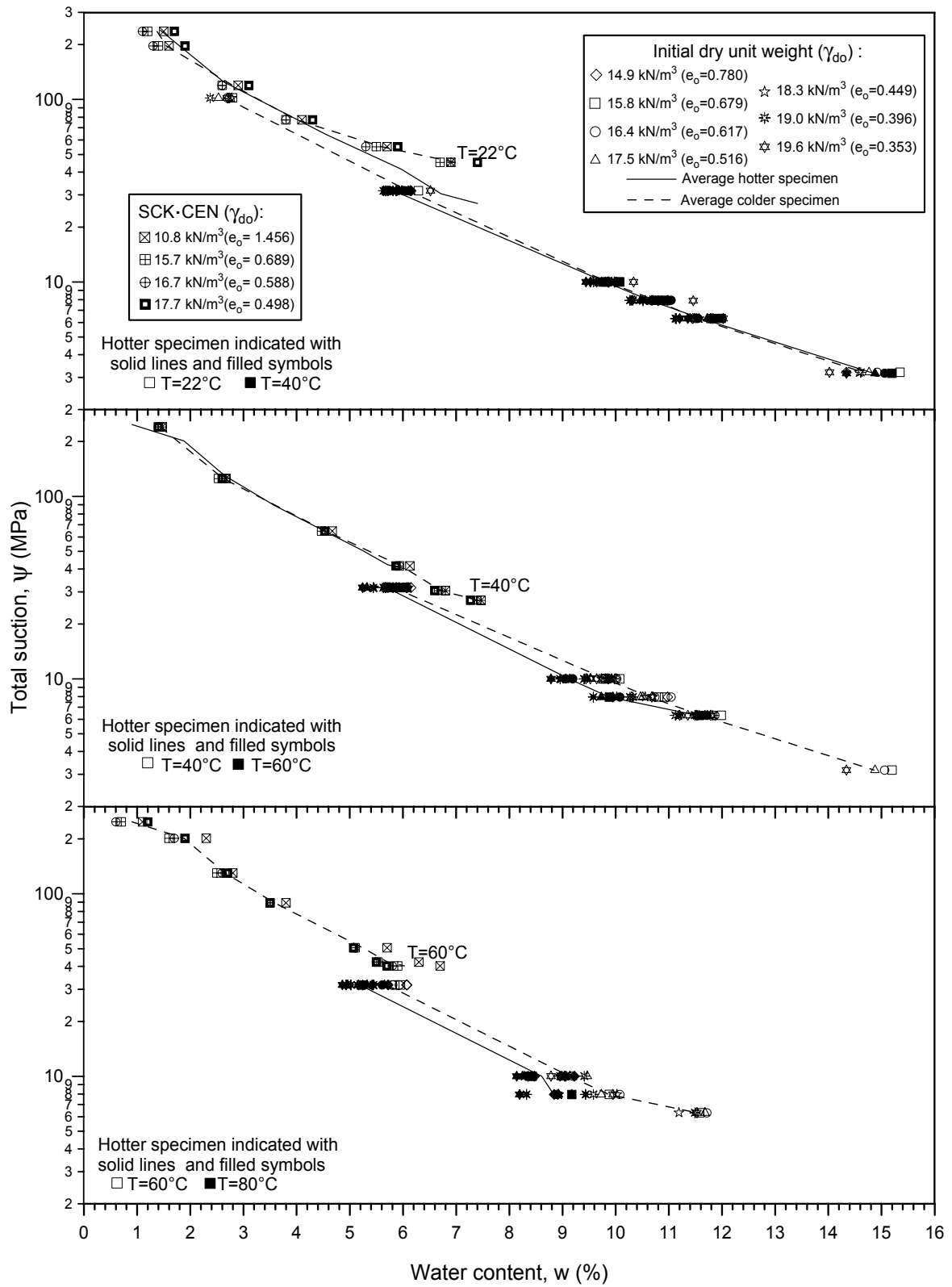
Figure 5.11   Soil water characteristic curves at different temperatures for different initial dry densities.
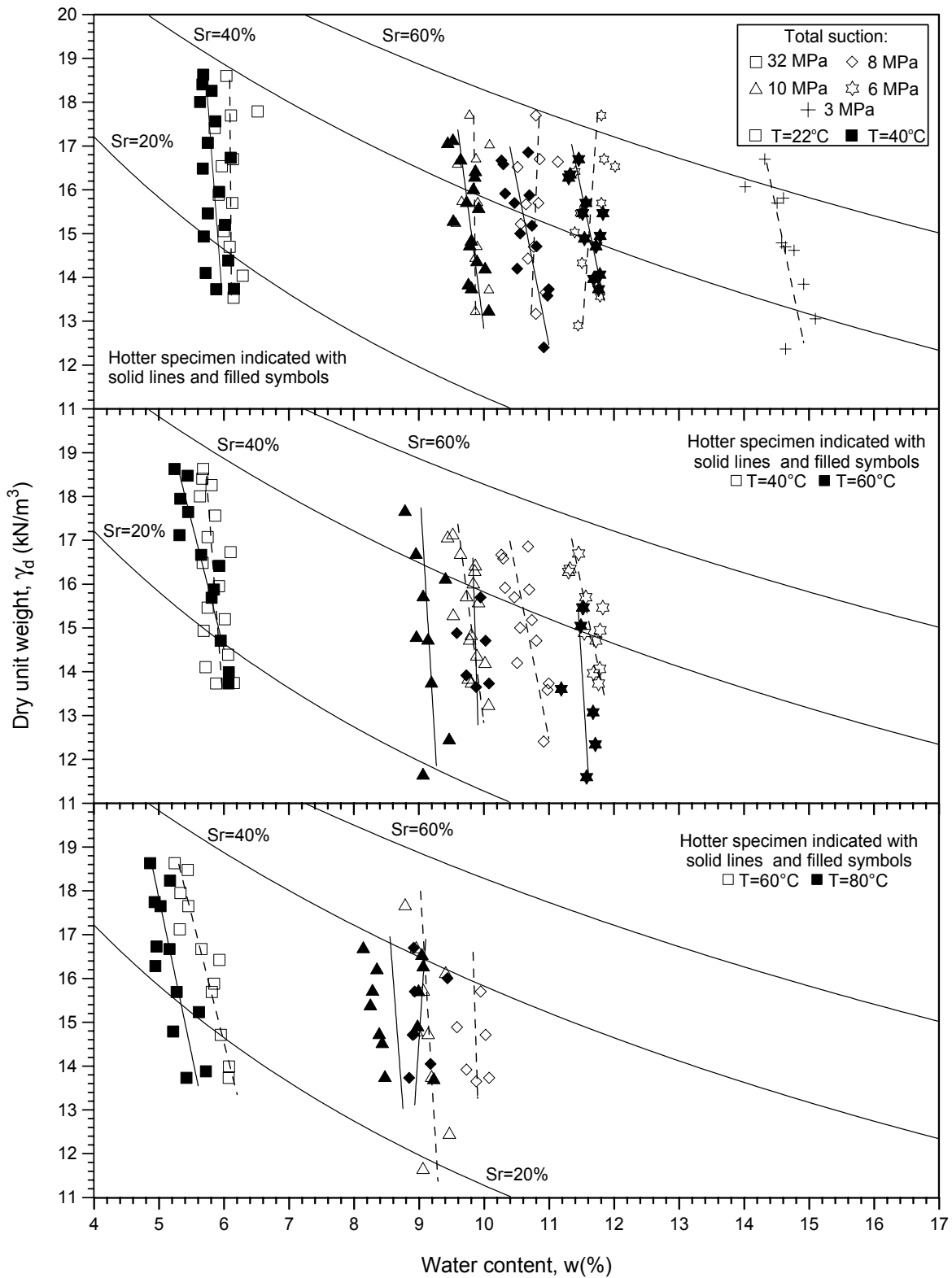
Figure 5.12   Dry unit weight-water content values after total suction equalisation in main wetting paths at different temperatures.

Figure 5.13 Dry unit weight-degree of saturation values after total suction equalisation in main wetting paths at different temperatures.

Figure 5.14   Total suction-degree of saturation relationships at constant porosity (main wetting paths at different temperatures).
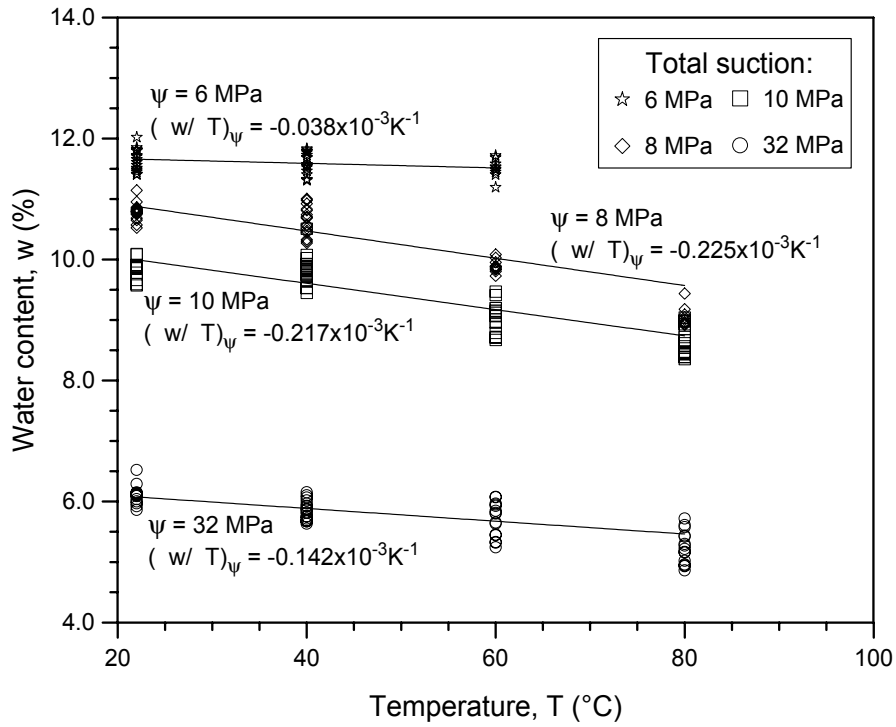
Figure 5.15   Water content-temperature plots at constant total suction.
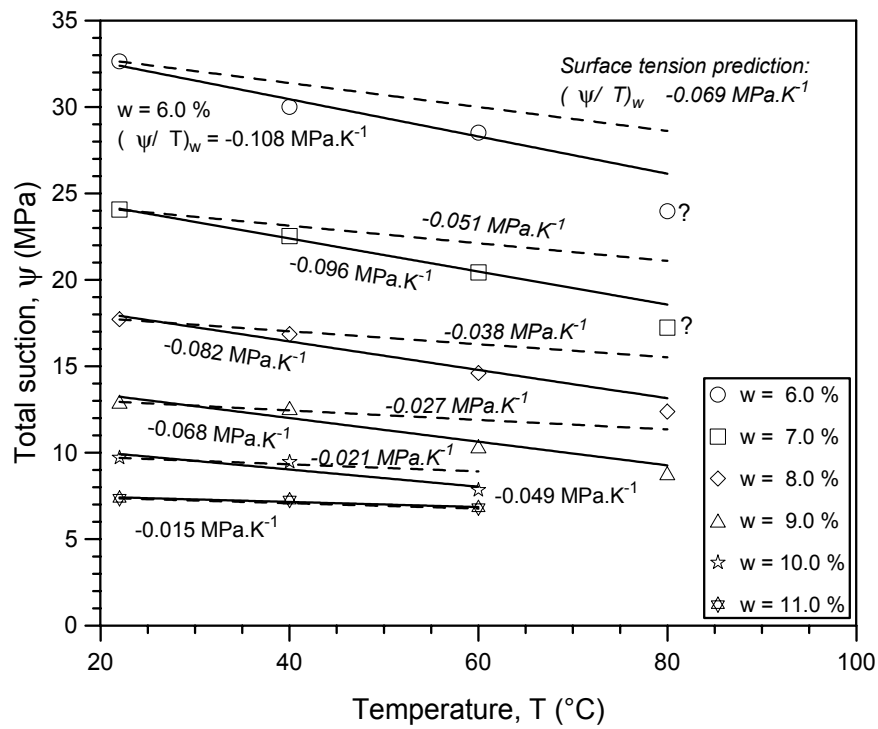
Figure 5.16   Total suction-temperature plots at constant water content.
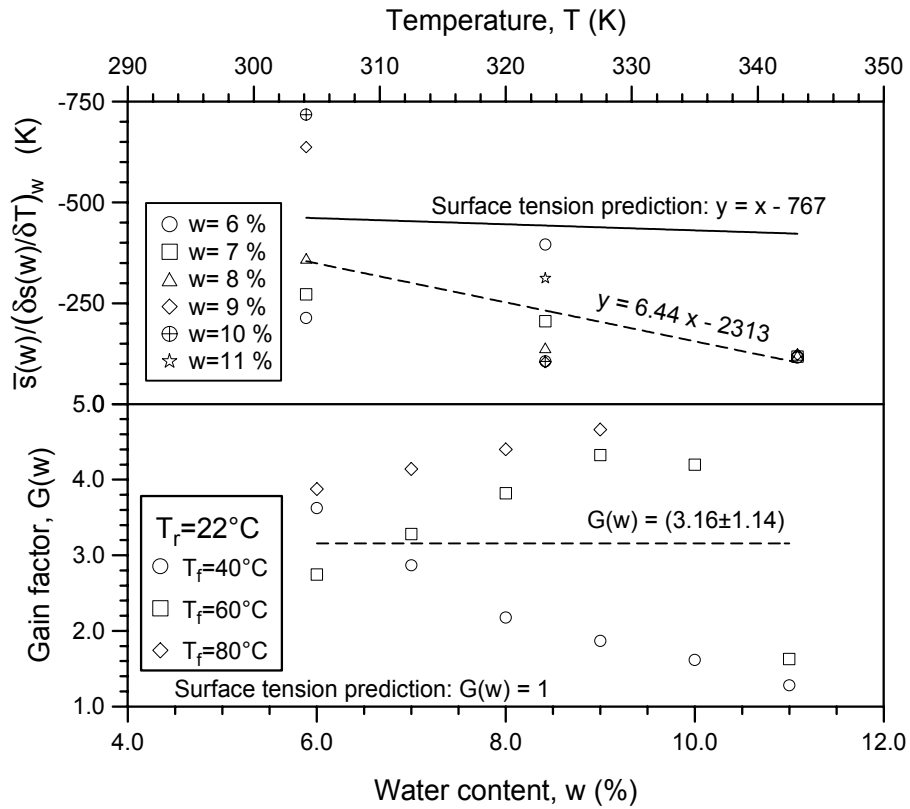
Figure 5.17   Parameters used to model temperature effects on energy status of soil water.
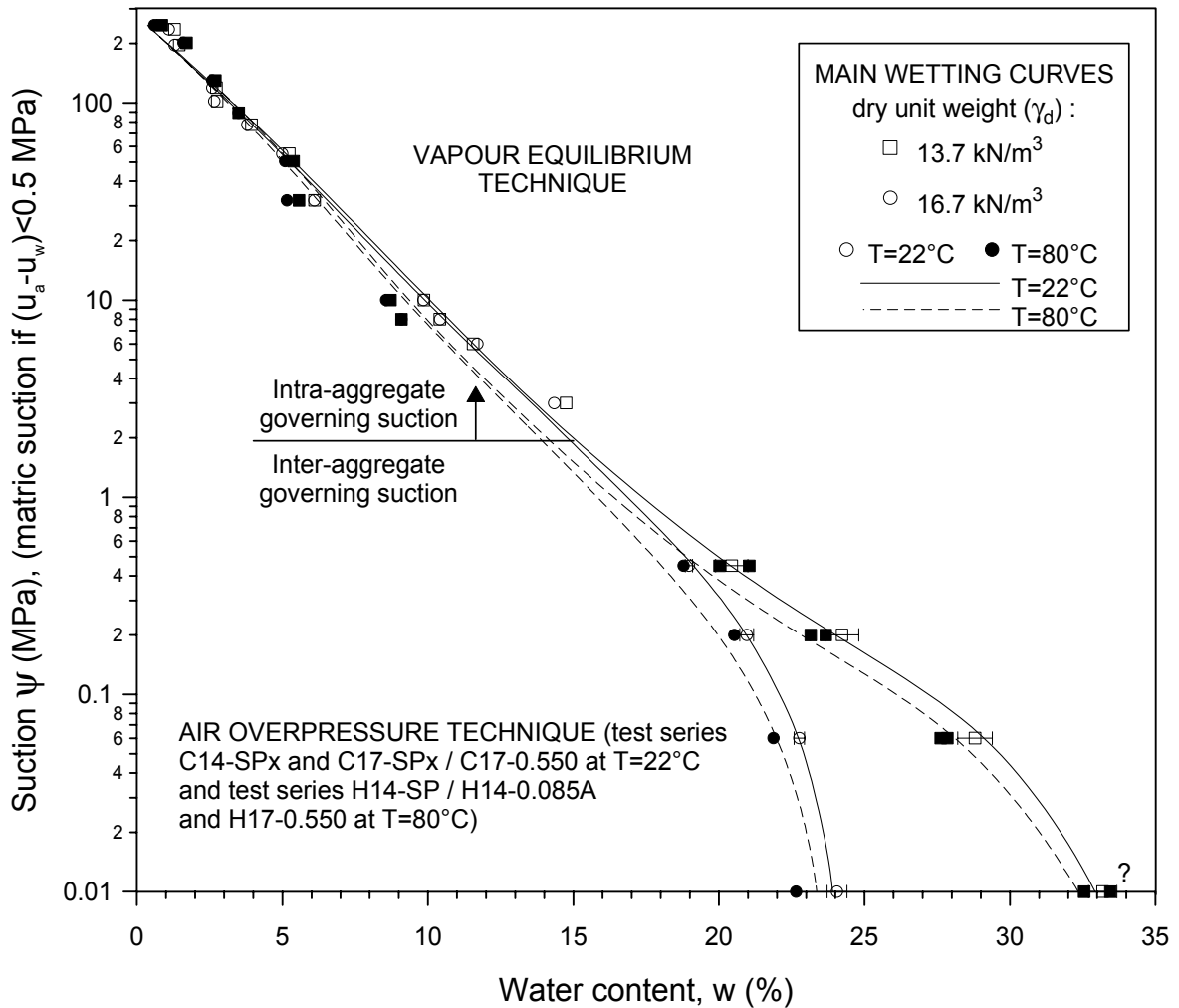
Figure 5.18   Relationships between suction and water content for different temperatures.
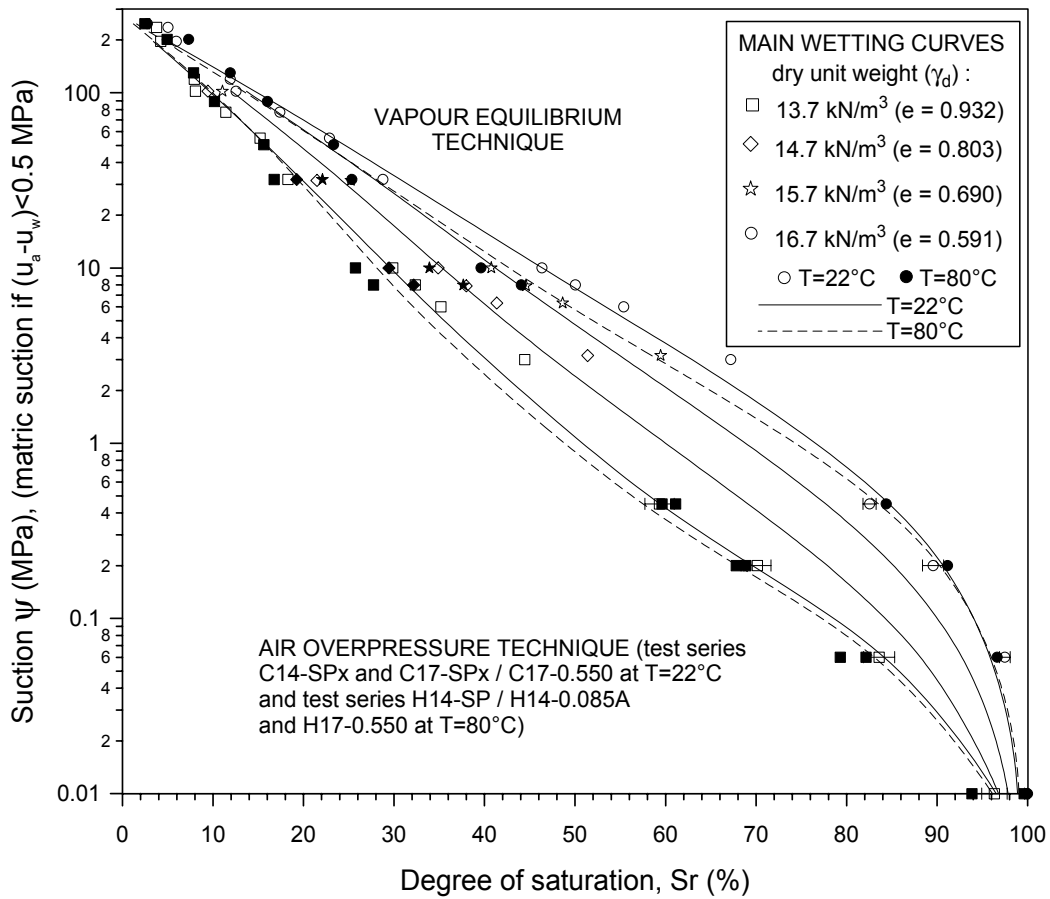
Figure 5.19   Relationships between suction and degree of saturation for different temperatures.
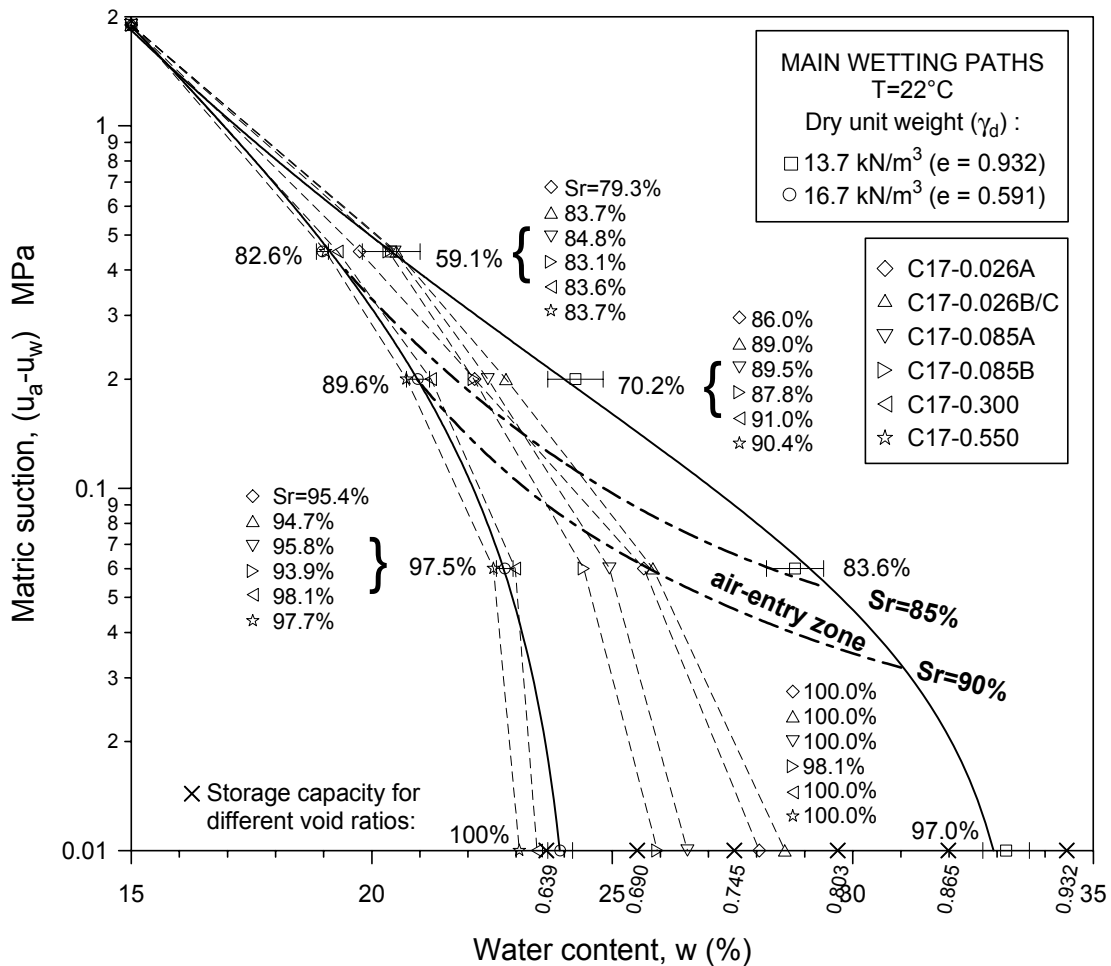
Figure 5.20   Main wetting retention curves for test series C17-xxx
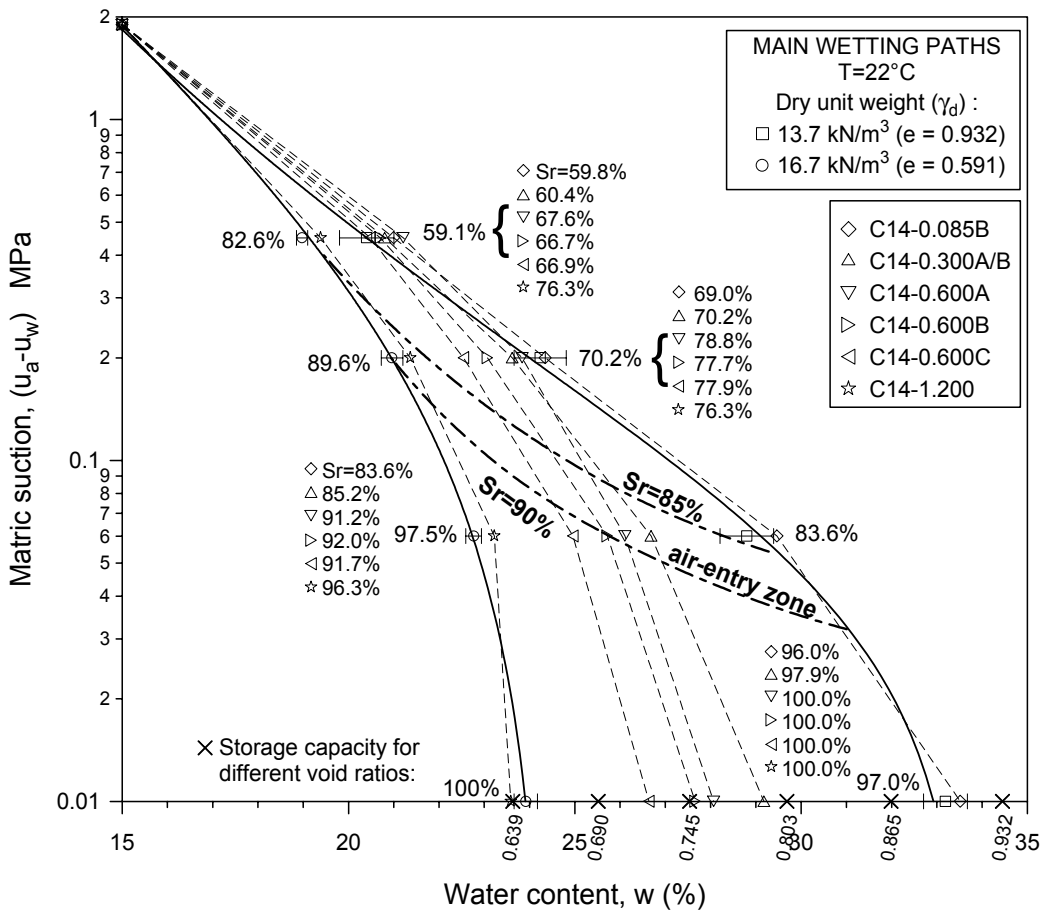
Figure 5.21 Main wetting retention curves for test series C14-xxx.
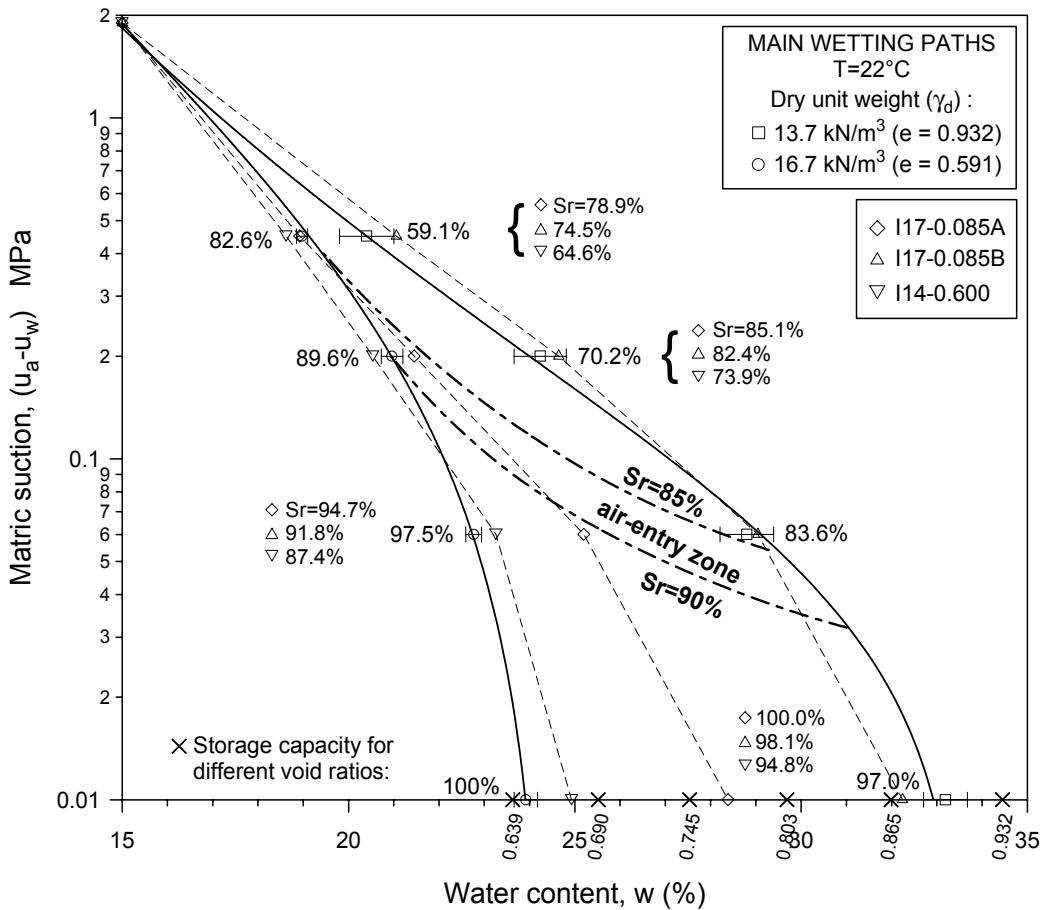
Figure 5.22 Main wetting retention curves for test series I17-xxx and I14-0.600.
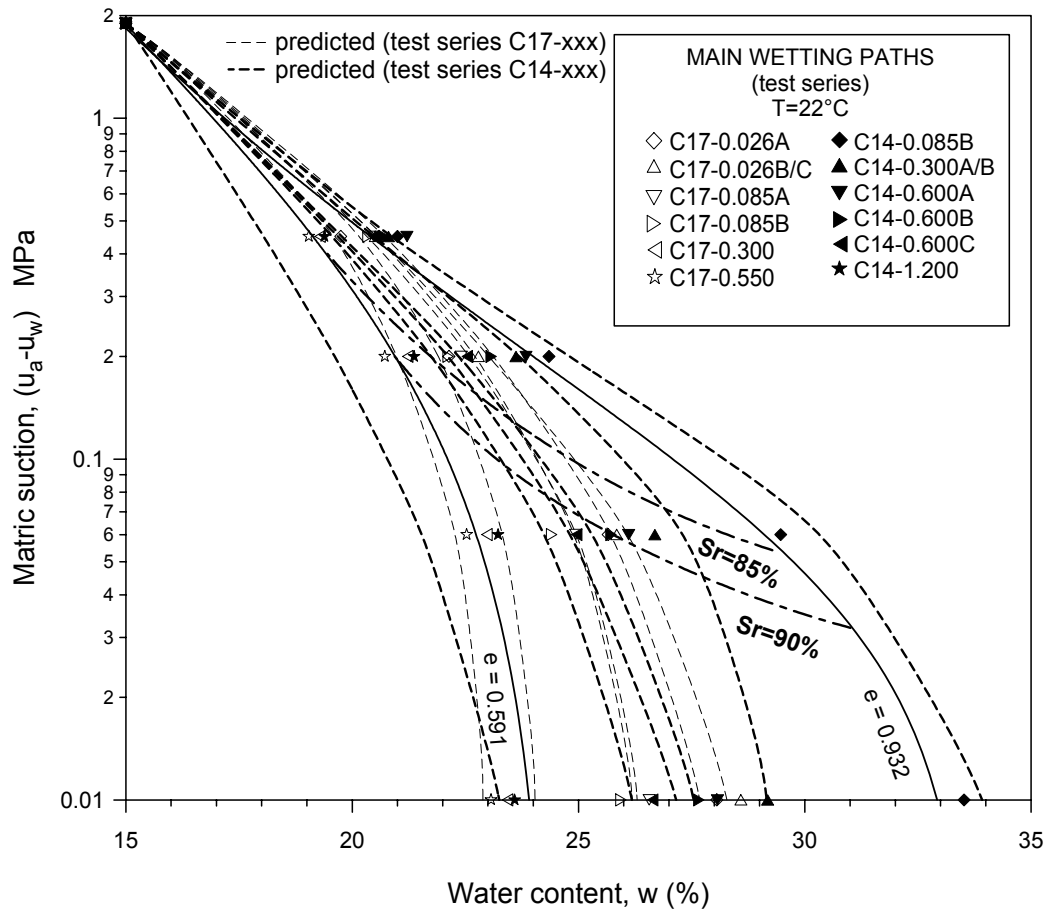
Figure 5.23   Predicted retention curves for main wetting paths (test series C17-xxx and C14-xxx).
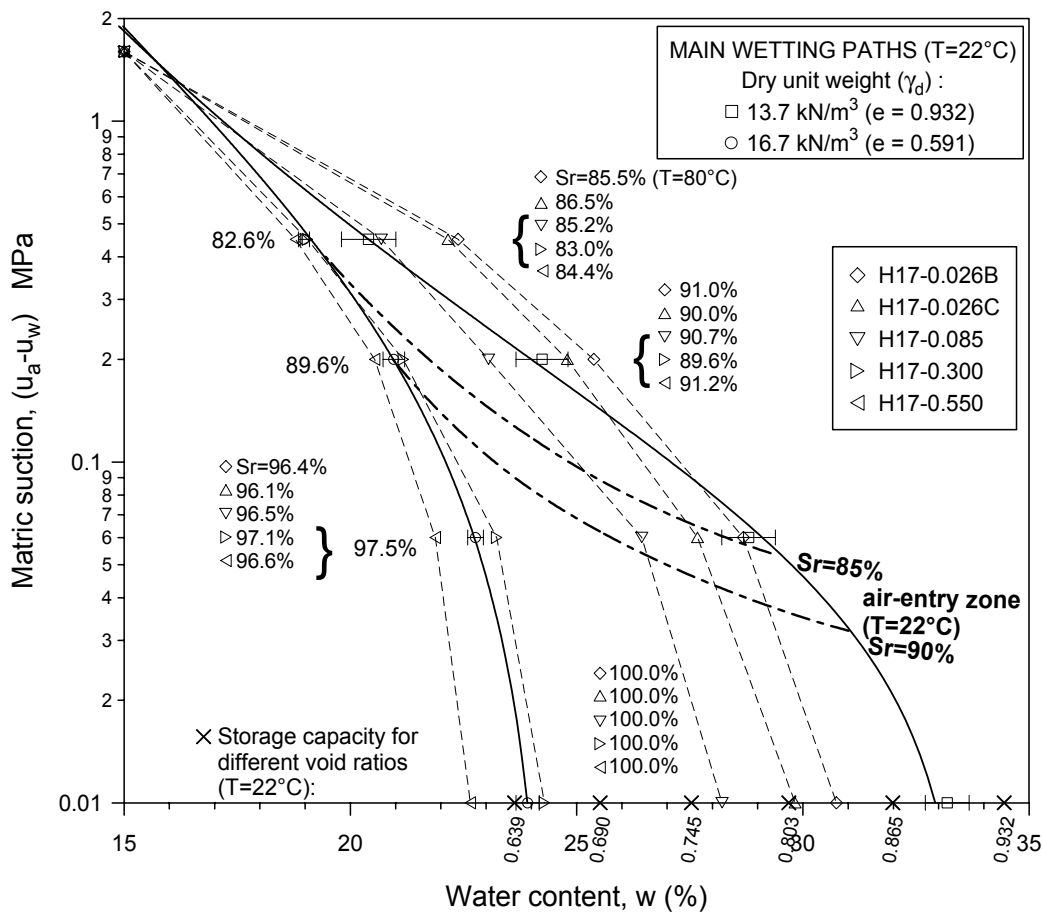
Figure 5.24   Main wetting retention curves for test series H17-xxx.
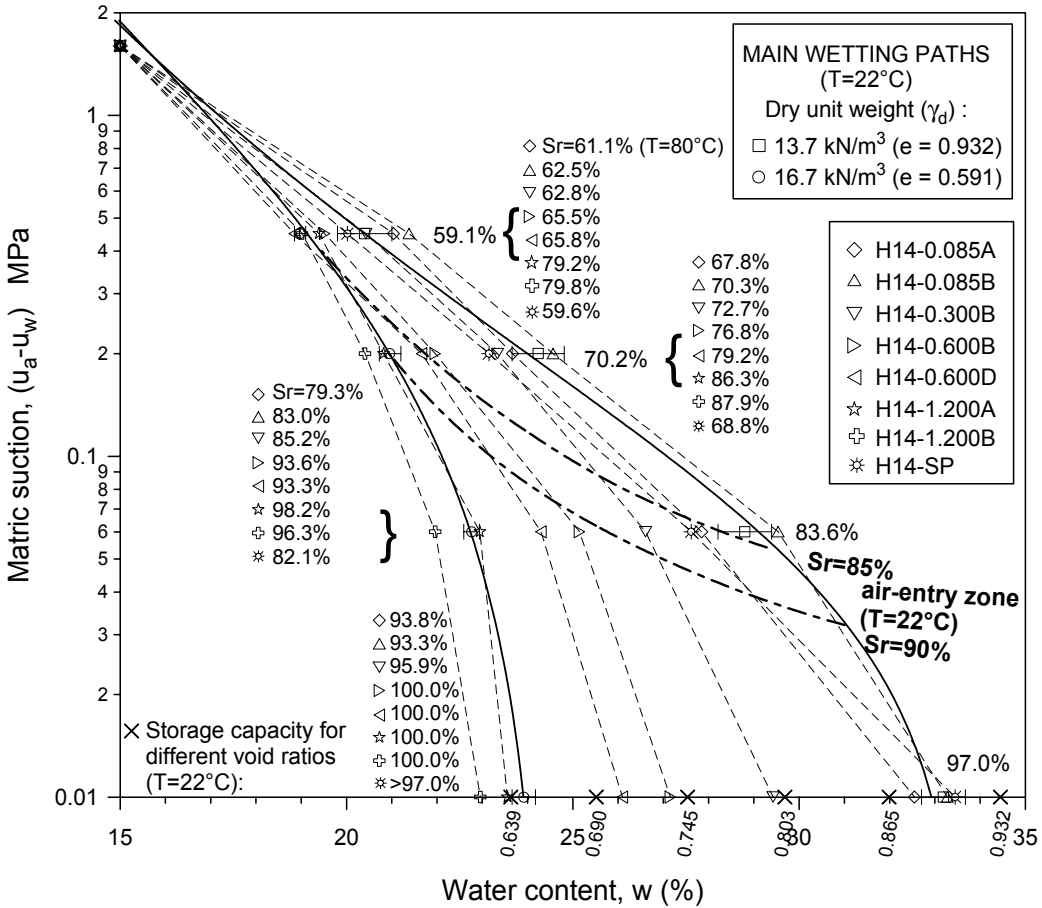
Figure 5.25   Main wetting retention curves for test series H14-xxx.
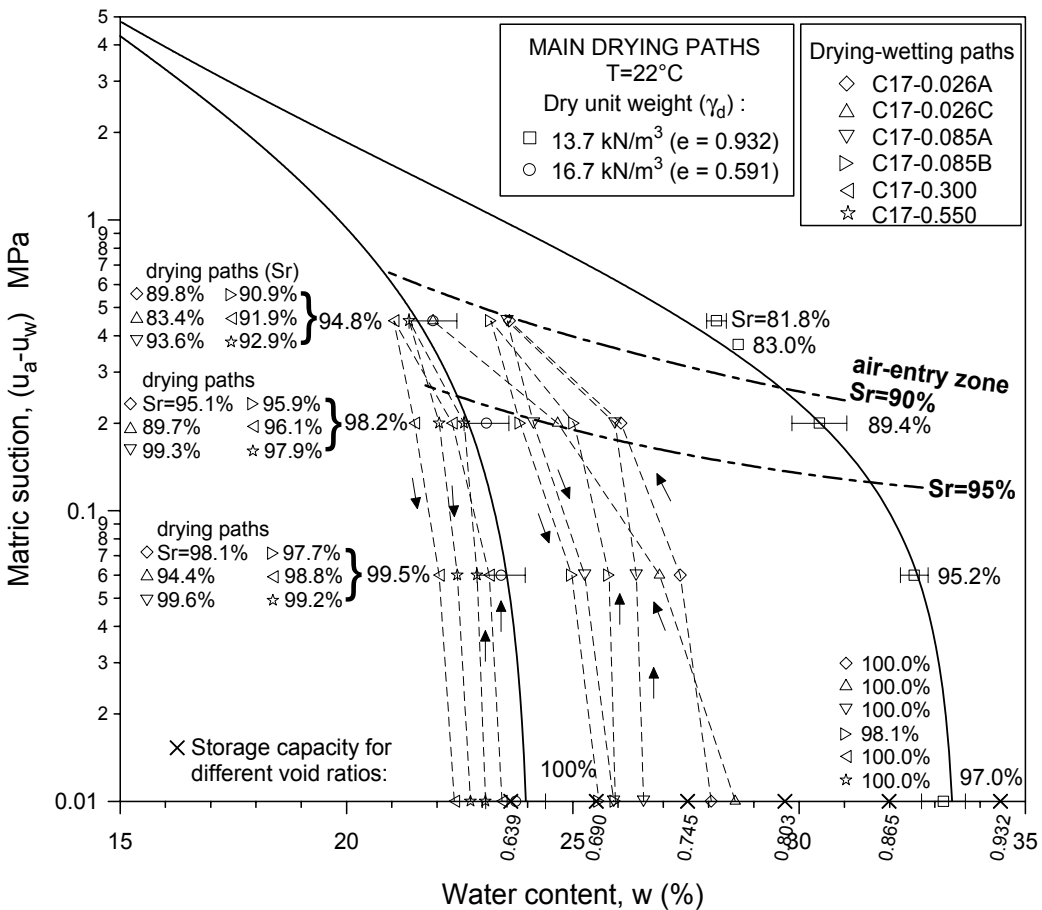
Figure 5.26   Main drying and scanning wetting retention curves for test series C17-xxx.
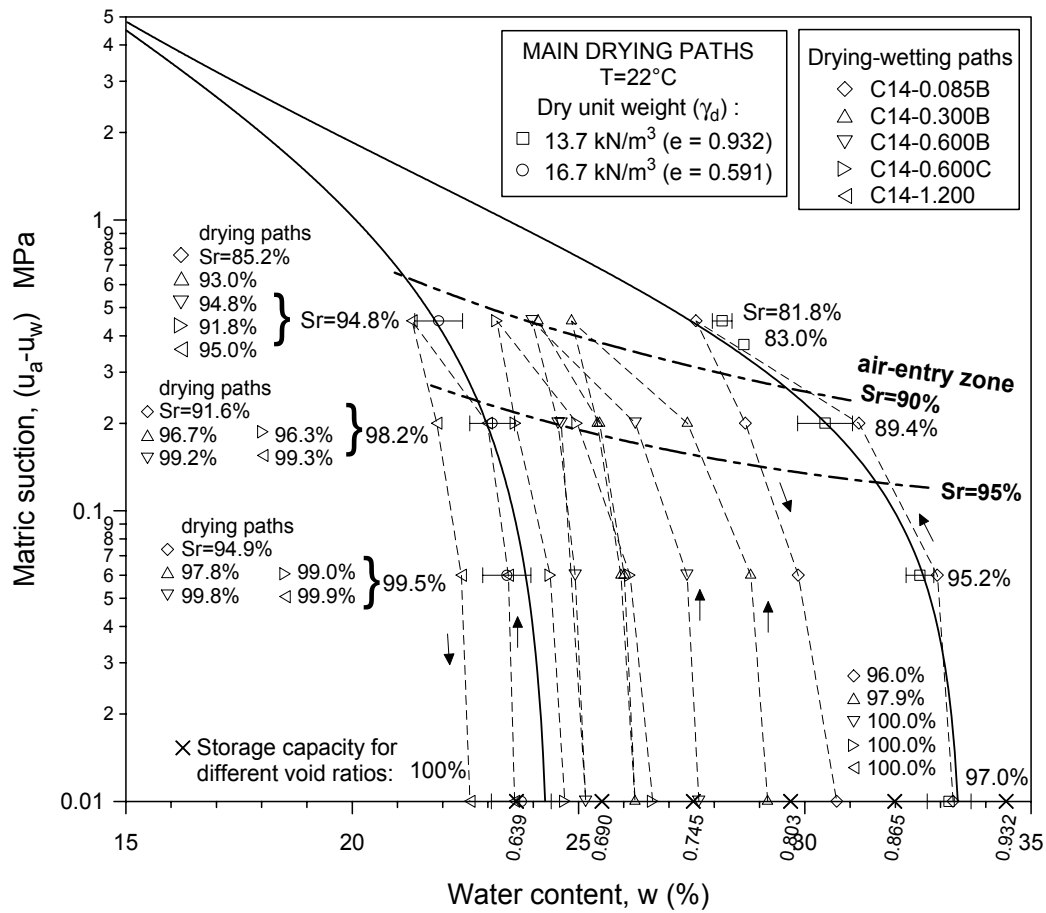
Figure 5.27   Main drying and scanning wetting retention curves for test series C14-xxx.
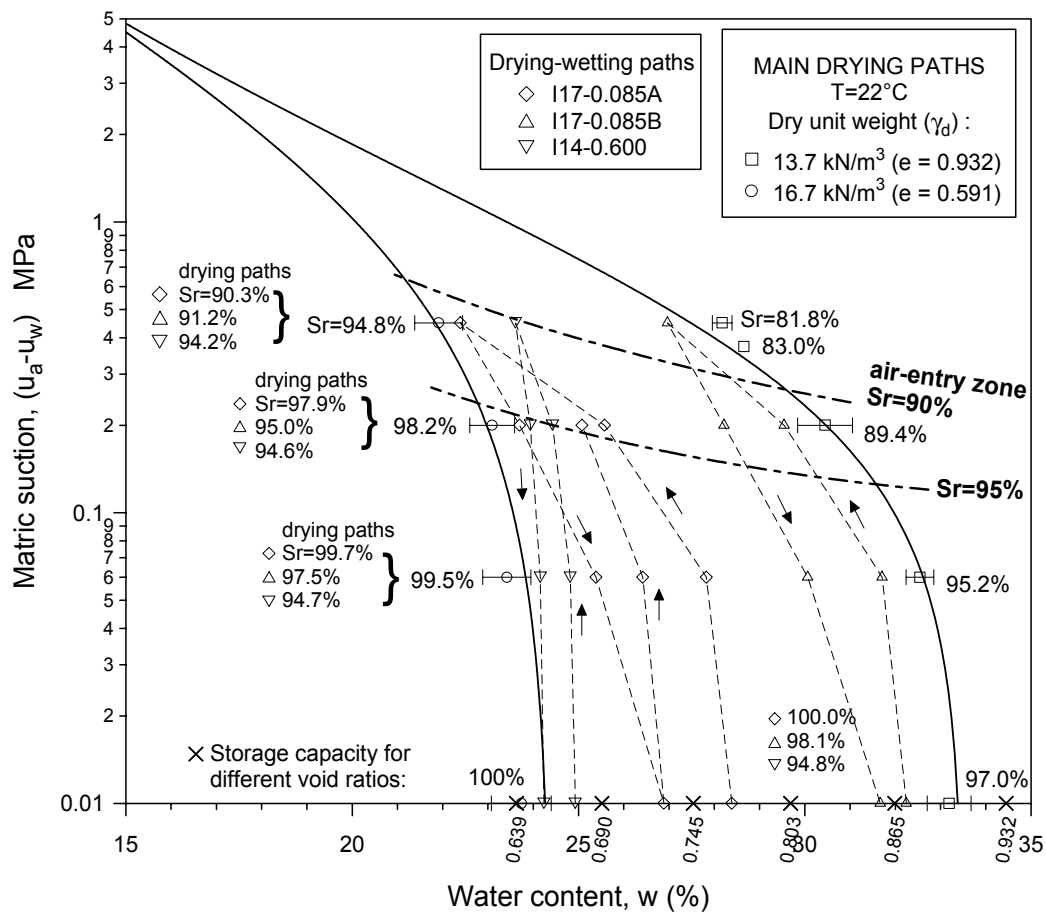
Figure 5.28   Main drying and scanning wetting retention curves for test series I17-xxx and I14-0.600.
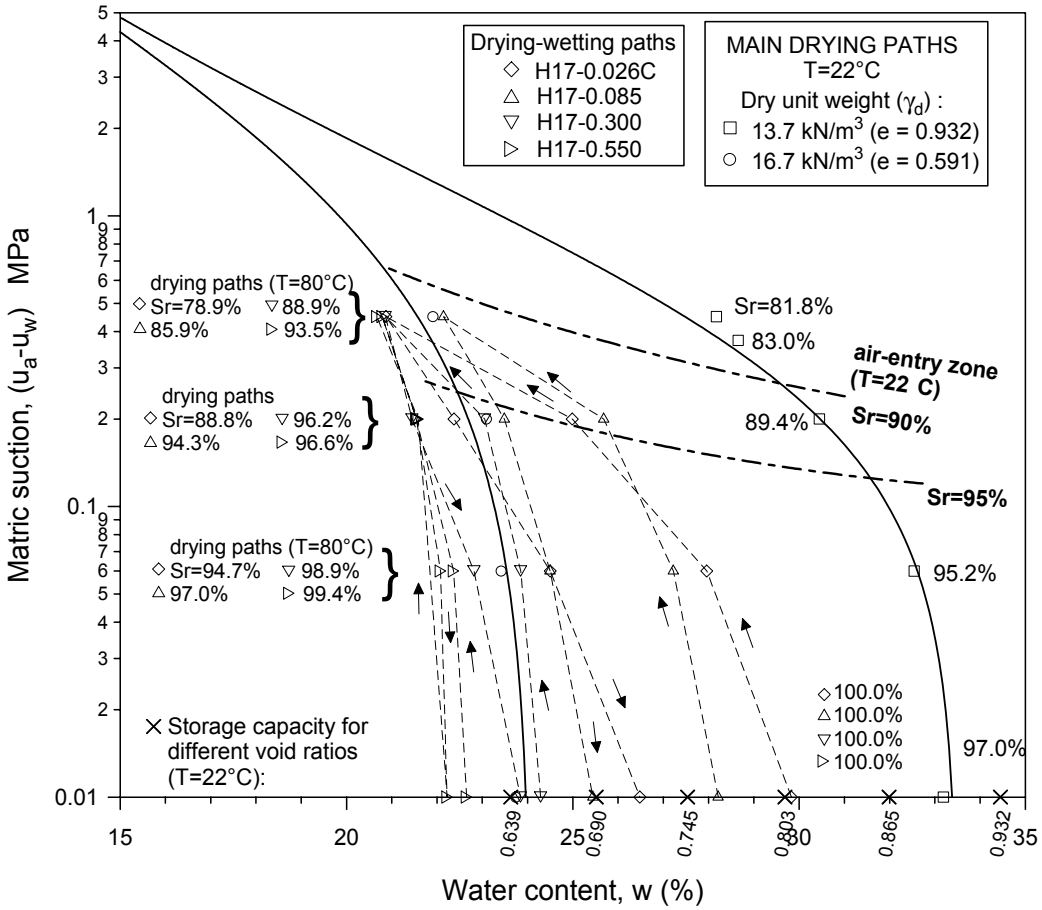
Figure 5.29   Main drying and scanning wetting retention curves for test series H17-xxx.
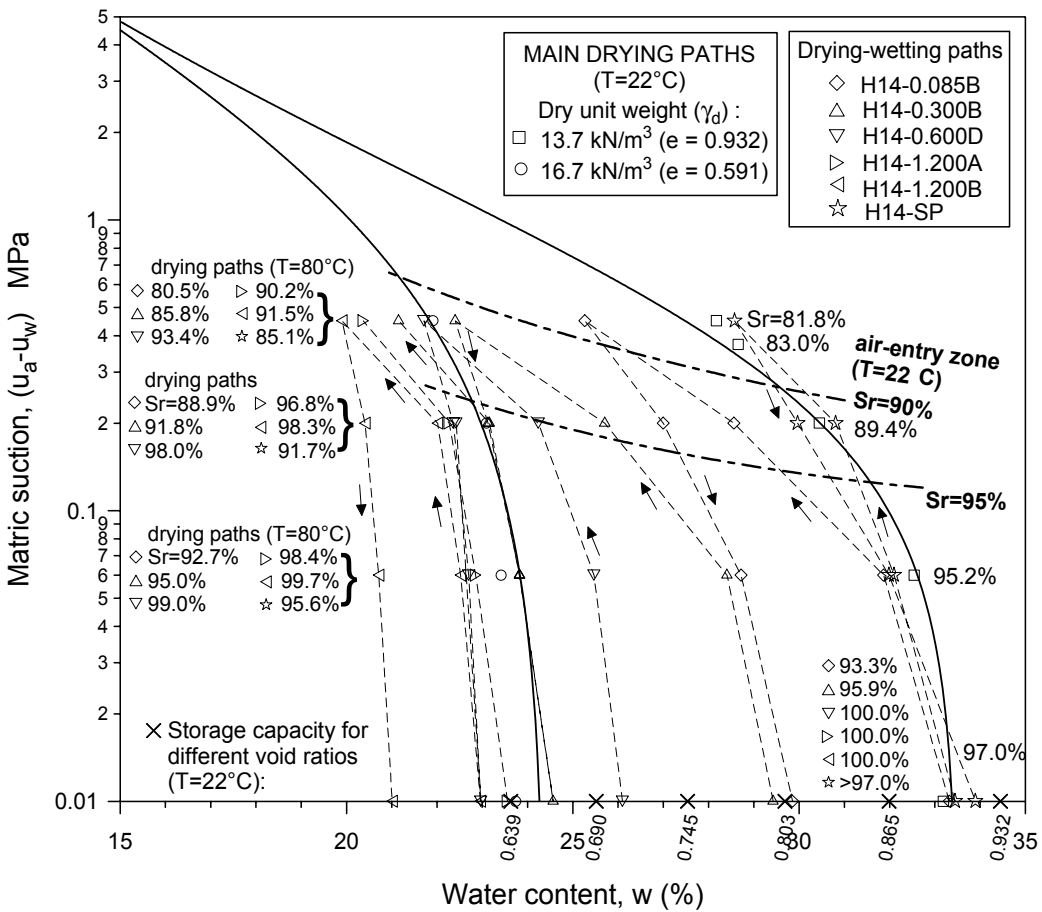
Figure 5.30   Main drying and scanning wetting retention curves for test series H14-xxx.
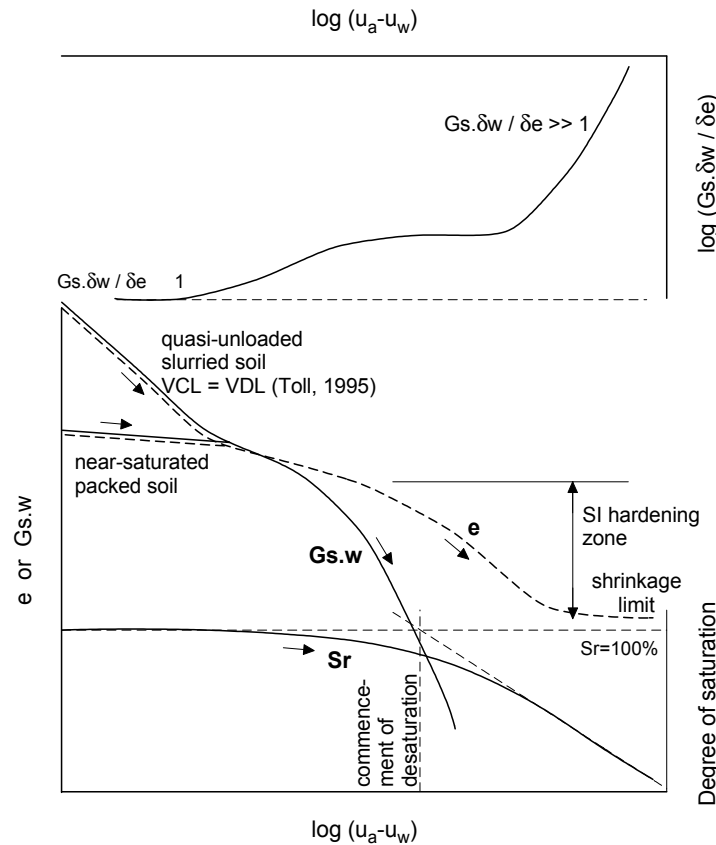
Figure 5.31   Conceptual framework for main drying paths departing from near-saturated conditions.
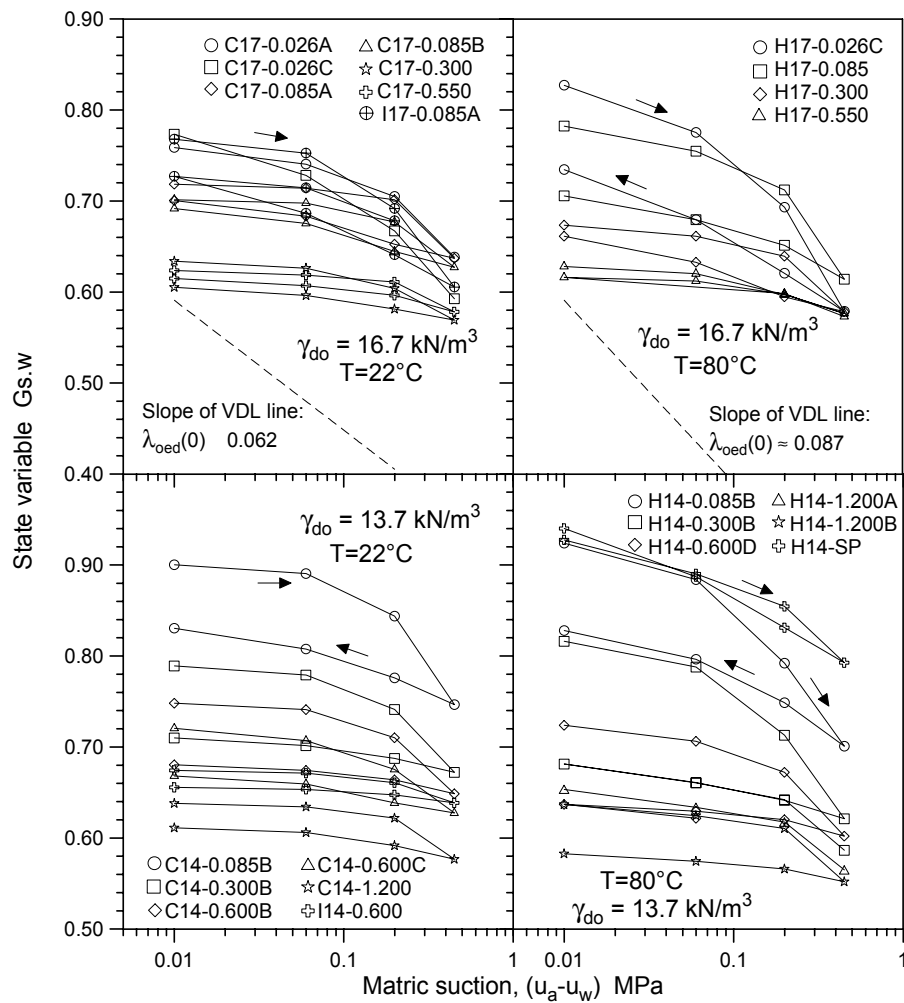
Figure 5.32   Main drying and scanning wetting paths for different packings and temperatures.
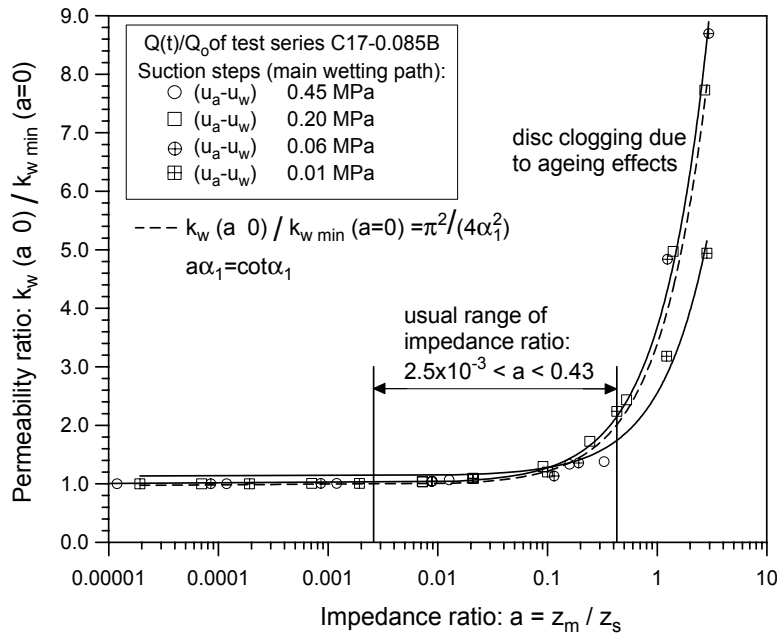
Figure 5.33 Impedance ratio effects on water permeability (transient inflow/outflow method).
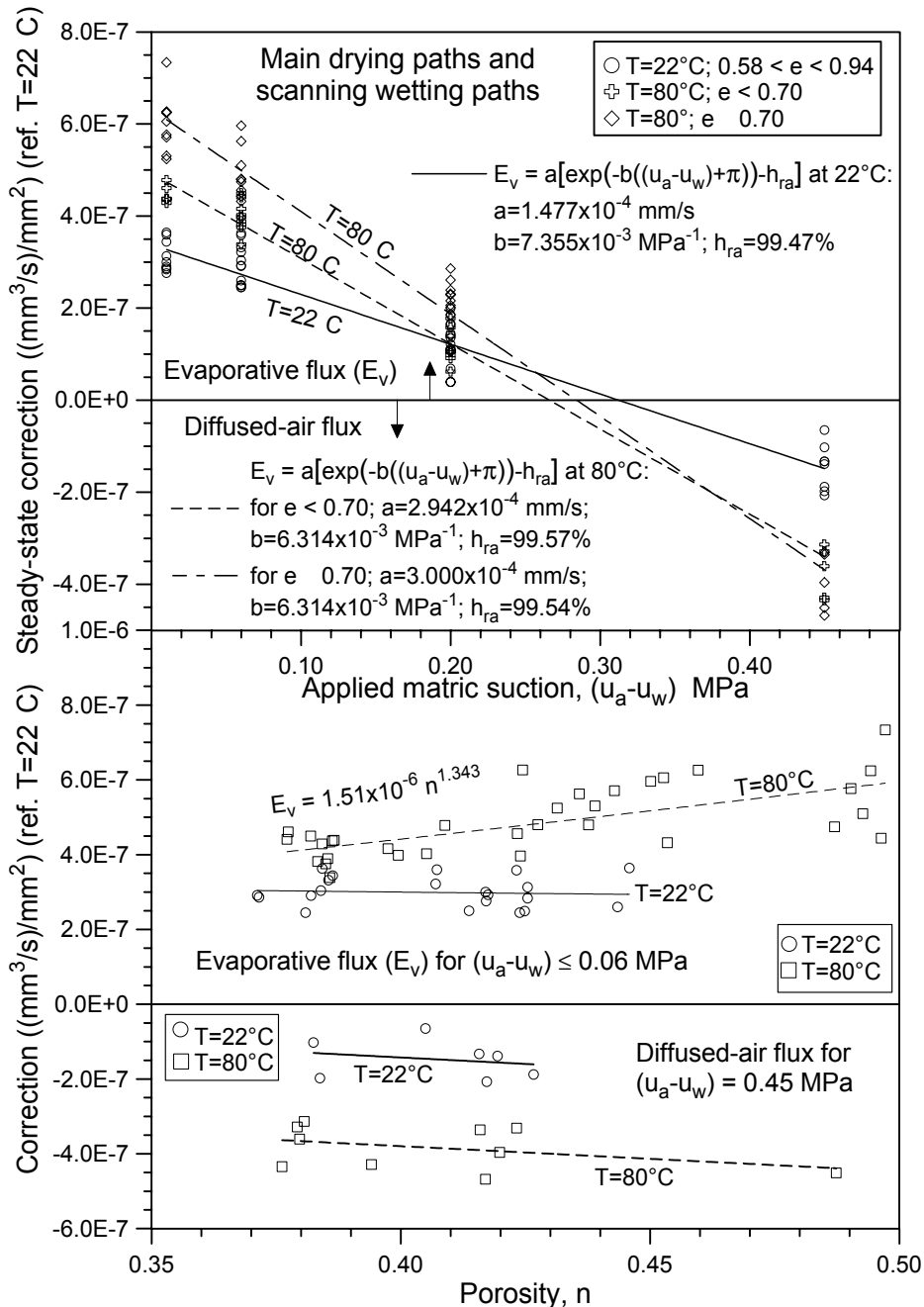
Figure 5.34 Steady-state corrections for air diffusion and soil water evaporation.
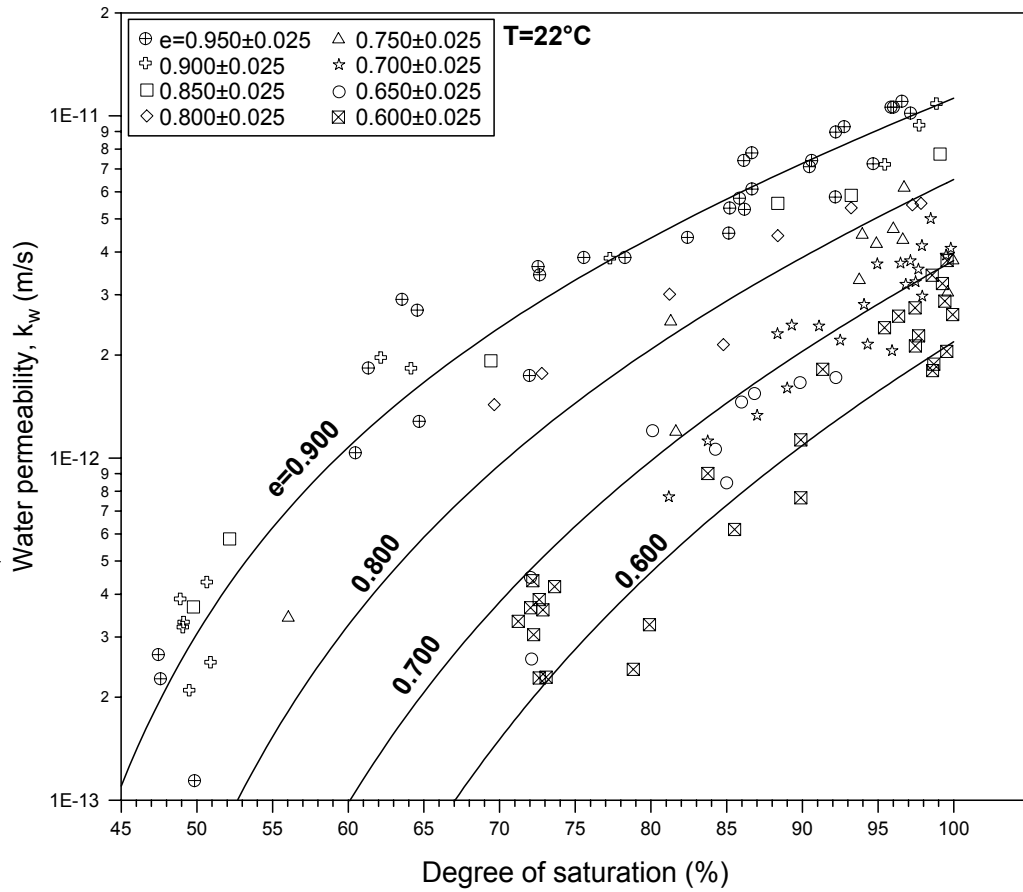
Figure 5.35   Water permeability vs. degree of saturation obtained in different suction steps at 22°C.
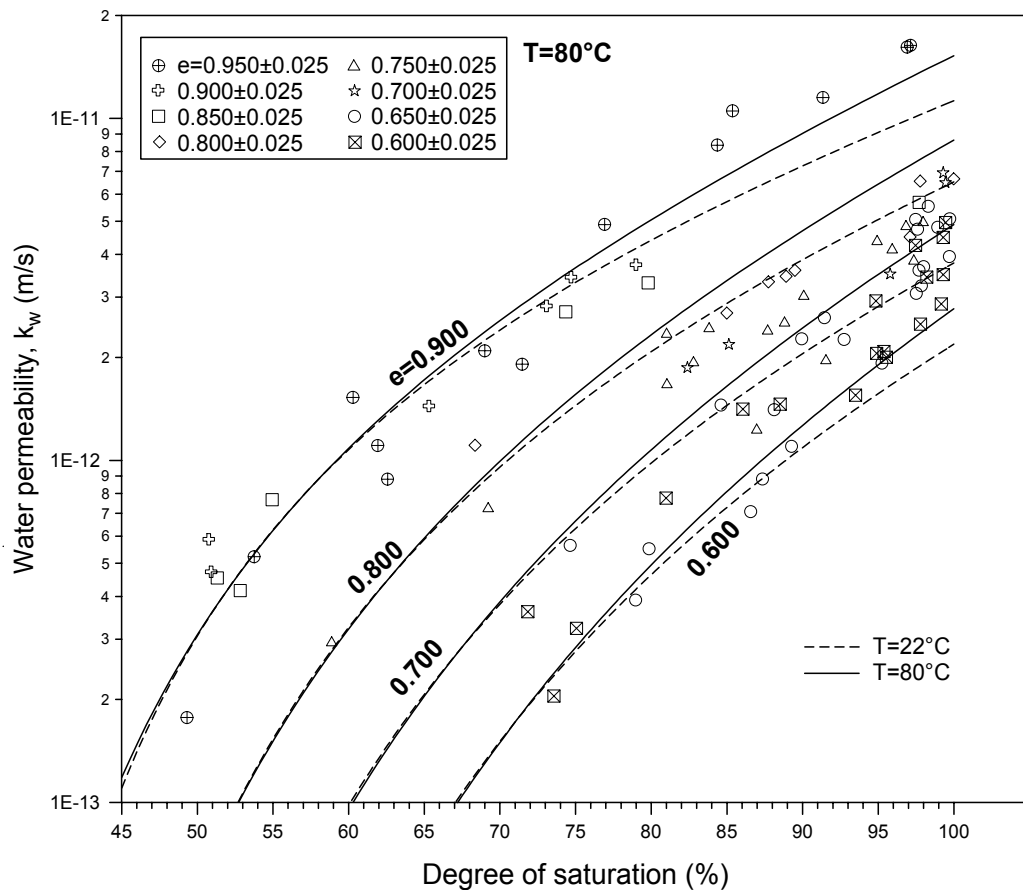
Figure 5.36   Water permeability vs. degree of saturation obtained in different suction steps at 80°C.
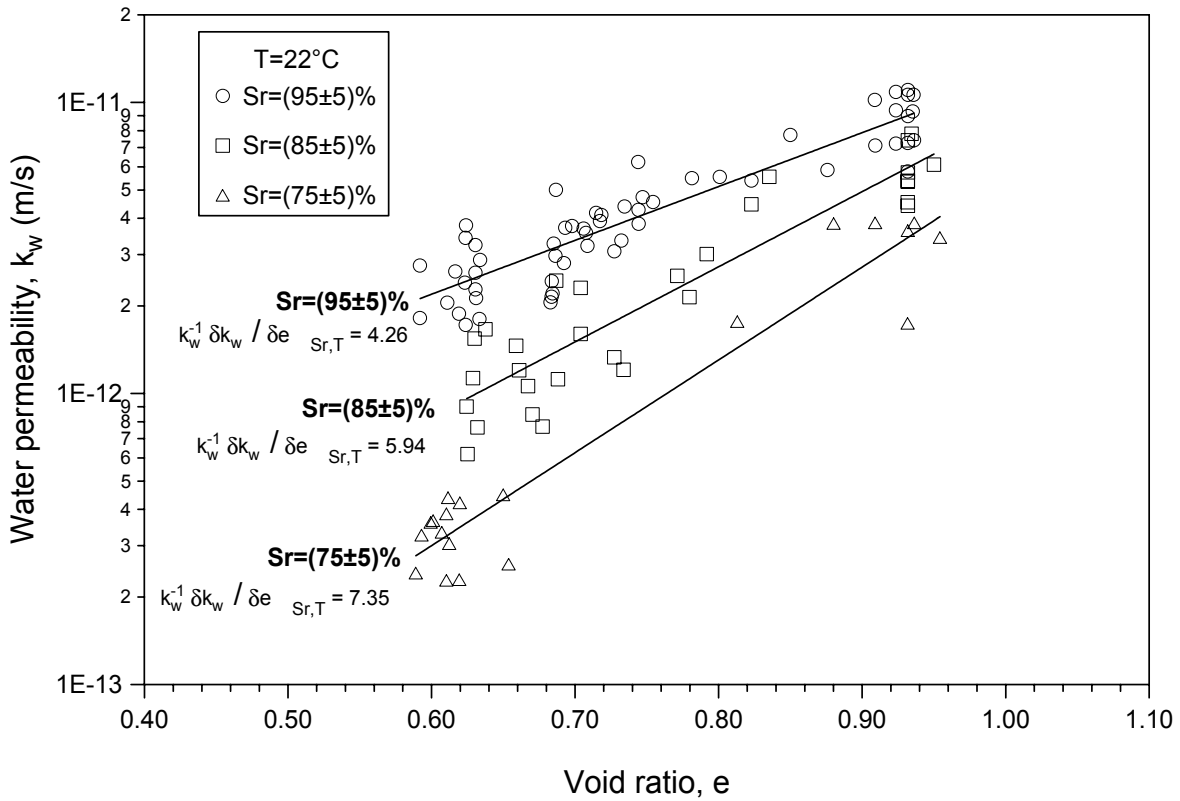
Figure 5.37   Water permeability vs. void ratio for constant degrees of saturation at 22°C.
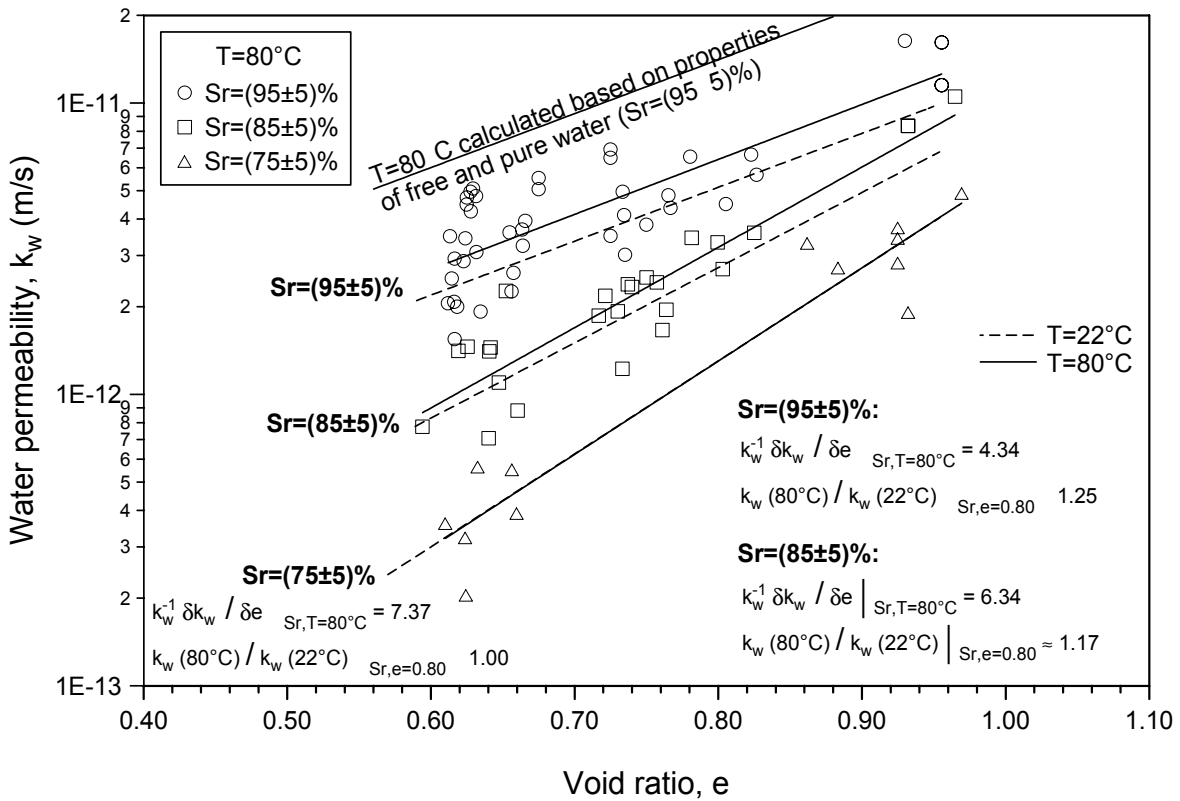
Figure 5.38   Water permeability vs. void ratio for constant degrees of saturation at 80°C.
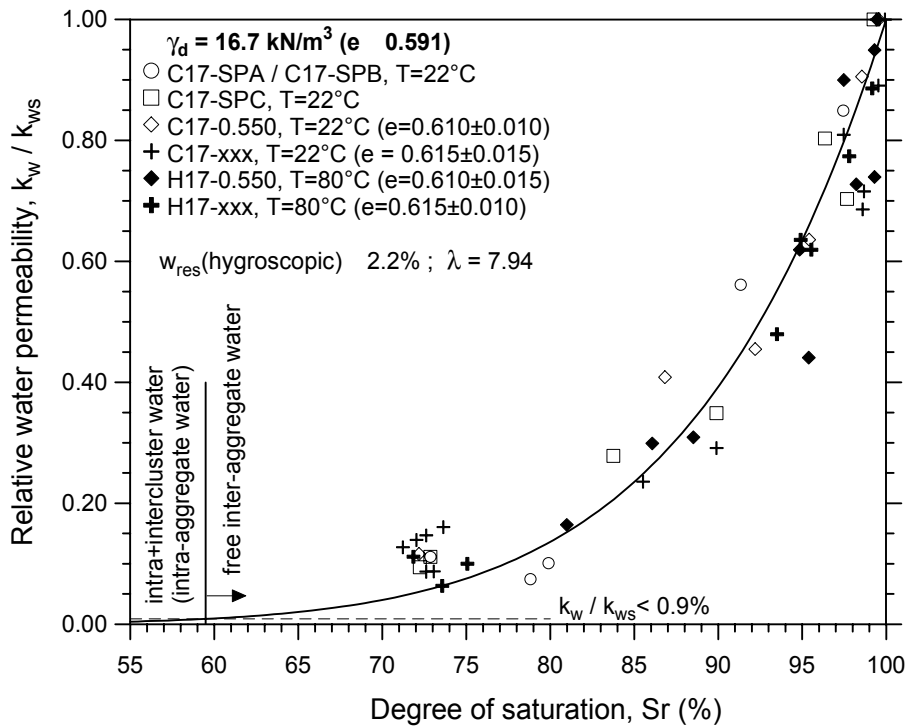
Figure 5.39 Relative water permeability-degree of saturation relationship for a constant low-porosity packing at a reference $w_{res} = 2.2\%$.
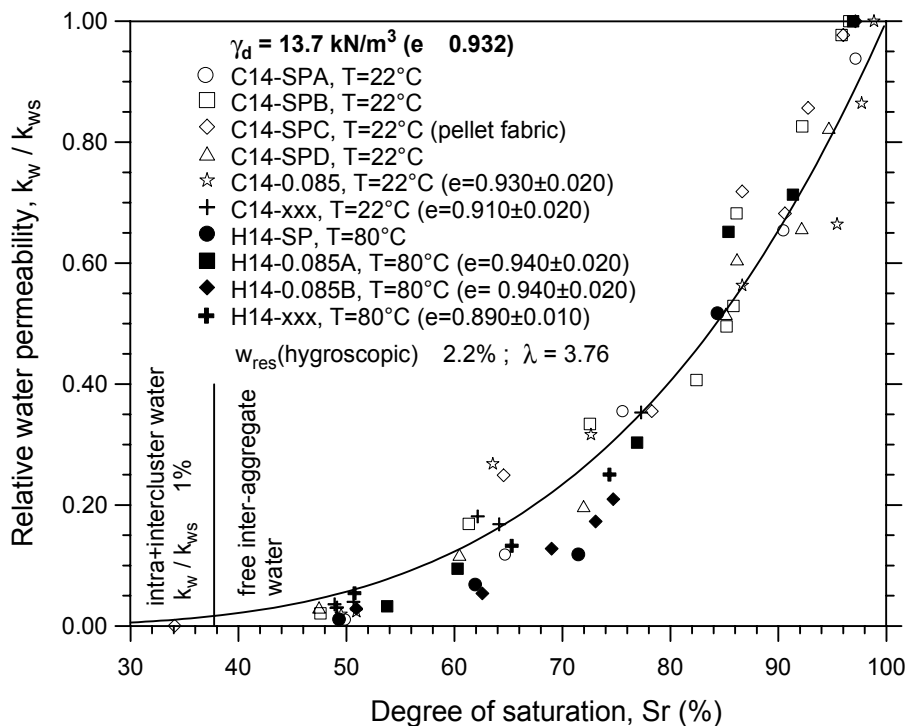
Figure 5.40 Relative water permeability-degree of saturation relationship for a constant high-porosity packing at a reference $w_{res} = 2.2\%$.
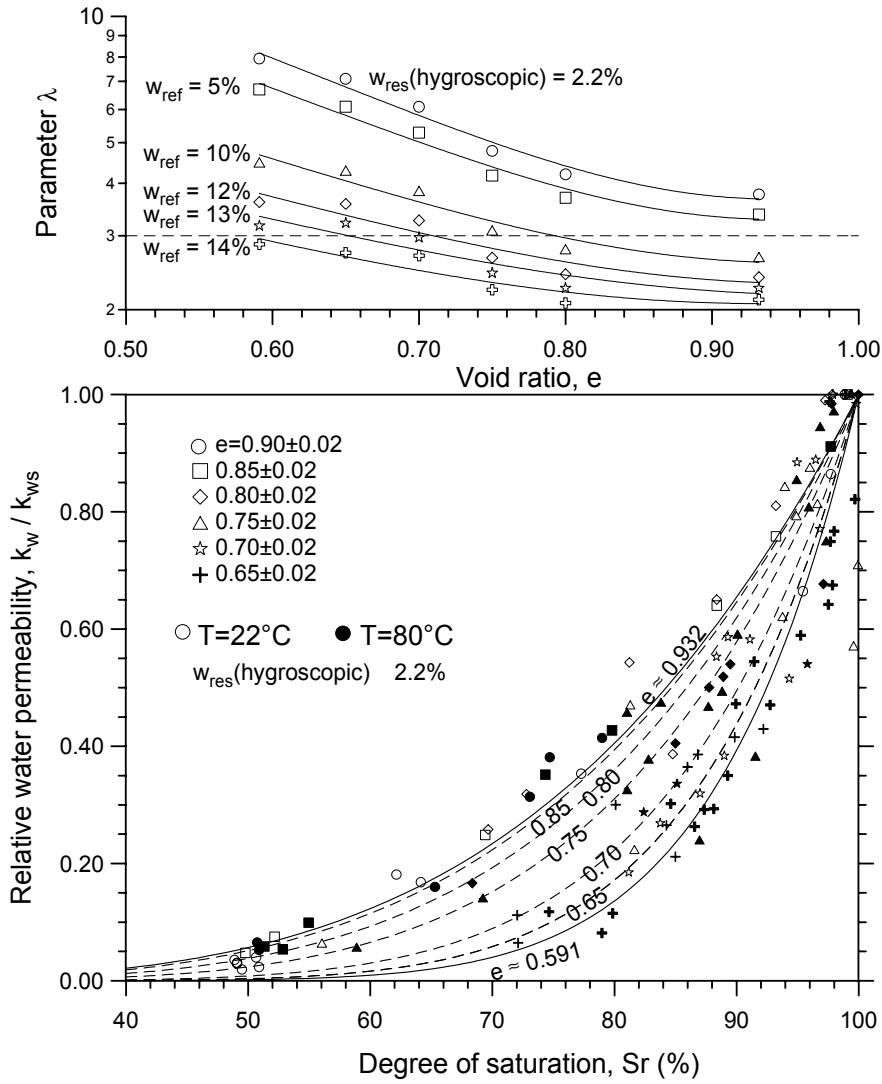
Figure 5.41   Relative water permeability-Sr relationships for different packings (w_{res} = 2.2%).
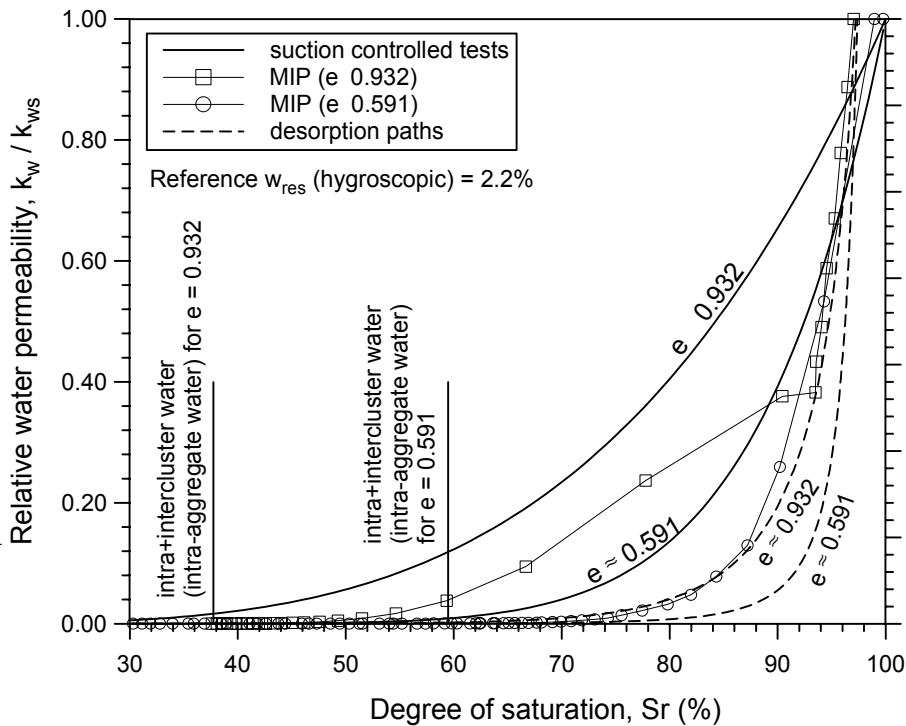
Figure 5.42   Relative water permeability-degree of saturation relationships for different packings at a reference w_{res} = 2.2% (inflow/outflow results and MIP-retention curve predictions).
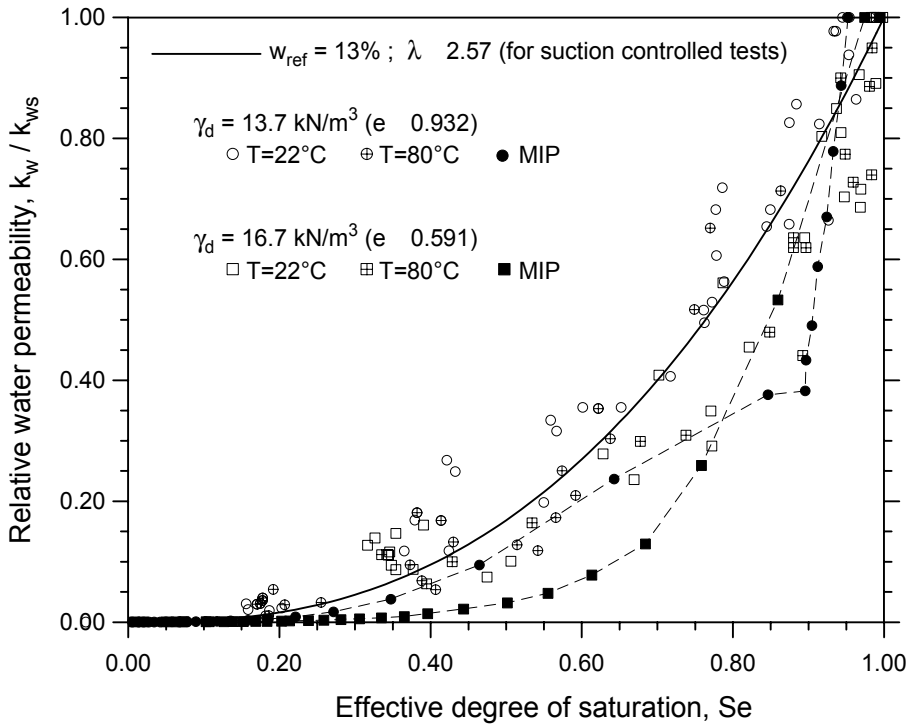
Figure 5.43 Relative water permeability-effective degree of saturation relationships for different packings at a reference w_{ref} = 13% (inflow/outflow results and MIP predictions).
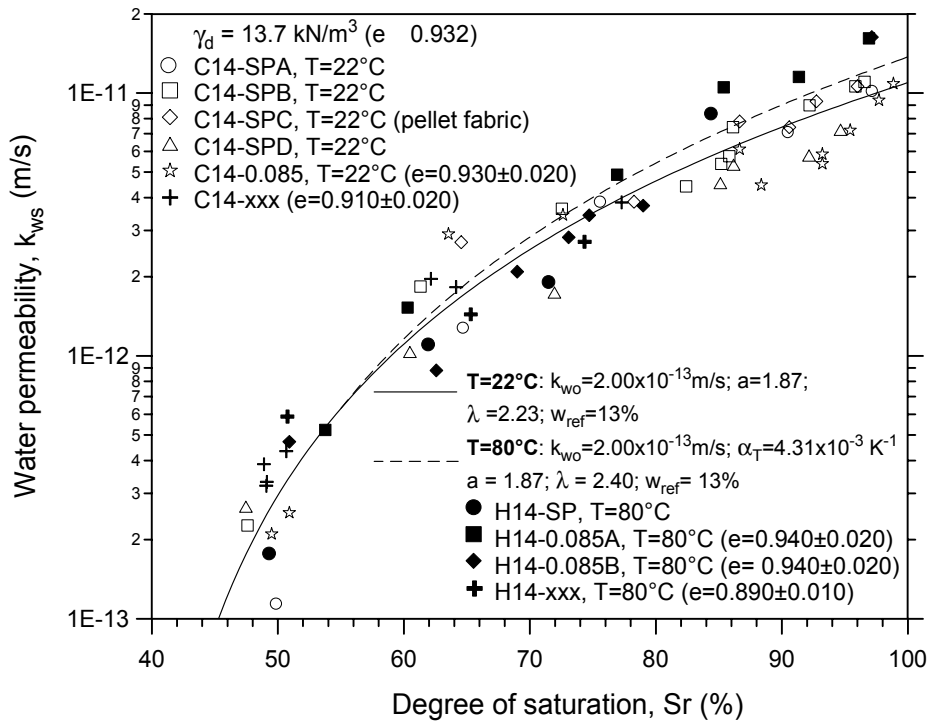

Figure 5.44 Water permeability for the high-porosity packing at different degrees of saturation and temperatures (best-fit curve).
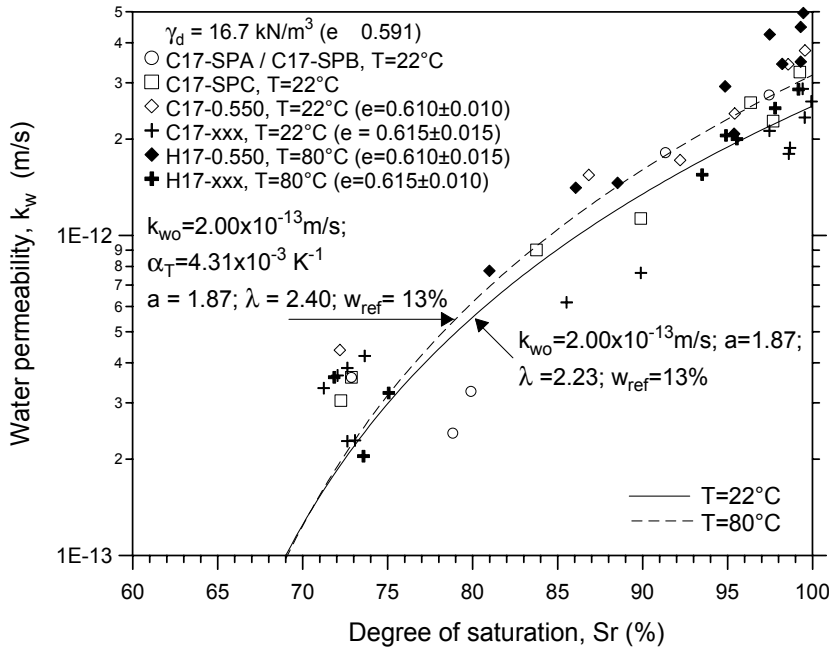
Figure 5.45 k_w for the low-porosity packing at different degrees of saturation and temperatures.
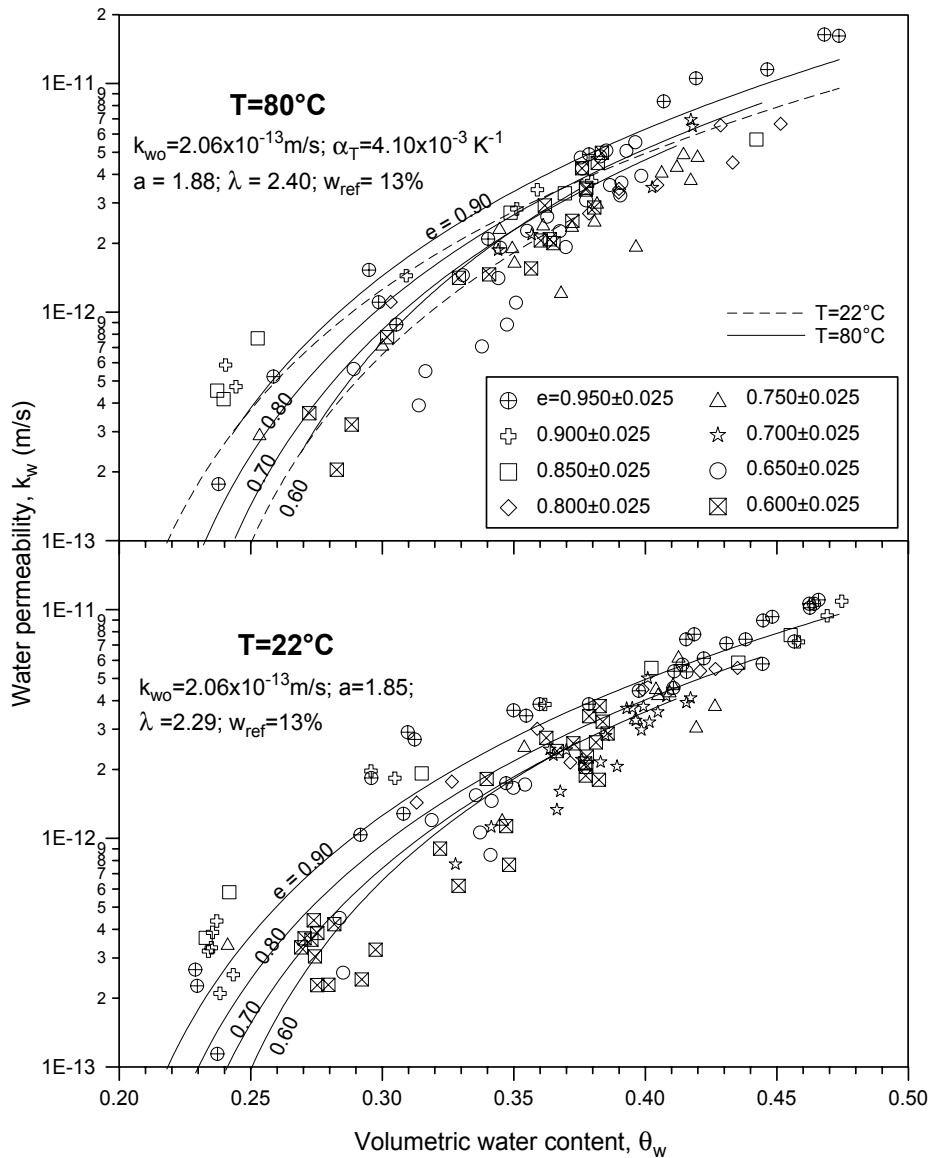

Figure 5.46 k_w-volumetric water content relationships at different void ratios and temperatures.